PATHOGEN DYNAMICS: MODELING AND ANALYSIS OF COMPETITION, ORGANIZATION, AND VACCINATION

by

Glenn Young

B.S. Mathematics, James Madison University, 2010

M.A. Mathematics, University of Pittsburgh, 2012

Submitted to the Graduate Faculty of

the Kenneth P. Dietrich School of Arts and Sciences in partial fulfillment

of the requirements for the degree of

Doctor of Philosophy

University of Pittsburgh

2016

UNIVERSITY OF PITTSBURGH

KENNETH P. DIETRICH SCHOOL OF ARTS AND SCIENCES

This dissertation was presented

by

Glenn Young

It was defended on

June 27, 2016

and approved by

Jonathan E. Rubin, Department of Mathematics

G. Bard Ermentrout, Department of Mathematics

David Swigon, Department of Mathematics

Hanna Salman, Department of Physics and Astronomy

Dissertation Advisors: Jonathan E. Rubin, Department of Mathematics,

G. Bard Ermentrout, Department of Mathematics

PATHOGEN DYNAMICS: MODELING AND ANALYSIS OF COMPETITION, ORGANIZATION, AND VACCINATION

Glenn Young, PhD

University of Pittsburgh, 2016

The work presented in this thesis is motivated by questions arising about pathogen dynamics. The effects of pathogens can be observed on a variety of spatial scales, from within-host interactions with the immune system on the microscopic level, to the spread of communicable disease on the population level. We present analyses of three common pathogens on three different scales. In Chapter 2, we derive and study a system of ordinary differential equations modeling the competition for space and resources between a mammalian host's native intestinal microbiota and an invasive species of Salmonella Typhimurium. We use our model to discuss optimal invasion strategies that maximize the salmonella's likelihood of successfully displacing the microbiota for a spot on the intestinal wall. In Chapter 3, we analyze an anomalous behavior observed in which two interacting pulses of *E. coli* in a one-dimensional nutrient gradient will turn around move away from one another rather than combine. To this end, we derive a novel system of ordinary differential equations approximating the dynamics of the classic Keller-Segel partial differential equations model for bacterial chemotaxis, and use this approximation to make testable predictions about mechanisms driving the turn around behavior. Finally, in Chapter 4, we use a two-strain SIR-type model of rotavirus transmission to study the effects of vaccination on a population exposed to multiple endemic strains.

TABLE OF CONTENTS

LIST OF TABLES

LIST OF FIGURES

PREFACE

The content in Chapter 2 appeared as "A boundary value approach to optimization with an application to salmonella competition" in the Bulletin of Mathematical Biology, vol. 77, no. 7, 1327-1348. It is copyright to Springer, 2015. The content in Chapter 4 appeared as "Qualitative effects of monovalent vaccination against rotavirus: a comparison of North America and South America" in the Bulletin of Mathematical Biology, vol. 77, no. 10, 1854-1885. It is copyright to Springer, 2015.

There are many people who deserve my deepest gratitude, without whom I sincerely believe I could not have accomplished this or much else in my life.

First and foremost, thank you to my advisors Jonathan Rubin and Bard Ermentrout. Your combined advice, high standards, and the innovation have shaped the way I think and approach problems, and I am eternally grateful.

To Hanna Salman, thank you introducing me to the world of collective dynamics and for the advice you provided as a committee member. I've greatly enjoyed our collaboration.

To David Swigon, thank you for all the feedback, both on my thesis and also during and after talks.

Thank you Eunha Shim for introducing me to mathematical epidemiology and all the guidance you provided within that field.

Thank you to my friends and colleagues. Scott Zimmerman, Abby Snyder, Jeff Dunworth, Torrey Gallagher, without your support, I am positive I would not have made it through this program.

To my family: Mom, Dad, Scott, Liz, Marshall. To adequately express my appreciation would double the page length of this thesis. Thank you for everything.

Leah, beyond everyone and everything else, I would not be where I am without you. Your constant support means more than you know.

1.0 INTRODUCTION

Understanding how pathogens interact with each other and their environment is imperative when it comes to controlling the spread and impact of disease. Experimentalists exploring these dynamics are presented with many difficulties, however; in vivo host-pathogen studies are made difficult by uncontrollable factors such as variation in immune response and gut biome composition, and population-level experiments of disease spread would be unethical at best. Mathematical modeling offers a tractable method of studying the nonlinear relationships governing the organization and interaction of microbes that are otherwise difficult or unethical to pursue.

Mathematical models of pathogen dynamics as they occur within a host organism are naturally called *within-host* models. Such models are usually on a small spatial scale, focus on the behavior of pathogens while inside of a host, and often consider the interaction of pathogens with a host's immune system. Within-host models are becoming invaluable tools for studying mechanisms behind specific aspects of their interactions inside of a host [36]. For example, the authors in [67] study the human inflammatory response due to influenza infection. In [43], a phenomenon in which the number of infected erythrocytes undergoes damped oscillations during malaria infection is captured and studied. These models vary in terms of complexity, from considering well-mixed, homogenous populations [4, 9], to spatially heterogeneous systems that require some form of cell motility [2, 62].

Cell motility plays a vital role in the spread of bacterial disease. Many pathogens "swim" to areas within a host that are most favorable for colonization and therefore maximize the likelihood of infection [54]. Such processes can lead to the aggregation of biofilms in patients and on medical equipment, a common cause of chronic infection that is becoming more significant with the rise of antibiotic resistant bacteria [18, 84]. Mathematical modeling

has a successful history in analyzing these processes. The Keller-Segel partial differential equations model for bacterial chemotaxis has been used to analyze important processes in biofilm formation, such as aggregation [46], the formation of traveling pulses [48, 75], and pattern formation [91]. Beyond biofilms, mathematical models for collective motion by chemotaxis such as the Keller-Segel model have been used to study the propagation of cancer [76] and even crime [81].

On a larger scale, models concerned with the dynamics of the spread of communicable disease in human, animal, or plant population are called *population-level* or *epidemiological* models. The earliest example of a population-level epidemic model is perhaps due to Daniel Bernoulli in 1760, when he derived and analyzed a mathematical model of smallpox transmission in an effort to influence the establishment of a vaccination program [10]. More recently, such models have been used to produce estimates of morbidity and mortality rates of communicable diseases and determine the benefits of various intervention methods. These models are valued tools in determining public policy and action, especially with quickly emerging and fast spreading viruses (e.g., West Nile virus [101], avian flu [17], ebola [28], and Zika virus [63]). There are also ongoing efforts being made to link within-host dynamics to population-level models together to create a more complete description of the transmission and impact of diseases [35].

The work in this thesis focuses on the development and analysis of systems of ordinary differential equations (ODEs) and partial differential equations (PDEs) that model biological systems arising from the study of pathogen dynamics. Many of our analytical techniques come directly from dynamical systems theory; in particular, we make heavy use of linear stability analysis and bifurcation theory to study the effect of variation of parameters on model behavior. A large proportion of our analytical techniques are novel, however; we present a variety of methods we developed with the purpose of answering specific biological questions, and then frame our methods in a more general context to facilitate application to other problems. In Chapters 2 and 3, we demonstrate the practicality and versatility of boundary value problems through a variety of examples related to optimization and transient analysis. In Chapter 3, we offer a novel approximation to the spatio-temporal dynamics of the advection-diffusion PDE system that offers qualitative agreement with the original model

and facilitates efficient analysis of varied parameters. While these methods are analytic, much of our analysis is carried out numerically using XPPAUT [29].

The following three chapters of this thesis present work motivated by a desire to understand the dynamics of different pathogens at various spatial scales. In Chapter 2, we study the within-host competition between the native, gut-dwelling microbiota, and an invading population of Salmonella Typhimurium. In Chapter 3, we analyze an anomalous behavior observed in interacting *E. coli* populations. In Chapter 4, we consider the possible effects of a monovalent vaccination on the spread of rotavirus. A brief summary of the content of each chapter concludes this introduction.

In Chapter 2, we develop a novel optimization framework to study strategies in ecological competition processes. The optimization method uses theory from dynamical systems describing the asymptotic behavior of a bistable system based on initial conditions, which we implement using a numerical boundary value problem. As an application of our method, we develop a model of the competition between Salmonella Typhimurium (S. Typhimurium) and the host's native microflora, which constantly and densely inhabit the intestinal lining of most mammals. S. Typhimurium invades the gut in two distinct phenotypic populations, one virulent and one avirulent, though the avirulent bacteria have the ability to activate a virulence factor and thereby "switch" into the virulent population. Counterintuitively, some studies have found that the combined population of S. Typhimurium gains an environmental advantage over the commensal microbiota after the virulent subpopulation provokes the body's inflammatory defenses. Our model represents the competition between the commensal microbiota, the avirulent salmonella, and the virulent salmonella populations and incorporates a simple representation of the immune response. We use our model to predict optimal strategies that would favor salmonella in its competition with the commensal bacteria. For example, if the switching rate of the salmonella from avirulent to virulent is known, our model can be used to make predictions about the minimum initial population size necessary to outcompete the microbiota and colonize the gut.

In Chapter 3, we study an anomalous behavior observed in interacting *E. coli* populations. When two populations of *E. coli* are placed on opposite ends of a long channel with a supply of nutrient between them, they will travel as pulses toward one another up

the nutrient gradient [75]. We present experimental evidence that the two pulses will in some cases change direction and begin moving away from each other and the nutrient back toward the end of the channel from which they originated. Intuition suggests that because the two bacterial populations produce the same chemoattractant to which they are mutually attracted and are both attracted up the interior nutrient gradient, they should both continue to move inward until they meet, and then combine into a single population. To study why this is not the case, we use an adaptation of the Keller-Segel PDE model for chemotaxis that includes an external nutrient source to elucidate mechanisms behind this direction switch. While the Keller-Segel model has been used to study a variety of important processes related to bacterial motility, it has not been used to study transient direction changes. We introduce a heuristic approximation to the spatial profile of each population in the Keller-Segel model to derive a system of ODEs approximating the temporal dynamics of the center of mass and the width of each spatial profile. This ODE model facilitates linear stability analysis of equilibrium states and numerical simulation, and allows phase plane analysis in some situations. In these ways, our approximate model simplifies analysis of the global dynamics of the bacterial system and allows us to efficiently explore the qualitative behavior changes across variations of parameters, and thereby provides experimentally testable hypotheses about the mechanisms behind the turnaround behavior. In particular, our model predicts that the center of mass of each bacterial pulse is generically ahead of (with respect to the direction of motion) the center of mass of the chemoattractant for early time. The bacteria are therefore attracted inward toward the nutrient and outward by their own chemoattractant and will turn around if the outward attraction is stronger than the inward attraction.

In Chapter 4, we study the effect of a vaccination program on the spread of rotavirus in a human population. Rotavirus is the most common cause of severe gastroenteritis in young children worldwide. The introduction of vaccination programs has led to a significant reduction in number of hospitalizations due to rotavirus in North and South American countries. Little work has been done, however, to examine the differential impact of vaccination as a function of strain distribution and strain-specific vaccine efficacy. We develop a two-strain epidemiological model of rotavirus transmission, and use it to examine the effects of a monovalent vaccine (Rotarix) on the qualitative behaviors of infection levels in a population.

For contrast, we parameterize our model with strain distribution data from North America and from South America. In all cases, the introduction of the vaccine leads to significant decreases in the prevalence of primary infection due to both strains for a decade or more, after which the overall prevalence recovers to near pre-vaccination levels. The prevalence of G1P[8] is significantly higher in North America (73% of all rotavirus infections) compared to that of South America (34%). Our model predicts that the introduction of Rotarix might result in major strain replacement in regions such as North America where the prevalence of G1P[8] is relatively high, due to higher efficacy of Rotarix against infection caused by G1P[8], while regions with lower prevalence of G1P[8], such as South America, are not susceptible to major strain replacement.

2.0 A BOUNDARY VALUE APPROACH TO OPTIMIZATION WITH AN APPLICATION TO SALMONELLA COMPETITION

2.1 INTRODUCTION

Interspecies competition often involves competition over a common resource, such as food, water, sunlight, or space. The outcome of such competition generally falls in favor of the species that can most quickly and efficiently make use of the resources, thereby limiting the resources available for the competitor. A species that can effectively use resources and inhibit its competitors' resource access is said to have a competitive advantage, and the greater its advantage, the greater the chances of survival for a species. From this perspective, a competitor should always adopt a strategy that maximizes competitive advantage and therefore chance of survival.

In this chapter, we seek to determine the optimal strategy that an invasive population can use to outcompete an established population. To this end, we develop an optimization method to determine the minimum initial size of a population needed for it to mount a successful invasion in a bistable competition setting. Our method is motivated by dynamical systems theory. In a bistable deterministic competition model, the asymptotic behavior of the system is entirely decided by initial conditions. The winner of the competition is determined by the side of a separatrix on which the system begins. In general, finding an analytical or numerical expression for the separatrix of such a system is difficult or impossible, and so finding an exact threshold for the success or failure of each species relative to the other is often impractical. Instead, we define a simple empirical condition that appears to be necessary and sufficient on the transient behavior of the system that determines the outcome of the competition. We use this idea to formulate a boundary value problem

that determines the smallest population size of an invasive species that will displace the established population, which we implement numerically.

As an application of our optimization method, we develop a novel model of the competition between Salmonella enterica serovar Typhimurium (S. Typhimurium) and a host's native intestinal microflora. Once salmonella enter a host, they must make their way into the lower intestine, where they attempt to colonize a spot on the interior intestinal wall. To successfully invade the gut, however, salmonella must outcompete a dense and ever-present layer of commensal microbiota [83]. These microbiota provide the final hurdle for the salmonella to cross before they can colonize the gut: the invaders must somehow use available energy and resources to displace the microbiota and expose the inhabitable intestinal wall. Remarkably, the virulence factor type III secretion system TTSS-1 allows S. Typhimurium to survive within host macrophages and thereby gain an environmental advantage over the commensal microbiota during the host's non-specific immune response [83]. S. Typhimurium is known to maintain a phenotypically distinct avirulent population during host invasion, which does not express the virulence factor. These avirulent cells reproduce at a faster rate than their virulent counterparts, but also can activate the virulence factor, thereby switching into the virulent population [86]. It seems reasonable to assume that S. Typhimurium has evolved in such a way as to increase its chance of survival inside of a host. To better understand the relative contributions of these two populations and the role of switching between them, we developed a system of ordinary differential equations that models the competition between the invasive S. Typhimurium and a native population of commensal microbiota, and we apply our optimization method to determine the virulence activation rate and initial proportions of avirulent and virulent salmonella that minimize the total initial salmonella population size necessary to outcompete the commensal bacteria. Our model therefore determines parameter values that represent behavioral characteristics of the salmonella that make it easiest for the salmonella to invade and become established in the gut.

In the following section, we introduce and develop the general idea of the optimization framework. In Section 2.3, we construct and analyze a model of the competition between the invasive S. Typhimurium and the commensal microbiota. Our model is based on a previous two-dimensional competition model encompassing an effect known as the differential killing

hypothesis [13]. We expand on this model in a number of ways, most importantly by modeling the virulent and avirulent salmonella phenotypes as separate populations and including a simple dynamic model of the immune system. We analyze this model to demonstrate conditions under which the salmonella population benefits from invading with two phenotypically distinct populations. The ability of the salmonella to outcompete the commensal microbiota depends heavily on the virulence factor activation rate, as well as the initial proportion of the avirulent and virulent phenotypes in the total population. In Section 2.5, we use our method to find the switching rate and the initial proportion of avirulent phenotypes (and consequently, the initial proportion of virulent phenotypes) that minimize the total initial salmonella population size necessary to outcompete the commensals for a spot on the intestinal wall. The optimal parameters that we compute represent an optimal strategy for the salmonella to use when invading the gut; that is, a population of S. Typhimurium maximizes its chance of successfully invading the gut by invading with the optimal initial proportion of avirulent cells and virulence activation rate. We follow up with a thought experiment concerning the initial and final ratios of avirulent to virulent salmonella. In theory, S. Typhimurium might have a greater chance of survival with a higher proportion of avirulent cells when surviving outside of a host, since the avirulent cells grow faster than their virulent counterparts. Consequently, we extend our optimization framework to determine optimal strategies for the salmonella to use within the host in order to exit the host with any ratio of avirulent to virulent cells. Our results provide experimentally testable predictions on important properties, namely the optimal switching rate and initial distribution of avirulent and virulent cells, found in bacterial populations.

2.2 OPTIMIZATION FRAMEWORK

Many bistable deterministic competitions are decided once one of the competitors surpasses some threshold given by a separatrix. For example, consider the two species competition governed by Lotka-Volterra-type deterministic equations

$$\begin{aligned} x' &= x(1 - x - \alpha y) \\ y' &= y(1 - y - \beta x), \end{aligned} \tag{2.1}$$

with $\alpha > \beta > 1$. The outcome of such a competition is determined by the position of the initial condition relative to the stable manifold of the interior saddle point, as shown in Figure 2.1. Species y will outcompete species x if and only if the system is ever above the stable manifold. Of course, the stable manifold of a general nonlinear system is very difficult or impossible to determine analytically, and consequently using the stable manifold as a separatrix is in practice out of the question. Instead, we can often determine a simpler sufficient condition to determine when species y outcompetes species x that is straightforward to check. In this case, if $x(t_1) = y(t_1)$ for any time t_1, then y will outcompete x because the identity line lies above the stable manifold. Moreover, if $x(0) > y(0)$, the condition is also necessary, since the system must pass through the identity line $y = x$ while approaching the steady state $(x, y) = (0, 1)$.

We now make use of this observation to find the minimum required initial y-value y_0 such that if $y(0) = y_0$, then y outcompetes x, assuming that species x has an established population and begins at its carrying capacity, $x(0) = 1$. The desired y_0 value is exactly the y-value of the intersection of the line $x = 1$ and the stable manifold, which we call y_s. In this two-dimensional case, we can numerically find this intersection by starting just off the saddle point on the stable manifold and integrating backwards in time until we reach $x = 1$, but this method is not easily generalizable to higher dimensional manifolds. Instead, we observe that starting above the stable manifold on the line $x = 1$ results in y outcompeting x, and, importantly, the system crossing the line $y = x$ at some unknown time $t_1 = t_1(y_0)$. The closer y_0 gets to the stable manifold, the more time it takes for the system to cross the line $y = x$, and the larger t_1 becomes; in particular, $\lim_{y_0 \downarrow y_s} t_1(y_0) = \infty$. Consequently, we can force y_0 to be arbitrarily close to y_s by requiring that $y(t_\infty) = x(t_\infty)$, where t_∞ is a sufficiently large number.

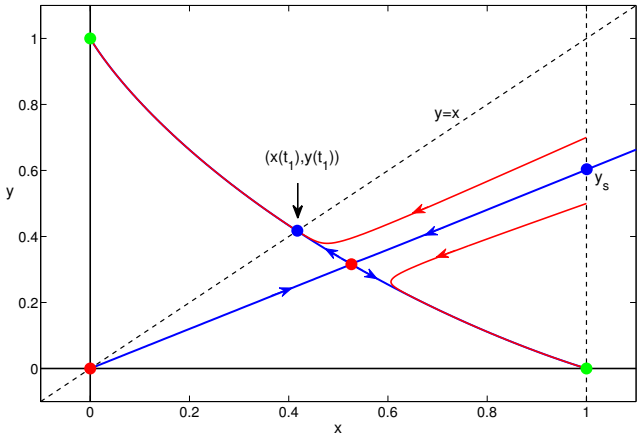

Figure 2.1: Two species Lotka-Volterra-type bistable competition. Assuming species x begins at carrying capacity $x = 1$, species y will outcompete x if and only if it invades with an initial population greater than y_s, which marks the intersection of the stable manifold of the saddle point (center red dot) and the line $x = 1$. The system crosses the identity line $y = x$ at time $t = t_1$, denoted in the figure by the blue dot labeled $(x(t_1), y(t_1))$. The green dots at $(0, 1)$ and $(1, 0)$ mark the two stable fixed points of the system, corresponding to the outcome where x outcompetes y and where y outcompetes x, respectively. The origin marked with a red dot is an unstable steady state.

We find this approximation of y_s numerically by solving the boundary value problem on $t \in [0, t_\infty]$:

$$\begin{aligned} \dot{x} &= x(1 - x - \alpha y) \\ \dot{y} &= y(1 - y - \beta x) \\ \dot{y}_0 &= 0 \\ x(0) &= 1 \\ y(0) &= y_0 \\ y(t_\infty) &= x(t_\infty). \end{aligned} \tag{2.2}$$

The addition of the third differential equation $\dot{y}_0 = 0$ serves a dual purpose: it allows us to include a third boundary condition and, along with the boundary conditions $y(0) = y_0$ and $y(t_\infty) = x(t_\infty)$, it forces the initial value of y to lie as close as we want to y_s.

The numerical solution of boundary value problem (2.2) yields y_s, the smallest initial y-value y_0 such that y will outcompete the established population x. Of course, the intersection of the stable manifold and the line $x = 1$ (and consequently the lower bound on y_0 yielding successful invasion) will vary with system parameters. We can minimize y_0 over any parameter by simply continuing the solution of the boundary value problem along this parameter.

2.3 SALMONELLA TYPHIMURIUM COMPETITION MODEL

Salmonella infection is a leading cause of foodborne illness worldwide, typically resulting in diarrhea, abdominal cramps, and fever for 4-7 days [74, 14]. S. Typhimurium exploit the host's immune response to displace the commensals from the intestinal wall in a variety of ways. First, invoking the immune response recruits macrophages. Though macrophages typically ingest and eliminate foreign bacteria, virulent S. Typhimurium have evolved to survive and even reproduce within host macrophages [74, 83]. Since inflammation will also disrupt the commensal microbiota, macrophage resistance likely contributes to S. Typhimurium's ability to colonize the gut, a phenomenon dubbed the *differential killing hypothesis* in [83]. Second, inflammation shifts nutrient availability in the intestine. In the uninflamed intestine, nutrients are used efficiently by the microbiota, but inflammation introduces organic compounds such as ethanolamine and cellular detritus, which S. Typhimurium might be better suited to consume[83, 90]. The advantage gained by the S. Typhimurium from this nutrient shift has been called the *food hypothesis* [83].

Despite the advantages that inflammation and therefore virulence provide, a subpopulation of invasive S. Typhimurium remarkably do not express the virulence factor TTSS-1 and are consequently avirulent. Intuitively, if S. Typhimurium gain an environmental advantage over the commensal microbiota by invoking the host's immune response, then every

salmonella cell should express TTSS-1 to maximize their advantage. However, the existence and persistence of the avirulent salmonella suggests that the avirulent cells must provide another type of advantage in the competition against the commensals.

Experiments have shown that avirulent salmonella cannot survive within host macrophages, but they reproduce at a much quicker rate than their TTSS-1-expressing counterparts [30, 86]. The fast growing avirulent cells are thought to allow the entire salmonella population to withstand the early stages of invasion, when their numbers are low, before inflammation takes effect. Moreover, recent studies on growth rates of S. Typhimurium have concluded that avirulent S. Typhimurium are able to "switch on" the virulence factor TTSS-1 while in the gut [86]. There is no evidence that the bacteria can switch back from virulent to avirulent, and the role of this switching mechanism in gut invasion is not fully understood.

We now develop a mathematical model of the competition between the virulent salmonella, V, the avirulent salmonella, U, and the established commensal microbiota population, C, on a small patch in the lower intestine. Our model is adapted from a three-population competition model.

$$\begin{aligned} U' &= U(g_U - \alpha(C+V) - \gamma U) \\ V' &= V(g_V - \alpha(C+U) - \gamma V) \\ C' &= C(g_C - \alpha(V+U) - \gamma C) \end{aligned} \tag{2.3}$$

In this basic model, each population $\zeta \in \{C, V, U\}$ has exponential growth rate g_ζ. Since the expression of the virulence factor slows growth rate, we always impose $g_V < g_U$. Moreover, each population suppresses the other two with competition parameter α and itself with self-crowding parameter γ.

We extend the basic model (2.3) to include additional biological features, as follows:

$$
\begin{aligned}
U' &= U(g_U - \alpha(C+V) - \gamma U + \sigma_U f(V) - \kappa M - d_r) \\
V' &= V(g_V - \alpha(C+U) - \gamma V + \sigma_V f(V) - (\kappa - r_V)M) + d_r U \\
C' &= C(g_C - \alpha(V+U) - \gamma C + \sigma_C f(V) - \kappa M) \\
P' &= aM - \mu_P P \\
D' &= g_D - (b_P P + b_V V + \rho V + \mu_D)D \\
M' &= (b_P P + b_V V)D - (\delta_V V + \mu_M)M \\
f(V) &= \frac{\delta V}{1+V}.
\end{aligned} \tag{2.4}
$$

As has been noted previously by, e.g., [74, 82], S. Typhimurium gains an environmental advantage over the commensals by inciting the inflammatory immune response of the host. We therefore include in our system a simple model of the immune response, motivated by those found in [19] and [68], in the form of a dynamic population of activated macrophages, M. Nonactivated macrophages serve a variety of purposes in the body, but once activated, their singular role is the elimination of pathogens. The nonactivated macrophages can be activated by pathogens and also by pro-inflammatory cytokines, which are produced by already activated macrophages. In our model, macrophages are activated at rate b_V when any member of a pool of nonactivated macrophages, D, comes into contact with a virulent salmonella cell and at rate b_P when a nonactivated macrophage comes into contact with a pro-inflammatory cytokine, P. The activated macrophages then kill each of the three bacterial populations at rate κ upon contact with the corresponding population. Since virulent S. Typhimurium are able to survive and reproduce within macrophages, the killing rate of V by M is reduced by a factor that we denote by r_V. The model does not include an equivalent reduction in the killing rate of the avirulent salmonella by the macrophages because they cannot survive within macrophages [30].

The pro-inflammatory cytokines P are produced by the macrophages at rate a and decay naturally at rate μ_P. The nonactivated macrophages D are produced by the body at rate g_D, activated by the pro-inflammatory cytokines and virulent salmonella at rate b_P and b_V, respectively. The nonactivated and activated macrophages naturally decay at rate μ_D and

μ_M, respectively. We also allow nonactivated and activated macrophages to be killed by virulent salmonella at rate ρ and δ_V, respectively, as has been observed experimentally [11].

We include in our model a food source f for each of the three bacterial populations to use as energy, which leads to faster growth. We assume available food is proportional to the amount of virulent salmonella, as virulence triggers inflammation and inflammation produces nutrients not found in the uninflamed intestine [90, 83]. The parameter δ is simply a scaling factor related to the amount of food available. The relative ability of each population to utilize the energy provided by food is given in the parameters σ_ζ, $\zeta \in \{C, V, U\}$. In accordance with the food hypothesis, we impose $\sigma_C < \sigma_U$ and $\sigma_C < \sigma_V$.

Experiments show that while in the gut, the avirulent salmonella are able to express the virulence factor TTSS-1 and consequently "switch" to join the virulent population [86]. We include this switching ability in our model as a drift rate, d_r, from U to V. Experimentalists have not observed "switching" from the virulent phenotype to the avirulent phenotype, and so we do not include a drift rate from V to U [86].

Since the reactions are happening locally in a patch in the gut, the body has an abundance of cytokines and nonactivated macrophages to contribute to the area; however, the available food nearby is limited. We therefore ignore any saturating effects on P and D but include them in f.

Finally, we assume that the commensal microbiota have reached their carrying capacity before the invasion by the salmonella, and that the gut contains no salmonella leading up to the invasion, such that initially no activated macrophages are present. In the following sections, we will concern ourselves with the initial size of the combined salmonella invading force, and consequently it is convenient to consider the avirulent and virulent populations as fractions of the total salmonella population. We define S_0 to be the initial salmonella population $S_0 = U(0) + V(0)$ and x to be the initial proportion of avirulent cells $x =$

$U(0)/(U(0)+V(0))$. We therefore consider system (2.4) with the following initial values:

$$\begin{aligned} U(0) &= xS_0 \\ V(0) &= (1-x)S_0 \\ C(0) &= g_c/\gamma \\ P(0) &= 0 \\ D(0) &= g_D/\mu_D \\ M(0) &= 0 \end{aligned} \tag{2.5}$$

where g_c/γ and g_D/μ_D are obtained from solving $C' = 0$ and $D' = 0$ with $U = V = M = 0$, respectively.

It is important to note that since we do not have sufficient data to accurately parameterize the system, all simulation results about model (2.4)-(2.5) that we present are purely qualitative. In this vein, we chose parameter values that are of the correct relative magnitudes based on the published literature. These values are found in Table 3.1 and are dimensionless.

Variables			
U	Relative population size of avirulent salmonella		
V	Relative population size of virulent salmonella		
C	Relative population size of commensal microbiota		
M	Relative population size of activated macrophages		
f	Relative abundance of food		
P	Relative abundance of pro-inflammatory cytokines		
D	Relative population size of non-activated macrophages		
	Parameters	Values	Source
g_ζ	Growth rate of bacterial population $\zeta = C, V, U$	1.3,0.7,1.3	[86]
α	Competition parameter	1.3	
γ	Bacterial self-crowding parameter	1	
σ_ζ	Relative contribution from food to the growth rate of bacterial population $\zeta = C, V, U$	1,1.4,1.8	
κ	Rate of elimination of bacteria by macrophages	1.8	[68]
r_V	Reduction in the rate of elimination of virulent salmonella by macrophages in the virulent population	0.9	[34]
d_r	Drift rate of salmonella from avirulent to virulent	0-1	
b_P	Activation rate of macrophages by pro-inflammatory cytokines	0.01	[19]
b_V	Activation rate of macrophages by virulent salmonella	0.02	[19]
δ_V	Rate of elimination of activated macrophages by the virulent salmonella	0.05	
μ_M	Natural death rate of activated macrophages	0.05	[19]
δ	Food abundance-scaling coefficient	4	
a	Production rate of pro-inflammatory cytokines by activated macrophages	0.1	
μ_P	Natural death rate of pro-inflammatory cytokines	0.1	
g_D	Production rate of non-activated macrophages	0.1	
ρ	Rate of elimination of non-activated macrophages by the virulent salmonella	0.005	[34]
μ_D	Natural death rate of non-activated macrophages	0.12	[19]
x	Initial proportion of avirulent salmonella cells	0-1	

Table 2.1: Variables and parameters for model (2.4).

We require of our model that activated macrophages cannot persist in the gut in the

absence of virulent salmonella. By this requirement, we effectively ignore all other causes of inflammation and our analysis can be thought of relative to a baseline amount of activated macrophages, which we assume to be zero. For this reason, we consider system (2.4) with V omitted and P and D in pseudo-steady state, for simplicity:

$$\begin{aligned} U' &= U(g_U - \alpha C - \gamma U - \kappa M) \\ C' &= C(g_C - \alpha U - \gamma C - \kappa M) \\ M' &= \frac{g_D b_P a M}{b_P a M + \mu_D \mu_P} - \mu_M M. \end{aligned} \tag{2.6}$$

We restrict our parameters such that the fixed point $(U, C, M) = (0, C^*, 0)$, $C^* = g_C/\gamma > 0$ of system (2.6) is stable and no stable fixed points such that $M > 0$ exist. The Jacobian matrix obtained by linearizing (2.6) around this fixed point is

$$J = \begin{bmatrix} g_U - \alpha C^* & 0 & 0 \\ -\alpha C^* & -\gamma C^* & -\kappa C^* \\ 0 & 0 & (g_D b_P a)/(\mu_D \mu_P) - \mu_M \end{bmatrix}.$$

All three eigenvalues of this matrix are negative and the only fixed points in the nonnegative octant are such that $M = 0$ if and only if $g_U \gamma < g_C \alpha$ and $(g_D b_P a)/(\mu_d \mu_M \mu_P) < 1$, so we impose these two requirements on our parameters. Under these requirements, when virulent salmonella are absent, the macrophages are, too.

2.4 EFFECT OF DRIFT RATE AND INITIAL AVIRULENT PROPORTION ON LONG-TERM OUTCOMES

To illustrate the power of our optimization method, we will use it to determine optimal strategies that the invasive salmonella should use in the gut to most easily outcompete the commensal microbiota. An in depth exploration of optimal strategies is presented in the next section, but as a preliminary step, here we determine some properties of system (2.4), and in particular, the effect of the drift rate d_r and the initial proportion of avirulent salmonella

x on the ability of the salmonella to colonize the gut. Both parameters are strongly related to the relative size of the avirulent and virulent salmonella populations and consequently are useful in determining the relative impact of both populations during invasions.

In Figure 2.2, the initial total population size of the invasive salmonella is fixed at $S_0 = U(0) + V(0) = 0.65$, with the initial proportion of avirulent salmonella fixed at $x = U(0)/S_0 = 0.5$. In panel A, the drift rate of the salmonella from avirulent to virulent is $d_r = 0.1$, and the salmonella are promptly eliminated by the immune system, while the commensals persist. In panel B, the drift rate is turned up to $d_r = 0.5$, and the salmonella outcompete the commensals for a spot on the gut. This suggests that a larger conversion rate from the avirulent to the virulent phenotype helps the salmonella in their quest to colonize the gut. However, in panel C of the same figure, the drift rate is set to $d_r = 0.9$, and the commensals once again outcompete the salmonella. Consequently, there seems to be an intermediate optimal drift rate, at least for the fixed initial proportion of avirulent salmonella near $x = 0.5$.

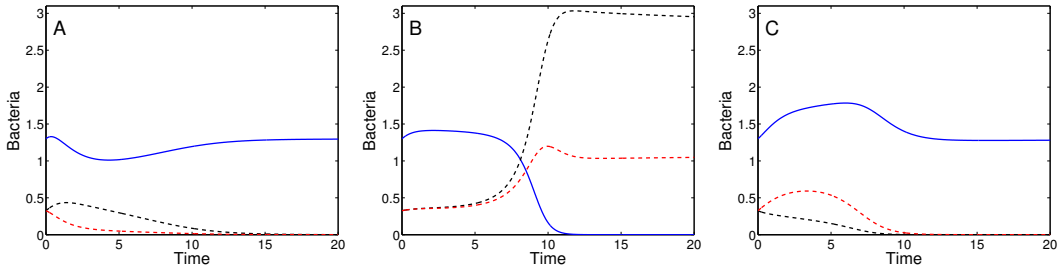

Figure 2.2: The outcome of the competition depends on the drift rate, d_r. All three panels show simulations of system (2.4) with C displayed as the blue curve, U as the dashed black curve, and V as the dashed red curve. $S_0 = U(0) + V(0)$ was fixed at 0.65 and x was fixed at 0.5 for all simulations. A. With drift rate $d_r = 0.1$, the commensals outcompete the salmonella. B. With $d_r = 0.5$, the salmonella outcompete the commensals. C. With $d_r = 0.9$, the commensals outcompete the salmonella once again. Since the salmonella outcompeted the commensals for one but not all drift rates shown, these figures suggest that there is an intermediate optimal drift rate for some fixed initial avirulent proportions x, such as $x = 0.5$.

Figure 2.3 shows a similar set up as in Figure 2.2, with the total initial invasive population

fixed at $S_0 = 0.65$, but now the drift rate is fixed at $d_r = 0.5$, and each panel shows the simulation for a different value of x. In panel A, $x = 0.1$, so only ten percent of the initial salmonella population is avirulent. This condition results in the commensals outcompeting the salmonella. Panel B in Figure 2.3 is the same as panel B in Figure 2.2, with $d_r = 0.5$ and $x = 0.5$. Increasing the initial proportion of avirulent salmonella to half of all invaders allows the salmonella to defeat the commensals and become established on the intestinal wall. Perhaps, then, having a higher avirulent proportion of the initial salmonella population is beneficial. The growth rate g_U of the avirulent phenotype is higher than the growth rate g_V of the virulent phenotype, so a larger initial population of the fast-growing avirulent salmonella could allow the entire salmonella population to survive the early stages of competition, after which drift rate d_r could cause an increase in the immune response-triggering virulent phenotype, which would help the salmonella outlast the remaining commensals. However, panel C shows that commensals quickly outcompete the salmonella when $x = 0.9$. Thus, we conclude that too large a proportion of avirulent invaders hurts the salmonella as a whole. These observations suggest that there is an interior optimum in the invasive proportion of avirulent salmonella for fixed drift rate; too few or too many avirulent salmonella cost the total population in the fight against commensals.

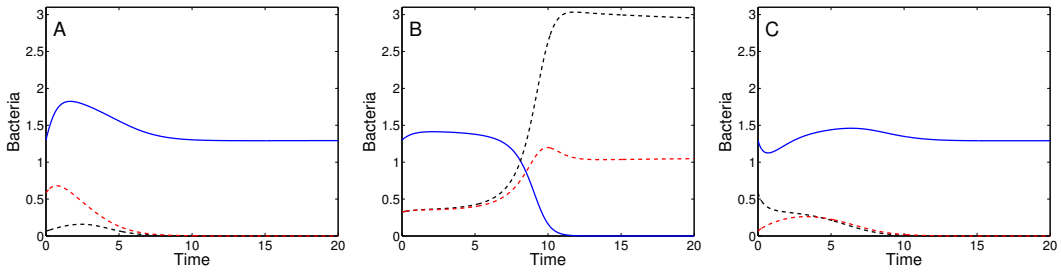

Figure 2.3: The outcome of the competition depends on the initial proportion of avirulent salmonella, x. All three panels show simulations of the system (2.4) with C displayed as the blue curve, U as the dashed black curve, and V as the dashed red curve. $S_0 = U(0) + V(0)$ was fixed at 0.65 and d_r fixed at 0.5 for all simulations. A. With $x = 0.1$, the commensals outcompete the salmonella. B. With $x = 0.5$, the salmonella outcompete the commensals. With $x = 0.9$, the commensals outcompete the salmonella. The salmonella only outcompete the commensals for the intermediate value of x, which suggests that there is an optimal initial avirulent proportion for some fixed drift rates d_r, such as $d_r = 0.5$.

Considering the above results, the two parameters d_r and x seem to play important roles in the competition between the salmonella and the commensal microbiota in the inflamed gut. Consequently, in the next section, we search for optimal strategies, in the sense of minimizing over d_r and x the initial salmonella population size S_0 needed for successful colonization.

2.5 FINDING OPTIMAL STRATEGIES

We now explore optimal invasion strategies from the salmonella's perspective. We consider the two parameters from the above section that impact the ability of the invasive salmonella to outcompete the commensal microbiota and colonize the gut: the drift rate d_r at which salmonella "switch" from the avirulent to the virulent population, and the proportion x of initial salmonella invaders that are avirulent. We ask what values of these quantities minimize the initial population size $S_0 = U(0) + V(0)$ necessary for the salmonella to successfully

outcompete the commensal bacteria. Given accurate parameter values, such an (x, d_r) pair would represent a prediction for the relative proportion of the two phenotypes found in an invasive S. Typhimurium population and the drift rate from avirulent to virulent states found in *S.* Typhimurium populations.

For a range of fixed d_r and x values, too small an initial population size S_0 will result in an unsuccessful invasion attempt, while a large enough S_0 will result in a successful invasion. Consequently, for each of these fixed parameter values, there is a minimum S_0 necessary to outcompete the commensals, which we call $S_{nec} := S_{nec}(d_r, x)$. In this notation, the optimal strategy we seek is given by $\arg\min_{d_r,x} S_{nec}(d_r, x)$.

We optimize using the method described in Section 2.2. We claim that the method extends naturally from our two-dimensional formulation to our six-dimensional model. Our approach for determining the optimal strategy described above is based on the numerical observation that if the total salmonella population is ever the same size as the commensal population, then the salmonella will ultimately outcompete the commensals; that is, if $U(t_1) + V(t_1) = C(t_1)$ at any time t_1, then $\lim_{t\to\infty} C(t) = 0$ and $\lim_{t\to\infty} U(t) + V(t) > 0$. This is the same condition we use to determine whether the invasive population outcompetes the established population in system 2.1 in Section 2.2. Conversely, if $\lim_{t\to\infty} C(t) = 0$ and $\lim_{t\to\infty} U(t) + V(t) > 0$, then the there must be a time t_1 such that $U(t_1) + V(t_1) = C(t_1)$, as long as $S_0 < C(0)$, which we will in general assume based on the idea that the salmonella is invading a domain where the commensal bacteria are already established. The existence of such a "crossing time" t_1 is therefore a necessary and sufficient condition that determines if the salmonella outcompete the commensals.

The crossing time t_1 depends on the initial salmonella population size S_0. In particular, if such a crossing time exists, an increase in S_0 will result in a shorter crossing time. This makes sense, since the more salmonella initially present, the faster they will outcompete the commensals. Similarly, a reduction in S_0 will result in a longer crossing time, until S_0 falls below the threshold $S_{nec}(d_r, x)$, after which the crossing time no longer exists because the commensals outcompete the salmonella. By continuity with respect to initial conditions, for each fixed d_r and x, and for any time t_1, there is an $S_0(t_1)$ so that the salmonella and commensal population sizes will be equal at t_1. As t_1 increases, the corresponding $S_0(t_1)$

decreases to a critical initial salmonella population size. Starting from this critical salmonella population size, a smaller S_0 would result in the commensals outcompeting the salmonella, while a larger S_0 would result in the salmonella outcompeting the commensals. This critical S_0 value for the fixed parameters is therefore $S_{nec}(d_r, x)$.

To find $\arg\min_{d_r,x} S_{nec}(d_r, x)$, we introduce the time-scaled system (2.7) with boundary conditions (2.8), both found in the Appendix. These equations represent a natural generalization of the boundary value problem system (2.2) from the Lotka-Volterra example in Section 2.2. According to our observation, the salmonella will outcompete the commensal microbiota if and only if $U(t_1)+V(t_1) = C(t_1)$ for some time t_1, and the larger t_1 is, the closer S_0 must be to $S_{nec}(d_r, x)$. We therefore approximate $S_{nec}(d_r, x)$ by requiring the crossing time t_1 to be large. We numerically implement this condition in system (2.7) by rescaling time by $s = t/\tau$, where $\tau = t_1$ is our required crossing time, and requiring that the populations cross at time $t = t_1$ by the boundary condition $C(1) = U(1)+V(1)$. Figure 2.4 shows an example solution of this boundary value problem. We illustrate that this approximation works well for large τ in Figure 2.10 in the Appendix.

Again using XPPAUT [29] we continue the solution of the boundary value problem (2.7)-(2.8) over a range of drift rate values d_r between 0 and 1 for fixed initial proportion of avirulent salmonella x. Figure 2.5A shows $S_{nec}(d_r, 0.1)$, $S_{nec}(d_r, 0.5)$, and $S_{nec}(d_r, 0.9)$ plotted versus the drift rate. For each fixed x, there is a clear interior minimum value of S_{nec}, and it is clear that these minima vary with x. We again use XPPAUT to pick out these minimal S_{nec} over all d_r between 0 and 1 for each fixed x , which we call $S_{min}(x) = \min_{d_r} S_{nec}(d_r, x)$, and use continuation in x to derive the full $S_{min}(x)$ curve (see Appendix). Figure 2.5B shows that the minimum of $S_{min}(x)$ occurs around $x = 0.5$ for this parameter set, implying that the salmonella should invade with roughly equal proportions of avirulent and virulent cells in order to maximize the population's chance at a successful invasion for these parameter values.

As was previously stated, we are concerned with finding pairs of d_r and x values that minimize the initial size of the invading salmonella population necessary to successfully outcompete the commensals. From the above, we have the x value which minimizes $S_{min}(x)$. To each $S_{min}(x)$ there corresponds a $d_r(x)$ for that fixed x that minimizes $S_{nec}(d_r, x)$; that

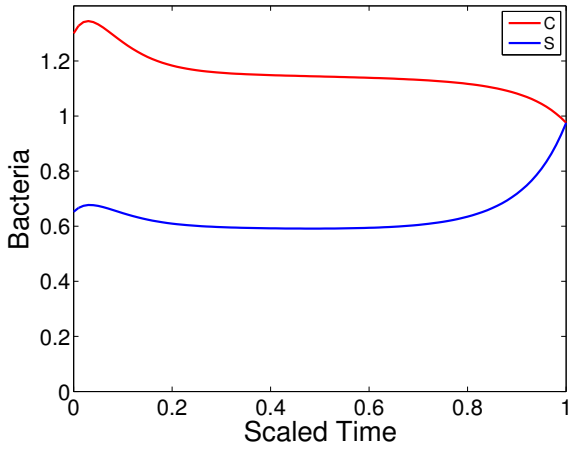

Figure 2.4: Boundary value problem solution with $\tau = 20$, $d_r = 0.3$, and $x = 0.5$. The upper red line represents the population of commensal microbiota, C, while the lower blue line represents the sum of the virulent and avirulent salmonella, $S = U + V$. The curves represent a solution to the boundary value problem, with right hand boundary condition $C(1) = U(1) + V(1)$, and the initial value $S(0) = U(0) + V(0)$ that is obtained is $S_{nec}(d_r, x)$. From this solution, we can vary the drift rate, d_r, and the initial proportion of avirulent cells in the salmonella population, x, to determine the minimum initial salmonella population size necessary to outcompete the commensals.

is, $d_r(x) = \arg\min_{d_r} S_{nec}(d_r, x)$. These optimal $d_r(x)$ are plotted versus x in Figure 2.5C. The figure shows that as x increases, the optimal d_r does as well. This makes sense, as a higher initial proportion of avirulent salmonella would require a faster virulence activation rate in order for the salmonella population to take advantage of the benefits that virulence provides. The dashed lines in the figure identify the d_r value corresponding to the x value that minimizes $S_{min}(x)$, as shown in Figure 2.5B. In particular, S_{min} is minimized when $d_r = 0.52$, implying that the avirulent salmonella should activate their virulence factor at that rate. Therefore, $(d_r, x) = (0.52, 0.5)$ represents the salmonella's optimal strategy for this particular parameter set.

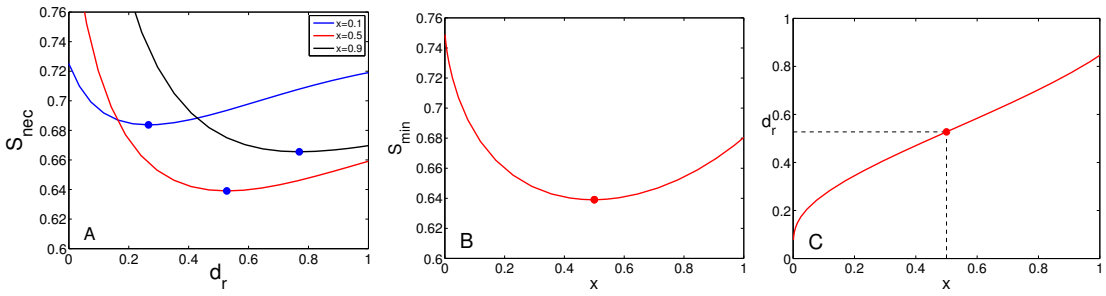

Figure 2.5: Optimal strategies and minimum necessary initial populations from continuation of solutions to boundary value problem (2.7)-(2.8) with $\tau = 20$ in d_r followed by continuation in x. A. S_{nec}, the minimum initial salmonella population necessary to outcompete the commensals, for three different fixed initial avirulent proportions x, as a function of switching rates d_r from 0 to 1. Each of the three curves in has an interior minimum value, which represents the smallest S_{nec} for that fixed value of x over all switching rates, which we call $S_{min}(x)$. B. $S_{min}(x)$ as a function of the initial avirulent salmonella proportion x. Note that d_r values can differ at different points on this curve. C. The $(x, d_r(x))$ pairs that minimize $S_{nec}(d_r, x)$ with respect to d_r. The dashed lines identify the x and d_r values that minimize S_{min}. The red circle in C corresponds to the same x value given by the red circle in B.

In the preceding analysis, for each fixed initial proportion of avirulent salmonella x, the minimal necessary invading salmonella population $S_{nec}(d_r, x)$ size was minimized over the drift rate d_r. Of course, we can ask the same question in the opposite order: for each fixed d_r, what value of x minimizes $S_{nec}(d_r, x)$? To answer this question, we use the same idea as before, only we now consider system (2.9) with boundary conditions (2.8), found in the Appendix, instead of system (2.7).

Figure 2.6A shows solutions to the boundary value problem for the drift rate fixed at $d_r = 0.3$, 0.5, and 0.7. Similar to the previous case, varying x reveals there is a minimum value of $S_{nec}(d_r, x)$ for each fixed d_r, which we call $S_{min}(d_r) = \min_x S_{nec}(d_r, x)$. Using XPPAUT, we continue the solution corresponding to $S_{min}(d_r)$ over d_r from 0 to 1, and the results are plotted in Figure 2.6B. Consistent with the approach used in Figure 2.5, the minimum S_{min} occurs around $d_r = 0.52$, meaning the avirulent salmonella should activate their virulence

factor at that rate in order to maximize their chance at a successful invasion.

The values of x that minimize $S_{nec}(d_r, x)$ for fixed d_r are plotted in Figure 2.6C, along with the corresponding curve from Figure 2.5C. The intersection of the two curves represents the (d_r, x) pair that minimizes $S_{nec}(d_r, x)$ over all d_r and x: $\min_{d_r,x} S_{nec}(d_r, x) = \min_x \left\{ \min_{d_r} S_{nec}(d_r, x) \right\} = \min_{d_r} \left\{ \min_x S_{nec}(d_r, x) \right\}$.

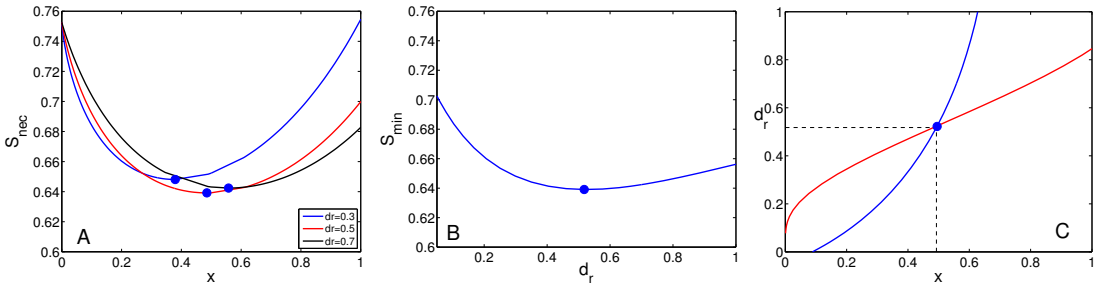

Figure 2.6: Optimal strategies and minimum necessary initial populations from continuation of solutions to boundary value problem (2.7)-(2.8) with $\tau = 20$ in x followed by continuation in d_r. A. S_{nec}, the minimum initial salmonella population necessary to outcompete the commensals, for fixed switching rates d_r, as a function of the initial proportion of avirulent salmonella x from 0 to 1. Each of the three curves has an interior minimum value, which represents the smallest S_{nec} for that fixed value of d_r over all initial avirulent proportions, which we call $S_{min}(d_r)$. B. $S_{min}(d_r)$ versus d_r. Note that x values can differ at different points on the curve. C. The curve of (x, d_r) pairs that minimize $S_{nec}(d_r, x)$ with respect to x is shown in blue and the curve of (x, d_r) pairs that minimize $S_{nec}(d_r, x)$ over d_r is shown in red. The intersection of the two curves represents the optimal strategy to be used by the salmonella when invading the gut.

The optimal strategies above are only optimal while the salmonella are within a host. After the bacteria are expelled, they find themselves in a new environment without any inflammatory response to exploit. Consequently, it might benefit the salmonella population to invade a host with the optimal proportion of avirulent cells described above, but leave the host with some other proportion of fast-growing avirulent cells that increases their chance of survival outside of a host. To explore this idea, we impose another condition and require

$x_{init} = \beta x_{final}$, where β is a constant, while $x_{init} = x$ and x_{final} are the proportions of avirulent cells in the total salmonella population at the beginning and end of the invasion, respectively. Details on how this additional condition was implemented can be found in the Appendix.

Holding all variables other than d_r and x constant, the final proportion of avirulent salmonella becomes a function of only d_r: $x_{final} = U^*(d_r)/(U^*(d_r)+V^*(d_r)) = U^*/(U^*+V^*)$, where $(U, V, C, M) = (U^*, V^*, 0, M^*)$, $U^*, V^* > 0$, is the steady state corresponding to a successful invasion. Thus for each fixed d_r, we need only consider the $x = x_{init}$ values such that $x = \beta U^*/(U^* + V^*)$. Figure 2.7 shows the curve in (d_r, x) space that preserves this equality with $\beta = 1$, along which we apply our optimization method. Figures 2.8A and B show the minimum salmonella invasion force necessary to colonize the gut, S_{min}, versus the initial proportion of avirulent salmonella x and the switching rate d_r, respectively, also with $\beta = 1$. Since we have added the constraint that $x_{init} = \beta x_{final}$, the minimum S_{min} value, $S_{min} = 0.6427$, is larger in these figures than in the analogous Figure 2.5B, where $S_{min} = 0.6393$.

This approach could be repeated to predict the optimal strategy for any other choice of $\beta > 0$.

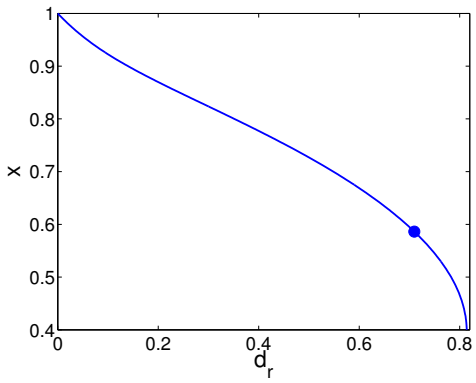

Figure 2.7: Parameter curve on which the initial proportion of avirulent salmonella is equal to the final proportion of avirulent salmonella. The blue dot at $(d_r, x) = (0.6743, 0.6161)$ denotes the (d_r, x) pair that minimizes S_{min} while preserving the equality $x_{init} = x_{final}$.

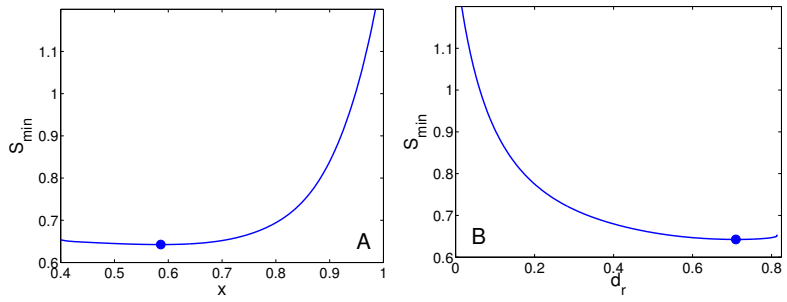

Figure 2.8: The optimal strategies with the added requirement that $x_{init} = \beta x_{final}$, with $\beta = 1$. A. The smallest initial salmonella population that will still outcompete the commensals, S_{min}, as a function of the initial proportion of avirulent salmonella x. B. S_{min} as a function of the switching rate d_r. The blue dots correspond to the x and d_r values that minimize S_{min}, which are the coordinates of the blue dot in Figure 2.7.

2.6 DISCUSSION

We have developed an optimization method to determine the minimum size of an invasive species population that will outcompete an established population. The method is based on analysis of general bistable competition models and is implemented by solving a boundary value problem numerically. Further, we constructed and analyzed a model describing the competition between a commensal microbiota population and an invasive salmonella population, along with a simple model of the immune response, under the assumptions of the two hypotheses about this competition proposed by Stecher and Hardt. Our model agrees with experiments in that populations of S. Typhimurium benefit from invading a host with two phenotypically distinct subpopulations of avirulent and virulent cells, rather than a population comprised of just avirulent or just virulent phenotypes. We went on to apply our optimization method to show how to determine the proportion of avirulent cells in the initial population and the virulence factor activation rate that maximize the chance of a successful invasion, for a fixed set of the model parameters.

Previous studies indicate that S. Typhimurium is an example of a species that gains an environmental advantage over a host's commensal microbiota as a result of the host's natural inflammatory response [82]. Stecher and Hardt proposed the differential killing hypothesis and the food hypothesis as mechanisms by which the salmonella gain this advantage [83]. Brown et al. [13] incorporated the food hypothesis into a simple model of the competition between S. Typhimurium and the commensal microbiota [13]. The food hypothesis is supported by, e.g., [90], which found that the inflamed intestine contains ethanolamine, a nutrient which supports the growth of salmonella, but not the commensal microbiota. In this chapter, we constructed and analyzed a novel model describing the competition between the commensal population and the salmonella population, including separate virulent and avirulent salmonella subpopulations, and incorporating the two hypotheses proposed by Stecher and Hardt along with a simple model of the immune response that mediates the differential killing effect.

At first glance, the need for both virulent and avirulent salmonella subpopulations may seem unnecessary. While the salmonella population as a whole benefits from the host's inflammatory response, only the virulent bacteria invoke inflammation. However, since the relative growth rate of the virulent population is slowed by the expression of virulence factor TTSS-1 [86], the fast-growing avirulent population allows the salmonella to become established during the early stage of the invasion. Thus, we expect that there could exist an optimal initial proportion of avirulent salmonella in the entire invasive population exclusively between 0 and 1, and our model confirms this expectation. This result is consistent with experiments, which have shown that both virulent and avirulent phenotypes exist in invasive S. Typhimurium populations. Moreover, avirulent S. Typhimurium are observed to "switch on" the virulence factor TTSS-1. Again, since a high switching rate would cause most or all of the salmonella to become virulent, we expect a nontrivial optimal switching rate, and our model confirms that such an optimal rate exists. It is reasonable to expect that while S. Typhimurium evolved to benefit from the body's inflammatory response, they also evolved in such a way as to activate their virulence factor at the rate that gives the greatest environmental advantage. We viewed the minimal initial population necessary to successfully colonize the intestine as a measure of this advantage, since the probability of

successful invasion should be proportional to this quantity. Our model allows us to estimate this minimal invasion force, as well as the corresponding switching rate and initial proportion of avirulent cells.

These results supply us with the means of creating experimentally testable hypotheses about the virulence initiation rate, the minimal initial salmonella population necessary to colonize the intestine, and the initial proportion of avirulent salmonella. If the switching rate is known, then the corresponding S_{min} value in Figure 2.6B represents the predicted minimal necessary salmonella invasion force, and the corresponding x value in Figure 2.6C provides a prediction of the optimal initial proportion of avirulent cells. For example, if the switching rate is found to be 0.4 hr^{-1}, then avirulent cells should make up about 43% of the initial salmonella population, and the minimal necessary invasion force S_{min} is predicted by our model to be above half the size of the established commensal population. Similarly, if the initial proportion of avirulent cells in the salmonella population is known, then Figure 2.5B predicts the value of S_{min}, and Figure 2.5C predicts the optimal switching rate d_r.

Since salmonella must survive outside of a host after being expelled, and the environment outside of the host is drastically different from the environment within the host, there is reason to believe the salmonella population would do better entering this non-host environment with a potentially different proportion of avirulent cells then that with which it invades. If we make the further assumption that the salmonella exit the host with a certain proportion of avirulent cells, we can still make analogous predictions about the expected switching rate and the smallest salmonella invasion force necessary to outcompete the commensals. Of course, the additional requirement will cause the minimum necessary initial salmonella size to become larger than that determined in the unconstrained case, but the increased chance to survive outside of the host could make up for this disadvantage.

The optimization method that we have introduced can be applied to any bistable system, and is generalizable to multi-stable systems, as long as a necessary and sufficient condition for each outcome, analogous to crossing the identity line in our example, can be formulated. In this way, the method must be problem-specific, as a condition that works for one system might not work for another. However, the ease with which such a condition can be implemented makes this method simple and attractive.

Future work can enhance the above analysis in several ways. Most notably, we made the simplifying assumption that the rate of virulence factor activation in S. Typhimurium is constant; however, Sturm et al. [86] showed that this switching rate can increase over time. It seems reasonable to assume that the switching rate might be proportional to the number of macrophages present, and to optimize such a rate would require techniques from variational calculus. Further, we have considered only temporal dynamics, corresponding to interactions in a small, localized region in the gut. A natural extension of the model would be to include both more aspects of the physiology involved, such as the blood, lumen, and so on [5]), and spatial aspects of bacterial interactions, which may allow virulent bacteria to invade successfully in some locations but not others. The coexistence of avirulent and virulent phenotypes itself raises an evolutionary question: how did the virulence factor-activating ability of the avirulent cells evolve? It may be possible to investigate this question through stochastic evolutionary models.

2.7 APPENDIX

To determine the minimal initial salmonella population size necessary to outcompete the commensals, we rescale time by $t = \tau s$ to transform system (2.4) to the following boundary value problem:

$$\begin{aligned}
U' &= \tau(U(g_U - \alpha(C+V) - \gamma U + \sigma_U f(V) - \kappa M - d_r)) \\
V' &= \tau(V(g_V - \alpha(C+U) - \gamma V + \sigma_V f(V) - (\kappa - r_V)M) + d_r U) \\
C' &= \tau(C(g_C - \alpha(V+U) - \gamma C + \sigma_C f(V) - \kappa M)) \\
P' &= aM - \mu_P P \\
D' &= g_D - (b_P P + b_V V + \rho V + \mu_D)D \\
M' &= \tau((b_P P(M) + b_V V)D(V,M) - (\delta_V V + \mu_M)M) \\
d_r' &= 0 \\
f(V) &= \frac{\delta V}{1+V},
\end{aligned} \tag{2.7}$$

where $' = \frac{d}{ds}$, and

$$\begin{aligned} U(0) &= xS_0 \\ V(0) &= (1-x)S_0 \\ C(0) &= g_C/\gamma \\ P(0) &= 0 \\ D(0) &= g_D/\mu_D \\ M(0) &= 0 \\ C(1) &= U(1) + V(1). \end{aligned} \tag{2.8}$$

where τ is a large positive number that we choose.

Here we consider d_r as a stationary variable instead of a parameter. Since we are minimizing S_0, it might seem more natural to allow S_0 to be a stationary variable and leave d_r as a parameter that we can vary. Solving such a boundary value problem and continuing the solution over varied d_r in AUTO results in solutions as in Figure 2.9A, where the minimum value of S_{nec} appears as a local minimum. Unfortunately, bifurcation continuation methods cannot continue along minima, as minima are not bifurcations. Treating d_r as a variable allows us to identify folds in the solution of the boundary value problem (2.7)-(2.8) where the derivative of d_r with respect to S_0 becomes unbounded. Such a fold is shown in Figure 2.9B. Solving the boundary value problem in this setting therefore allows us to continue the solution over a new parameter; in particular, we can continue the solution in x to determine $S_{min} = \min_{d_r} S_{nec}(d_r, x)$.

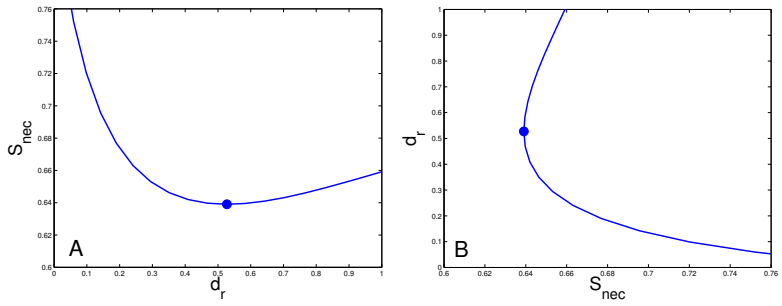

Figure 2.9: Minimal salmonella population sizes necessary in successful invasions, derived using boundary conditions (2.8). A. The S_0 value obtained by solving system (2.4) together with $S_0' = 0$ and boundary conditions (2.8) over a range of d_r values. The bifurcation continuation software AUTO cannot continue along minima, and so this solution cannot be continued along a new parameter. B. The d_r value obtained by solving system (2.7) with boundary conditions (2.8) for varied $S_{nec} \equiv S_0$. Here, the minimum value of S_{nec} with respect to d_r is given by a fold bifurcation, which allows us to continue to track the minimum as x is varied in AUTO.

We seek the critical value of S_0 so that beginning with any initial salmonella population size below this value results in the commensals outcompeting the salmonella, while initial salmonella population sizes above this level yield successful invasion. Our method to determine this value is based on the description in Section 2.2. After rescaling time, solutions to the boundary value problem (2.7)-(2.8) for fixed S_0 and x return a value of d_r for which we have $C(1) = U(1) + V(1)$, where C, U, and V are now considered functions of rescaled time s. Consequently, we are really searching for the value of d_r for which $S_0 = S_{nec}(d_r, x)$. If S_0 is any larger for the fixed x and d_r, then $U(s_0) + V(s_0) = C(s_0)$ for some $0 \leq s_0 < 1$ and if S_0 is any smaller, then the combined population $U + V$ will not match C before $s = 1$, and possibly never will. Analogous to the treatment of system (2.2) in Section 2.2, we can approximate the critical value of S_0 within arbitrary precision by taking τ sufficiently large. We take $\tau = 20$, which seems to be large enough to provide an accurate approximation of the critical S_0, as seen in Figure 2.10.

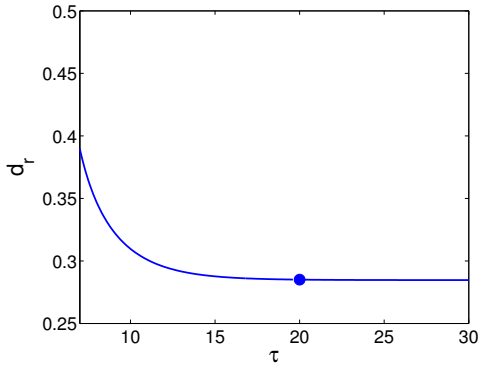

Figure 2.10: Justification for the choice of τ. The value of d_r in the solution to system (2.7) with boundary conditions (2.8) remains near its asymptotic value around and beyond $\tau = 20$. Here, $x = 0.5$ and $S_0 = 0.652$.

Similarly, in order to minimize $S_{nec}(d_r, x)$ over x for fixed d_r, we consider the following system:

$$\begin{aligned}
U' &= \tau(U(g_U - \alpha(C+V) - \gamma U + \sigma_U f(V) - \kappa M - d_r)) \\
V' &= \tau(V(g_V - \alpha(C+U) - \gamma V + \sigma_V f(V) - (\kappa - r_V)M) + d_r U) \\
C' &= \tau(C(g_C - \alpha(V+U) - \gamma C + \sigma_C f(V) - \kappa M)) \\
P' &= aM - \mu_P P \\
D' &= g_D - (b_P P + b_V V + \rho V + \mu_D)D \\
M' &= \tau((b_P P(M) + b_V V)D(V,M) - (\delta_V V + \mu_M)M) \\
x' &= 0 \\
f(V) &= \frac{\delta V}{1+V},
\end{aligned} \tag{2.9}$$

The technique to solve the boundary value problem (2.9) with boundary conditions (2.8) is identical to that described above, with the roles of d_r and x switched.

To add the constraint that the final proportion of avirulent salmonella is equal to the initial proportion of avirulent salmonella (or any fraction β of the initial proportion, although we set $\beta = 1$ here), we restrict our (d_r, x) parameter values to only those such that

$x = U^*/(U^* + V^*)$, where $(U, V, C, M) = (U^*, V^*, 0, M^*)$, $U^*, V^* > 0$ is the steady state corresponding to a successful invasion. We find such parameter pairs by continuing this steady state along d_r and setting $x = U^*/(U^* + V^*) = U^*(d_r)/(U^*(d_r) + V^*(d_r))$ for each fixed d_r. Since we do not have an analytical form for this steady state, we load the d_r and corresponding $x = U^*/(U^* + V^*)$ values into XPPAUT as functions of a new parameter q, so that $(d_r(q), x(q))$ preserves the equality $x_{init} = x_{final}$ for all q. We then solve the system

$$\begin{aligned}
U' &= \tau(U(g_U - \alpha(C+V) - \gamma U + \sigma_U f(V) - \kappa M - d_r)) \\
V' &= \tau(V(g_V - \alpha(C+U) - \gamma V + \sigma_V f(V) - (\kappa - r_V)M) + d_r U) \\
C' &= \tau(C(g_C - \alpha(V+U) - \gamma C + \sigma_C f(V) - \kappa M)) \\
P' &= aM - \mu_P P \\
D' &= g_D - (b_P P + b_V V + \rho V + \mu_D)D \\
M' &= \tau((b_P P(M) + b_V V)D(V, M) - (\delta_V V + \mu_M)M) \\
S_0' &= 0 \\
f(V) &= \frac{\delta V}{1+V},
\end{aligned} \tag{2.10}$$

with boundary conditions (2.8) in XPPAUT. Here there is no advantage to treating x or d_r as a stationary parameter in place of S_0, as our parameter space $(d_r, x) = (d_r, x(d_r))$ is now one-dimensional, and consequently we need only vary a single parameter to find the global minimum S_{min}. We continue the solution of the boundary value problem in AUTO over varied q, from which we can extract the corresponding $d_r(q)$ and $x(q)$ for each q, and the result is plotted in Figures 2.8A and B.

3.0 INTERACTIONS OF SOLITARY PULSES OF *E. COLI* IN A ONE-DIMENSIONAL NUTRIENT GRADIENT

3.1 INTRODUCTION

In 1970, Evelyn Keller and Lee Segel proposed a mathematical model to analyze the aggregation process of slime mold [46]. In the following year, they derived a general model describing the collective dynamics of populations that move by chemical sensing, or chemotaxis [47]. This so-called Keller-Segel model has provided a cornerstone for the mathematical study of the collective behavior of biological species. Since its inception, the Keller-Segel model has been applied to approximate the dynamics of a variety of species, from slime molds such as *Dictyostelium discoideum* to bacteria such as *Escherichia coli* to insects such as the fruit fly *Drosophila melanogaster* [39, 41, 51]. Many adaptations have been developed to include additional biological realism, such as signal-dependent sensitivity [50, 77] or non-local sampling of a chemical [39, 58]. The primary biological questions addressed by these models are typically centered around describing aggregation processes [46], pattern formation [12, 40, 41, 62], and the development of traveling waves [42, 48, 56], while the mathematical questions typically concern existence of solutions and conditions for finite-time blow up [39, 41, 85]. Here we use such a model to address a different problem: analyzing the transient dynamics of two interacting pulses of bacteria in a nutrient gradient.

In Section 3.2, we present experimental results due to the Salman laboratory at the University of Pittsburgh demonstrating the dynamics of two interacting *E. coli* populations in a nutrient gradient. When two *E. coli* populations are placed on opposite ends of a long channel with a supply of nutrient between them, they travel as pulses toward one another up the nutrient gradient. Interestingly, in some cases they will change direction and begin

moving away from each other and the nutrient back towards where they started. Because the two bacterial populations move by chemotaxis up the nutrient gradient and they both produce the same chemoattractant to which they are mutually attracted, it seems reasonable that they should always continue moving inward toward one another, meet in the middle, and subsequently combine into a single, unified population. As this is not the case, we use a Keller-Segel model that includes an external nutrient source to elucidate mechanisms behind this unintuitive direction switch. External gradients play an important role in collective behavior of species that move by chemotaxis. For example, it has been shown that an external nutrient gradient can give rise to a traveling pulse in a bacterial population [75]. Temperature and oxygen gradients have also been shown to influence the collective dynamics of such populations [21, 24, 71, 72].

Pulse-pulse interaction has also been studied in a number of reaction-diffusion equations, including the Gierer-Meinhardt and Gray-Scott models [25, 27, 87]. In [25] and [87], the authors use asymptotic approaches to derive approximate ordinary differential equations for the distance between the center of pulses. We do not use formal asymptotic estimates to derive approximations for the center of the pulses here, but instead make a straightforward heuristic approximation to the spatial profile of each pulse using a Gaussian distribution. From this assumption, we are able to derive a system of ODEs approximating the temporal dynamics of the center of mass and the width of the pulses. Analysis of the Keller-Segel partial differential equations model is complicated by finite-time blow up of solutions and numerical difficulties. By contrast, our ODE system eases linear stability analysis of equilibrium states and numerical simulation, and even allows phase plane analysis in some situations. In these ways, our approximation facilitates analysis of the global dynamics of the bacterial system and allows us to efficiently explore the qualitative behavior changes across variations of parameters.

This chapter is organized as follows: in Section 3.2, we present experimental results due to the Salman laboratory highlighting this unusual result in which two identical *E. coli* populations can turn around rather than combine. Next, in Section 3.3, we show that the classic Keller-Segel model for bacterial chemotaxis captures the experimentally observed behaviors. In Section 3.4 and 3.5, we show that our approximating system agrees with the

Keller-Segel model in predicting that bacterial accumulation is the result of an instability of the uniform state that occurs when the bacterial population size gets sufficiently large. In Section 3.6, we use our approximation to analyze parameter conditions that lead to turn around of the bacterial populations and conditions that cause them to combine.

3.2 EXPERIMENTAL RESULTS

Wild type *Escherichia coli* (*E. coli*) RP437, expressing either yellow fluorescent protein (YFP) or red fluorescent protein (tdTomato) from a medium copy number plasmid (pZA) under the control of the constitutive λ-promoter, were grown in M9 minimal medium supplemented with 1g/l casamino acids, and 4g/l glucose (M9CG) at 30°C until early exponential growth phase (Optical Density at 600nm (OD_{600nm}) = 0.1). The cultures were then centrifuged for 5 minutes at 10,000 rpm, and resuspended in fresh M9CG medium at an OD_{600nm}=0.3. Each of the bacterial cultures was loaded onto one end of a set of ∼2cm long, thin channels (800 μm wide, 20-25 μm deep) fabricated in polydimethylsiloxane (PDMS) and adhered to a microscope glass slide (Figure 3.1A). The channels were pre-filled with fresh M9CG medium. The sample was then mounted onto an inverted microscope (Zeiss Axiovert 40 CFL), and the bacteria were observed in fluorescence mode using a 2.5x objective. Shortly after loading the bacterial cultures onto the slide ($\sim 10-20$ minutes), a sharp accumulation peak appeared at each end of the channel, which then proceeded to advance as a pulse towards the center of the channel following a food gradient created by the bacterial consumption at the densely populated ends (for more details about this phenomenon see for example [59, 72, 75]). The dynamics of both bacterial pulses was recorded, each in its correspondent fluorescence colors, at a rate of 1 image/9 seconds using a charge-coupled device (CCD) camera (Progress MF, Jenoptik). The fluorescence profile reflecting the bacterial concentration along the channel was measured using ImageJ (NIH). For each of the examples presented in Figure 3.1B and C, the fluorescence intensity is depicted in units of the maximal measured fluorescence at the peak of the concentration and the background was subtracted for better comparison.

Figure 3.1B and C displays only a ∼3.5mm long section of the channel where the two populations meet. These results show that upon collision between the two populations, two outcomes could occur. In the first (Figure 3.1B), the two populations combine and move together towards one end of the channel or sometimes (data not shown) stay at the collision location, while their accumulation peak reduces in amplitude and widens gradually by diffusion. In the second case (Figure 3.1C), the two populations' peaks never meet; rather, they approach each other initially and then bounce back, each towards the end of the channel where they originated.

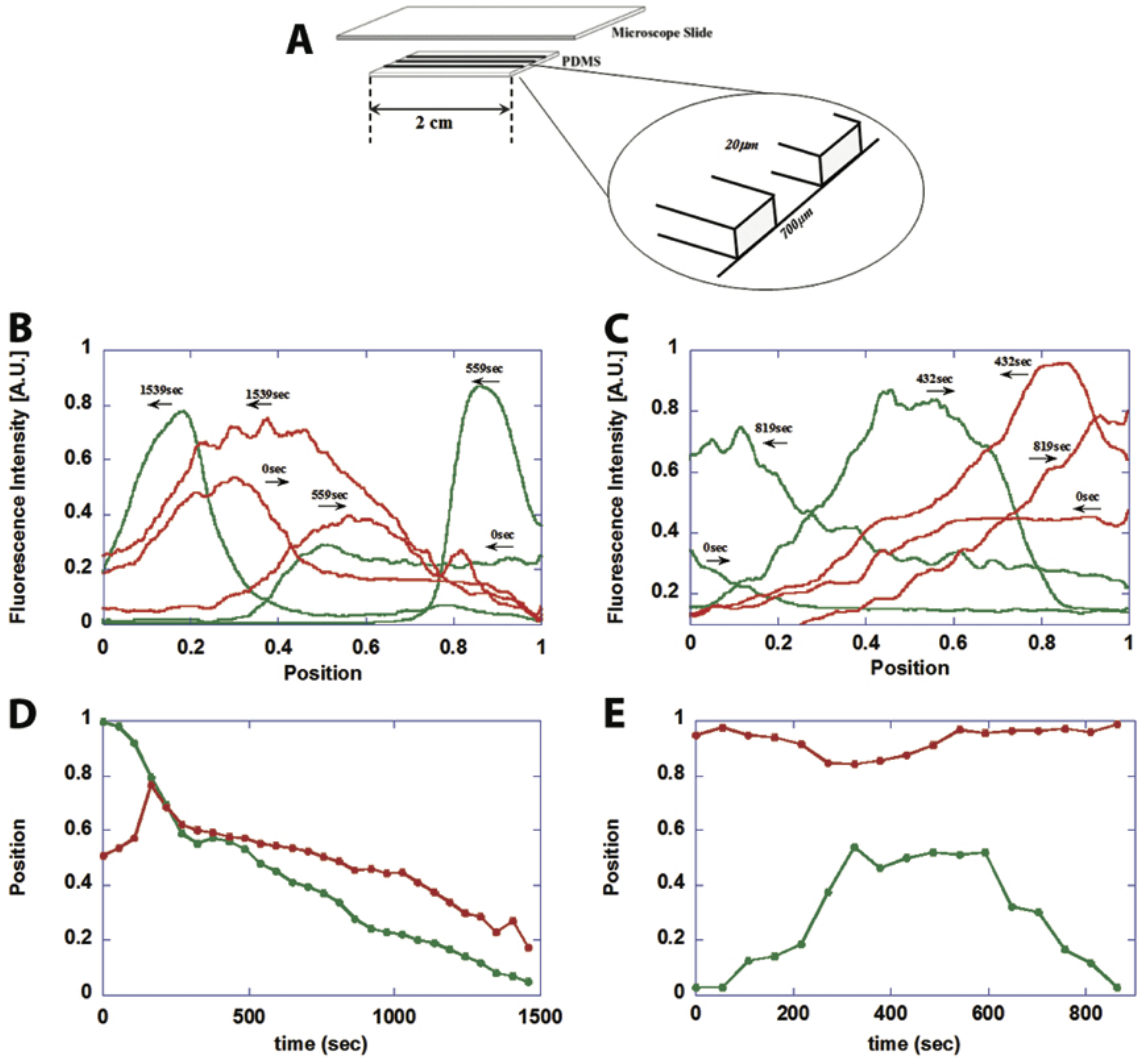

Figure 3.1: Experimental results (these data were collected by the Salman laboratory). (A) The experimental setup: a set of narrow channels (800μm×20μm), 2 cm long, microfabricated with polydimethyl-siloxane (PDMS) using the common techniques [59] and adhered to a microscope slide by plasma cleaning, while leaving both ends open for loading the bacteria. (B and C) Examples of the fluorescence intensity profile along the channel measured for both red and green bacteria as indicated by the color of the plot and at different time points marked in the graph. In (B) the two bacterial pulses advance towards each other and when they meet, they combine and move together towards the left end of the channel. In (C) the two pulses bounce back and move towards their original end of the channel. (D and E) The position of the peaks of the bacterial pulses over time. (D) corresponds to the data from panel (B) and (E) corresponds to the data from panel (C).

3.3 KELLER-SEGEL MODEL

We use an adaptation of the classic Keller-Segel model of chemotaxis to approximate the spatio-temporal dynamics of the above experiment. We denote by $b(t, x)$ the bacterial density at time t and spatial position x. The cell density moves both by linear diffusion and by chemotaxis up a chemical gradient. A full derivation of the differential equations modeling such dynamics can be found in, for example, [39, 41]. Here we consider the effects of two chemical densities: a chemoattractant (glycine) produced by the bacteria, $a(t, x)$, and an externally added nutrient, $\phi(t, x)$. We assume that the chemoattractant is produced by the bacteria at constant rate r and naturally degrades at rate δ, and that the bacteria consume the nutrient at constant rate κ. Under these assumptions, the model we study is as follows:

$$\begin{aligned}
\frac{\partial b}{\partial t} &= D_b \frac{\partial^2 b}{\partial x^2} - \chi_a \frac{\partial}{\partial x}\left[b \frac{\partial a}{\partial x}\right] - \chi_\phi \frac{\partial}{\partial x}\left[b \frac{\partial \phi}{\partial x}\right] \\
\frac{\partial a}{\partial t} &= D_a \frac{\partial^2 a}{\partial x^2} + rb - \delta a \\
\frac{\partial \phi}{\partial t} &= D_\phi \frac{\partial^2 \phi}{\partial x^2} - \kappa b \phi \\
\left.\frac{\partial b}{\partial x}\right|_{x=0,1} &= \left.\frac{\partial a}{\partial x}\right|_{x=0,1} = \left.\frac{\partial \phi}{\partial x}\right|_{x=0,1} = 0
\end{aligned} \tag{3.1}$$

where the parameters are defined in Table 3.1.

We impose minimal biological assumptions on our model: we ignore any effects of cell physiology on chemical sensing, such as signal-dependent sensitivity, and any cell kinetics. The basic Keller-Segel model (3.1) captures the qualitative behaviors observed experimentally and is therefore a reasonable approximation of the *E. coli* system studied. We note that the receptor-binding adaptation to the Keller-Segel model (model (M2a) in [39]) produces similar qualitative results as we present in this paper, though we do not present those results here.

For the purpose of differentiating between two populations of bacteria in numerical simulations, we include in our model two identical populations of bacteria, b_1 and b_2, that each produce the same chemoattractant, a_1 and a_2, respectively. These variables are only

differentiated by their initial distributions and are otherwise identical:

$$\begin{aligned}
\frac{\partial b_1}{\partial t} &= D_b \frac{\partial^2 b_1}{\partial x^2} - \chi_a \frac{\partial}{\partial x}\left[b_1 \frac{\partial (a_1 + a_2)}{\partial x}\right] - \chi_\phi \frac{\partial}{\partial x}\left[b_1 \frac{\partial \phi}{\partial x}\right] \\
\frac{\partial b_2}{\partial t} &= D_b \frac{\partial^2 b_2}{\partial x^2} - \chi_a \frac{\partial}{\partial x}\left[b_2 \frac{\partial (a_1 + a_2)}{\partial x}\right] - \chi_\phi \frac{\partial}{\partial x}\left[b_2 \frac{\partial \phi}{\partial x}\right] \\
\frac{\partial a_1}{\partial t} &= D_a \frac{\partial^2 a_1}{\partial x^2} + r b_1 - \delta a_1 \\
\frac{\partial a_2}{\partial t} &= D_a \frac{\partial^2 a_2}{\partial x^2} + r b_2 - \delta a_2 \\
\frac{\partial \phi}{\partial t} &= D_\phi \frac{\partial^2 \phi}{\partial x^2} - \kappa (b_1 + b_2)\phi \\
\left.\frac{\partial b_{1,2}}{\partial x}\right|_{x=0,1} &= \left.\frac{\partial a_{1,2}}{\partial x}\right|_{x=0,1} = \left.\frac{\partial \phi}{\partial x}\right|_{x=0,1} = 0.
\end{aligned} \tag{3.2}$$

Importantly, the dynamics of the two population model are identical to those of the single population model because the system is linear in b and a. That is, if $b = b_1 + b_2$ and $a = a_1 + a_2$, then the system of differential equations governing the dynamics of b, a, and c is exactly system (3.1).

We nondimensionalize model (3.2) as follows:

$$b_1 = N\tilde{b}_1;\ b_2 = N\tilde{b}_2;\ a_1 = K\tilde{a}_1;\ a_1 = K\tilde{a}_1;\ \phi = M\tilde{\phi};\ x = \tilde{x}/L,$$

where N, K, and M are large numbers of approximately the same size of the maximum size of the bacterial, chemoattractant, and nutrient populations, respectively, and L is the domain length. After nondimensionalization, the parameter values we use are those given in Table 3.1. The natural dimensions (before nondimensionalization) are included. After nondimensionalization, all parameters have units s^{-1} and the spatial domain is the unit interval. For simplicity, we immediately replace the nondimensionalized symbols $\tilde{b}_1$, $\tilde{b}_2$, $\tilde{a}_1$, $\tilde{a}_2$, $\tilde{\phi}$, and $\tilde{x}$ with b_1, b_2, a_1, a_2 ϕ, and x, respectively, in the nondimensionalized system.

	Parameter	Value	Natural dimensions
D_b	Diffusivity of bacteria	0.001	space^2·time^{-1}
D_a	Diffusivity of attractant	0.03	space^2·time^{-1}
D_ϕ	Diffusivity of nutrient	0.03	space^2·time^{-1}
χ_a	Chemotactic sensitivity to attractant	0.025	space^3·time^{-1}·mol^{-1}
χ_ϕ	Chemotactic sensitivity to nutrient	0.015	space^3·time^{-1}·mol^{-1}
r	Production rate of attractant by bacteria	0.05	mol·bacterium^{-1}· time^{-1}
δ	Natural decay rate of attractant	0.005	time^{-1}
κ	Consumption rate of nutrient by bacteria	0.001	(bacterium/space)$^{-1}$·time^{-1}

Table 3.1: Parameters used in model (3.1).

We initialize all simulations with the two populations accumulated on opposite ends of the spatial domain. We assume that sufficient time has passed so that the bacteria have consumed the nutrient at the densely populated regions at the ends of the domain so that the nutrient concentration is initially distributed as the symmetric sigmoid function given by

$$\phi(0,x) = \begin{cases} \phi_0/(1+\exp(-100x+10)) & : 0 \le x \le 0.5 \\ \phi_0/(1+\exp(100x-90)) & : 0.5 < x \le 1 \end{cases}, \tag{3.3}$$

where ϕ_0 is a parameter. Without the external nutrient, the bacterial populations would remain accumulated at their respective ends of the domain, maintaining a concentration of chemoattractant, and would not travel inward.

A population evolving according to a Keller-Segel model can only form a nontrivial pulse if the population size is sufficiently large relative to model parameters [26, 39, 41, 55]. Below this critical threshold, the only solution is the uniform solution, $b = b_{tot}$ =constant, $a = rb_{tot}/\delta$. Model (3.1) in particular predicts that in order to maintain a nontrivial pulse,

the total amount of bacteria must be greater than the critical threshold defined by

$$b^*_{tot} = \frac{D_b[(k\pi)^2 D_a + \delta]}{r\chi_a}, \tag{3.4}$$

where k is any positive integer (see Section 3.8.1 in the Appendix for details) [26]. The nutrient does not come into play here because $\phi = 0$ in the uniform state.

Below threshold (3.4), the bacterial population cannot maintain a pulse-like solution. Figure 3.2 shows an example of a simulation of model (3.2) when the combined bacterial population size is less than threshold (3.4). The two populations initially form pulses and move up the food gradient toward the center, but eventually lose their pulse-like shapes and diffuse out to uniformly fill the spatial domain.

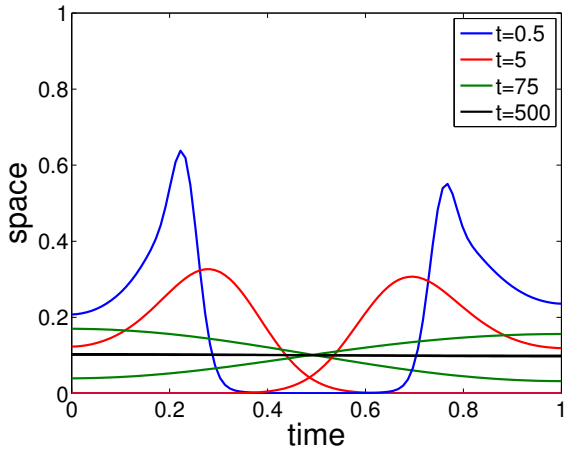

Figure 3.2: Bacteria dynamics with population size below critical threshold (3.4). The two populations initially move up the nutrient gradient but cannot maintain a pulse-like profile.

When the total amount of bacteria exceeds threshold (3.4), the bacterial populations will asymptotically form a pulse along one or both of the boundaries of the spatial domain. For consistency with experiment, we will only consider bacterial population sizes above this threshold.

Figures 3.3 and 3.4 show examples of simulations of system (3.2) that capture the two qualitatively distinct results observed experimentally. In Figure 3.3, the two bacterial populations move up the nutrient gradient toward one another until they meet and combine into a

single pulse, which propagates to one end of the domain. In Figure 3.4, the two populations initially move up the external nutrient gradient but eventually change direction and move backwards toward the chemoattractant that is accumulated near the boundaries. The only difference between the two outcomes is the initial amount of nutrient: the simulations shown in Figure 3.3 begin with more nutrient than those shown in Figure 3.4.

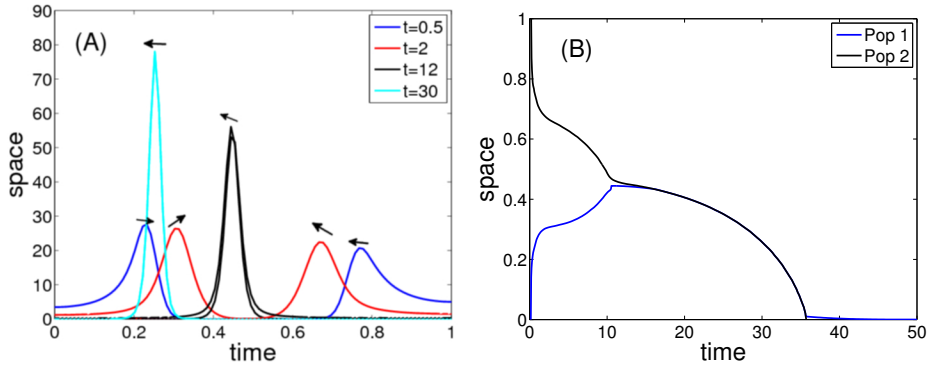

Figure 3.3: Bacterial pulses combine under the dynamics of system (3.2). The two populations move toward one another up the external nutrient gradient until they collide and combine to form a single pulse, which ultimately moves to and accumulates on the left wall. The initial food profile is given by the reflected sigmoid (3.3) with $\phi_0 = 20$. (A) Snapshots of the bacterial profiles at different times. The arrows indicate direction of motion. By $t = 30$, the two populations have combined and behind moving toward the left boundary. (B) The positions of the peaks of the bacterial pulses over time.

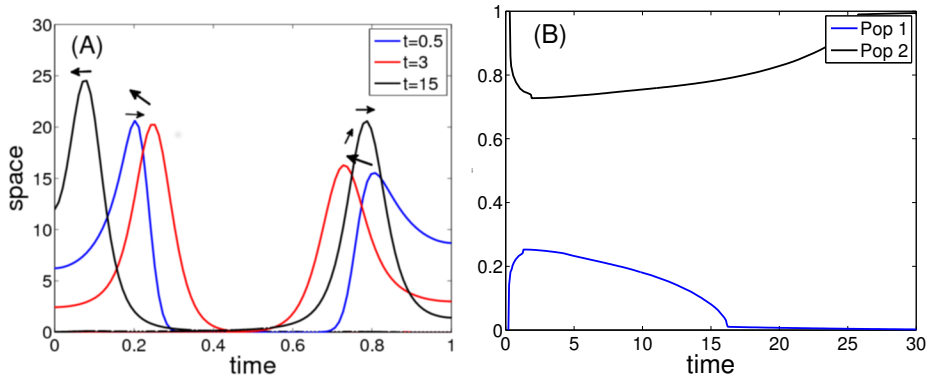

Figure 3.4: Bacterial pulses turn around under the dynamics of system (3.2). The two populations initially move toward one another up the external nutrient gradient. Through a combination of diffusion and consumption, the nutrient gradient quickly becomes sufficiently weak so that the two populations are both attracted backward toward the chemoattractant they left behind. Here the initial food profile is given by the reflected sigmoid (3.3) with $\phi_0 = 18$. (A) Snapshots of the bacterial profiles at different times. Arrows indicate direction of motion. (B) The positions of the peaks of the bacterial pulses over time.

Though these outcomes result from a change in the initial abundance of the nutrient, we note that we can produce similar results by changing other model parameters. For example, if we start from conditions that result in the two populations combining, we can always reduce the chemotactic sensitivity of the bacteria to the nutrient, χ_ϕ, and cause the two populations to turn around. On the other hand, this parameter is unlikely to change from experiment to experiment, and therefore cannot be the reason we observe different outcomes on different trials.

We seek to determine possible causes of these distinct outcomes. We observe that both the combination outcome and the turnaround outcome can be characterized by the relative position of the center of mass of the two bacterial populations: if the centers of mass coalesce, the two populations have combined; if they change direction and accumulated along the opposite boundaries of the domain, the two populations have turned around. In the following section, we derive a system of ordinary differential equations (ODEs) describing the dynamics of the size, center of mass, and variance of the spatial profile of each variable. By explicitly

considering the dynamics of the center of mass, this model facilitates exploration of parameter spaces related to the transient behaviors of the bacterial populations.

3.4 GAUSSIAN APPROXIMATION OF A ONE POPULATION SYSTEM

Here we consider the temporal dynamics of the spatial moments of each variable in a one bacterial population Keller-Segel model (3.1). The i^{th} moment, $i = 0, 1, 2, \ldots$, of the spatial profile of variable $s \in \{b, a, \phi\}$ is defined by

$$s_i(t) = \int_{-\infty}^{\infty} x^i s(x,t) dx.$$

We are primarily concerned with the size, center of mass, and variance of each population. The size of population s is simply s_0, the zeroth moment of that population. The center of mass is given by the formula $\mu_s = s_1/s_0$, and the variance is given by $\sigma_s^2 = s_2/s_0 - \mu_s^2$. Each of these quantities is a function of time only, and therefore differentiation produces an ordinary differential equation describing the temporal dynamics of that quantity. For example, the differential equation governing μ_b is

$$\begin{aligned}
\dot{\mu}_b &= \frac{d}{dt}\left[b_1/b_0\right] \\
&= \frac{1}{b_0}\int_{-\infty}^{\infty} \frac{\partial}{\partial t}\left[xb(t,x)\right] dx \\
&= \frac{1}{b_0}\int_{-\infty}^{\infty} x\left(D_b\frac{\partial^2 b}{\partial x^2} - \chi_a\frac{\partial}{\partial x}\left[b\frac{\partial a}{\partial x}\right] - \chi_\phi\frac{\partial}{\partial x}\left[b\frac{\partial \phi}{\partial x}\right]\right) dx \\
&= \frac{1}{b_0}\left[x\left(D_b\frac{\partial b}{\partial x} - \chi_a b\frac{\partial a}{\partial x} - \chi_\phi b\frac{\partial \phi}{\partial x}\right)\Big|_{-\infty}^{\infty} - \int_{-\infty}^{\infty} D_b\frac{\partial b}{\partial x} - \chi_a b\frac{\partial a}{\partial x} - \chi_\phi b\frac{\partial \phi}{\partial x} dx\right] \\
&= \frac{1}{b_0}\left[0 - D_b b\Big|_{-\infty}^{\infty} + \chi_a\langle ba_x\rangle + \chi_\phi\langle b\phi_x\rangle\right] \\
&= \frac{\chi_a\langle ba_x\rangle + \chi_\phi\langle b\phi_x\rangle}{b_0},
\end{aligned} \tag{3.5}$$

where $1/b_0$ factors out because b_0 is a constant (see system (3.6), below), the boundary terms are zero by assumption, and

$$\langle f(x)g(x)\rangle = \int_{-\infty}^{\infty} f(x)g(x)dx.$$

Similarly differentiating the eight remaining variables produces the following system of nine ODEs:

$$\begin{aligned}
\dot{b}_0 &= 0 \\
\dot{a}_0 &= rb_0 - \delta a_0 \\
\dot{\phi}_0 &= -\kappa\langle b\phi\rangle \\
\dot{\mu}_b &= \frac{\chi_a\langle ba_x\rangle + \chi_\phi\langle b\phi_x\rangle}{b_0} \\
\dot{\mu}_a &= \frac{rb_0}{a_0}(\mu_b - \mu_a) \\
\dot{\mu}_\phi &= -\frac{\kappa}{\phi_0}(\langle xb\phi\rangle - \mu_\phi\langle b\phi\rangle) \\
\dot{\sigma}_b^2 &= 2D_b + 2\frac{\chi_a\langle(x-\mu_b)ba_x\rangle + \chi_\phi\langle(x-\mu_b)b\phi_x\rangle}{b_0} \\
\dot{\sigma}_a^2 &= 2D_a + \frac{rb_0}{a_0}\left(\sigma_b^2 - \sigma_a^2 + (\mu_b - \mu_a)^2\right) \\
\dot{\sigma}_\phi^2 &= 2D_\phi + \frac{\kappa}{\phi_0}\left(\sigma_\phi^2\langle b\phi\rangle - \langle(x-\mu_\phi)^2 b\phi\rangle\right)
\end{aligned} \tag{3.6}$$

The two terms on the right hand side of equation (3.5), $\chi_a\langle ba_x\rangle$ and $\chi_\phi\langle b\phi_x\rangle$, are mixed moments, which cannot be found without knowing the spatial distribution of each population. Indeed, the differential equation for each moment of each variable will generally depend on higher or mixed moments, and we therefore require a method of moment closure.

We observe that the spatial profiles of the bacterial populations in the Keller-Segel model (3.2) both maintain pulsatile, fairly symmetric, Gaussian-like appearances when accumulated in the interior of the spatial domain (see Figures 3.3 and 3.4). We therefore approximate the spatial distribution of each population $s(t,x) \in \{b(t,x), a(t,x), \phi(t,x)\}$ by

$$s(t,x) = \frac{s_0}{\sigma_s\sqrt{\pi}}\exp\left(\frac{-(x-\mu_s)^2}{\sigma_s^2}\right). \tag{3.7}$$

Further, because the pulse-pulse interaction occurs within the interior of the domain, we ignore boundary effects by considering the system on the infinite real line. Approximation (3.7) allows us to evaluate each integral that appears in system (3.6), resulting in an explicit system of ordinary differential equations. In this way, the approximation acts as a method of moment closure.

The behavior of the dynamic variables in system (3.6) describe important aspects of the dynamics of the populations considered in the Keller-Segel model (3.1). In particular,

a change in the direction of μ_b (that is, the sign of $\dot{\mu}_b$) corresponds to a direction reversal of the bacterial population. Similarly, if σ_b^2 is nonzero and small, then the bacteria form a pulse; if σ_b^2 tends to infinity, then the bacterial population diffuses out to a uniform state.

Unless otherwise specified, the initial conditions and parameter values used are those given in the Table 3.2.

	Variable	Initial condition	Natural dimension
b_0	Total bacteria	3	bacterium
a_0	Total chemoattractant	rb_0/δ	mol
ϕ_0	Total nutrient	35	mol
μ_b	Center of mass of bacteria	0	space
μ_a	Center of mass of chemoattractant	0	space
μ_ϕ	Center of mass of nutrient	0.5	space
σ_b^2	Variance of the bacteria profile	0.005	space^2
σ_a^2	Variance of the chemoattractant profile	0.2	space^2
σ_ϕ^2	Variance of the nutrient profile	0.1	space^2
	Parameter	**Value**	**Natural dimension**
D_b	Diffusivity of bacteria	10^{-5}	space^2·time^{-1}
D_a	Diffusivity of attractant	0.0002	space^2·time^{-1}
D_ϕ	Diffusivity of nutrient	0.0002	space^2·time^{-1}
χ_a	Chemotactic sensitivity to attractant	0.00025	space^3·time^{-1}·mol^{-1}
χ_ϕ	Chemotactic sensitivity to nutrient	0.0002	space^3·time^{-1}·mol^{-1}
r	Production rate of attractant by bacteria	0.05	mol·bacterium^{-1}·time^{-1}
δ	Natural decay rate of attractant	0.005	time^{-1}
κ	Consumption rate of nutrient by bacteria	0.001	(bacterium/space)$^{-1}$·time^{-1}

Table 3.2: System variables and parameters used in system (3.6).

Before we explore the mechanisms responsible for the turnaround of the bacteria in a one-dimensional nutrient gradient, we explore the extent of the qualitative agreement between

the Keller-Segel model (3.1) and system (3.6).

3.4.1 Stability of uniform state

While we cannot expect perfect quantitative agreement between model (3.1) and system (3.6), we can confirm that (3.6) reproduces key qualitative behaviors of (3.1). We first consider the linear stability of all equilibrium points of system (3.6). The differential equation for μ_a indicates that we must have $\mu_b = \mu_a$ at any equilibrium point, but the specific value of these two variables is arbitrary (in other words, the bacterial and chemical pulse must accumulate around the same spatial coordinate, but that coordinate can be anywhere). We therefore introduce the relative coordinate $\mu = \mu_b - \mu_a$. Further, we note that any steady state requires $\phi_0 = 0$. Under this transformation and condition, evaluating the integrals remaining in system (3.6) after imposing assumption (3.7) produces

$$\begin{aligned}
\dot{b}_0 &= 0 \\
\dot{a}_0 &= rb_0 - \delta a_0 \\
\dot{\mu} &= \left[\frac{-2\chi_a a_0}{\sqrt{\pi}(\sigma_b^2 + \sigma_a^2)^{3/2}} \exp\left(\frac{-\mu^2}{\sigma_b^2 + \sigma_a^2} \right) - \frac{rb_0}{a_0} \right] \mu \\
\dot{\sigma}_b^2 &= 2D_b - 2\frac{\chi_a a_0 \sigma_b^2}{\sqrt{\pi}(\sigma_b^2 + \sigma_a^2)^{5/2}} \left(\sigma_b^2 + \sigma_a^2 - 2\mu^2 \right) \exp\left(\frac{-\mu^2}{\sigma_b^2 + \sigma_a^2} \right) \\
\dot{\sigma}_a^2 &= 2D_a + \frac{rb_0}{a_0}(\sigma_b^2 - \sigma_a^2 + \mu^2).
\end{aligned} \tag{3.8}$$

From the first two equations, any fixed point of this system must satisfy $b_0^* = constant$ and $a_0^* = rb_0^*/\delta$. Since the term inside the brackets in the μ equation is strictly negative, any fixed point must also satisfy $\mu = 0$. The remaining two-variable system is

$$\begin{aligned}
\dot{\sigma}_b^2 &= 2\left(D_b - \frac{\chi_a r b_0^* \sigma_b^2}{\sqrt{\pi}\delta(\sigma_b^2 + \sigma_a^2)^{3/2}} \right) \\
\dot{\sigma}_a^2 &= 2D_a + \delta(\sigma_b^2 - \sigma_a^2).
\end{aligned} \tag{3.9}$$

The generic cases of the nullclines for system (3.9) are plotted in Figure 3.5. In Figure 3.5A, the total amount of bacteria is $b_0 = 0.01$ and the system contains no fixed points. The variance of both populations generically blows up to infinity as time gets large for any initial condition; that is, the bacterial population will always diffuse out into a uniform state if the

population size is too low. As b_0 surpasses some critical threshold b_0^*, the system undergoes a saddle-node bifurcation (Figure 3.6). In Figure 3.5B, b_0 is increased to 0.012, and a stable node and a saddle point now exist. The stable equilibrium point is analogous to the pulse solution of system (3.1): the bacterial population and its chemoattractant accumulate around the same center of mass ($\mu = \mu_b - \mu_a = 0$) with a small variance around this point. Consequently, the threshold b_0^* is analogous to the critical threshold (3.4) of the Keller-Segel model (3.1), above which the bacteria are able to aggregate into a pulse. In the approximate system (3.6), however, if the initial bacterial variance that is too large (that is, to the right of the separatrix of the saddle point), then the variance of both populations increases without bound. This case is analogous to the system diffusing out to the uniform solution, and so system (3.6) is generically bistable when b_0 is above a critical threshold.

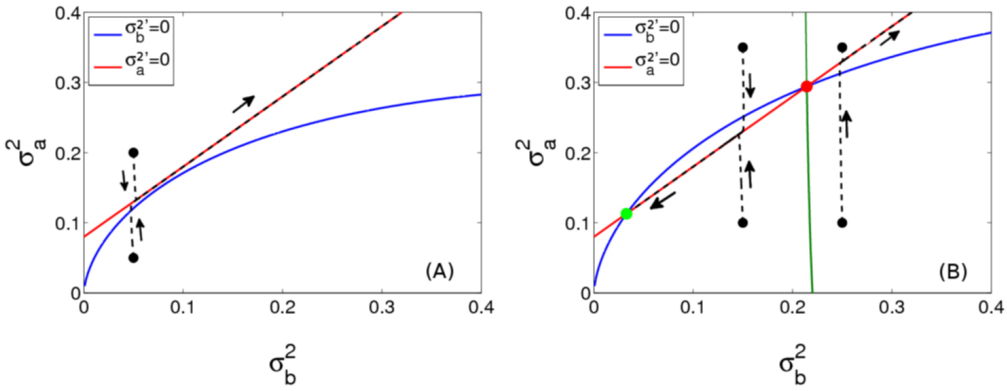

Figure 3.5: Phase plane of system (3.9) describing steady states of the Gaussian approximation system. (A) The bacterial size $b_0 = 0.01$ is below the critical threshold b_0^*. Trajectories approach the σ_a^2-nullcline and then both σ_a^2 and σ_b^2 tend to infinity. (B) The bacterial population size $b_0 = 0.012$ is above the critical threshold b_0^*. The left-most equilibrium point is a stable node. The right-most equilibrium point is a saddle, the stable manifold of which is shown as the green curve. To the left of this stable manifold, trajectories tend toward the stable node, and the bacteria consequently form a pulse. To the right of the manifold, trajectories tend to infinity, and the bacteria diffuse out to the uniform solution. Arrows in both panels indicate the direction of flow.

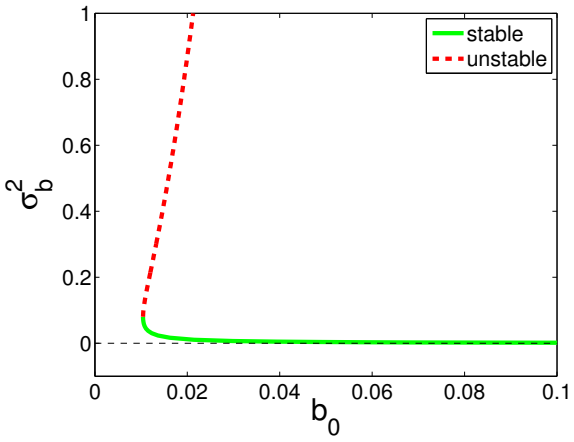

Figure 3.6: Bifurcation diagram of system (3.9). The green curve corresponds to the σ_b^2 coordinate of the stable node, and the red dashed curve corresponds to the σ_b^2 coordinate of the saddle point. The σ_b^2 coordinate of the saddle point increases with b_0, and consequently the separatrix in Figure 3.5 gets pushed farther to the right.

We can explicitly calculate the critical population size b_0^* at which the saddle-node bifurcation occurs as a function of system parameters. The nullclines of system (3.9) intersect when

$$D_b - \frac{\chi_a r b_0 \sigma_b^2}{\sqrt{\pi}\delta(2\sigma_b^2 + 2D_a/\delta)^{3/2}} = 0,$$

or equivalently,

$$(\sigma_b^2)^3 + \left(3\frac{D_a}{\delta} - \frac{\chi_a^2 r^2 b_0^2}{8\pi\delta^2 D_b^2}\right)(\sigma_b^2)^2 + \frac{3D_a^2}{\delta^2}\sigma_b^2 + \frac{D_a^3}{\delta^3} = 0. \tag{3.10}$$

When

$$3\frac{D_a}{\delta} - \frac{\chi_a^2 r^2 b_0^2}{8\pi\delta^2 D_b^2} = -\frac{15}{4}\frac{D_a}{\delta}, \tag{3.11}$$

Equation (3.10) can be written

$$\left(\sigma_b^2 - 2\frac{D_a}{\delta}\right)^2 \left(\sigma_b^2 + \frac{D_a}{4\delta}\right) = 0,$$

and therefore equation (3.11) is the condition for when the two positive roots of (3.10) coalesce. This condition gives us the critical bifurcation value for b_0,

$$b_0^* = \frac{D_b\sqrt{54\pi D_a\delta}}{r\chi_a}. \tag{3.12}$$

If $b_0 > b_0^*$, then equation (3.10) has two roots and a stable pulse solution of system (3.16) exists, and if $b_0 < b_0^*$, then the equation has no roots and the uniform state is the only asymptotic solution of the system. Comparison to the critical value of b^{tot} in the Keller-Segel system (3.1),

$$b^{tot} = \frac{D_b(\pi^2 D_a + \delta)}{r\chi_a},$$

shows that a change in any of the system parameters for (3.6) produces the same qualitative effect on the threshold as in the PDE model (3.1).

In the following section, we introduce a similar approximation to the dynamics of a two-population system and show that the asymptotic dynamics and critical threshold remain qualitatively unchanged.

3.5 TWO-POPULATION GAUSSIAN APPROXIMATION

For the purposes of analyzing the behavior of interacting bacterial populations, we introduce a second bacterial population β and corresponding chemoattractant concentration α, both of which we again assume maintain a Gaussian profile. The dynamics governing b and β are identical: both are mutually attracted by chemotaxis up both chemoattractant gradients and the nutrient gradient and they diffuse at the same rate. With the addition of these variables, the system we study becomes

$$
\begin{aligned}
\dot{b}_0 &= 0 \\
\dot{a}_0 &= rb_0 - \delta a_0 \\
\dot{\beta}_0 &= 0 \\
\dot{\alpha}_0 &= r\beta_0 - \delta\alpha_0 \\
\dot{\phi}_0 &= -\kappa\langle b\phi\rangle - \kappa\langle\beta\phi\rangle \\
\dot{\mu}_b &= \frac{\chi_a\langle ba_x\rangle + \chi_a\langle b\alpha_x\rangle + \chi_\phi\langle b\phi_x\rangle}{b_0} \\
\dot{\mu}_a &= \frac{rb_0}{a_0}(\mu_b - \mu_a) \\
\dot{\mu}_\beta &= \frac{\chi_a\langle\beta a_x\rangle + \chi_a\langle\beta\alpha_x\rangle + \chi_\phi\langle\beta\phi_x\rangle}{\beta_0} \\
\dot{\mu}_\alpha &= \frac{r\beta_0}{\alpha_0}(\mu_\beta - \mu_\alpha) \\
\dot{\mu}_\phi &= -\frac{\kappa}{\phi_0}(\langle xb\phi\rangle - \mu_\phi\langle b\phi\rangle) - \frac{\kappa}{\phi_0}(\langle x\beta\phi\rangle - \mu_\phi\langle\beta\phi\rangle) \\
\dot{\sigma}_b^2 &= 2D_b + 2\frac{\chi_a\langle(x-\mu_b)ba_x\rangle + \chi_a\langle(x-\mu_b)b\alpha_x\rangle + \chi_\phi\langle(x-\mu_b)b\phi_x\rangle}{b_0} \\
\dot{\sigma}_a^2 &= 2D_a + \frac{rb_0}{a_0}\left(\sigma_b^2 - \sigma_a^2 + (\mu_b - \mu_a)^2\right) \\
\dot{\sigma}_\beta^2 &= 2D_b + 2\frac{\chi_a\langle(x-\mu_\beta)\beta a_x\rangle + \chi_a\langle(x-\mu_\beta)\beta\alpha_x\rangle + \chi_\phi\langle(x-\mu_\beta)\beta\phi_x\rangle}{\beta_0} \\
\dot{\sigma}_\alpha^2 &= 2D_a + \frac{r\beta_0}{\alpha_0}\left(\sigma_\beta^2 - \sigma_\alpha^2 + (\mu_\beta - \mu_\alpha)^2\right) \\
\dot{\sigma}_\phi^2 &= 2D_\phi + \frac{\kappa}{\phi_0}\left(\sigma_\phi^2\langle b\phi\rangle + \sigma_\phi^2\langle\beta\phi\rangle - \langle(x-\mu_\phi)^2 b\phi\rangle - \langle(x-\mu_\phi)^2\beta\phi\rangle\right).
\end{aligned}
\tag{3.13}
$$

We will first show that the asymptotic dynamics of system (3.13) are qualitatively the same at the analogous one-population system (3.6), namely that any equilibrium point of system (3.13) requires that $\mu_b = \mu_\beta = \mu_a = \mu_\alpha$. As in system (3.6), the external nutrient population is entirely transient, $\phi_0 \to 0$ as $t \to \infty$, so the nutrient will not affect asymptotic stability. From the first four equations of system (3.13), we have that $a_0^* = rb_0^*/\delta$ and $\alpha_0^* = r\beta_0^*/\delta$ at any equilibrium point, where b_0^* and β_0^* are constants. Moreover, the μ_a and

μ_α equations require that $\mu_b = \mu_a$, and $\mu_\beta = \mu_\alpha$, respectively. We introduce the relative center of mass coordinate $\mu_{b\beta} = \mu_b - \mu_\beta$, which is then governed by the differential equation

$$\begin{aligned}
\dot{\mu}_{b\beta} &= -\frac{2\chi_a r\beta_0(\mu_b-\mu_\alpha)}{\delta\sqrt{\pi}(\sigma_b^2+\sigma_\alpha^2)^{3/2}}\exp\left(\frac{-(\mu_b-\mu_\alpha)^2}{\sigma_b^2+\sigma_\alpha^2}\right)+\frac{2\chi_a r b_0(\mu_\beta-\mu_a)}{\delta\sqrt{\pi}(\sigma_\beta^2+\sigma_a^2)^{3/2}}\exp\left(\frac{-(\mu_\beta-\mu_a)^2}{\sigma_\beta^2+\sigma_a^2}\right)\\
&= -\frac{2\chi_a r\beta_0(\mu_b-\mu_\beta)}{\delta\sqrt{\pi}(\sigma_b^2+\sigma_\alpha^2)^{3/2}}\exp\left(\frac{-(\mu_b-\mu_\beta)^2}{\sigma_b^2+\sigma_\alpha^2}\right)+\frac{2\chi_a r b_0(\mu_\beta-\mu_b)}{\delta\sqrt{\pi}(\sigma_\beta^2+\sigma_a^2)^{3/2}}\exp\left(\frac{-(\mu_\beta-\mu_b)^2}{\sigma_\beta^2+\sigma_a^2}\right)\\
&= -\frac{2\chi_a r\beta_0\mu_{b\beta}}{\delta\sqrt{\pi}(\sigma_b^2+\sigma_\alpha^2)^{3/2}}\exp\left(\frac{-\mu_{b\beta}^2}{\sigma_b^2+\sigma_\alpha^2}\right)+\frac{2\chi_a r b_0(-\mu_{b\beta})}{\delta\sqrt{\pi}(\sigma_\beta^2+\sigma_a^2)^{3/2}}\exp\left(\frac{-\mu_{b\beta}^2}{\sigma_\beta^2+\sigma_a^2}\right)\\
&= \left(-\frac{2\chi_a r\beta_0}{\delta\sqrt{\pi}(\sigma_b^2+\sigma_\alpha^2)^{3/2}}\exp\left(\frac{-\mu_{b\beta}^2}{\sigma_b^2+\sigma_\alpha^2}\right)-\frac{2\chi_a r b_0}{\delta\sqrt{\pi}(\sigma_\beta^2+\sigma_a^2)^{3/2}}\exp\left(\frac{-\mu_{b\beta}^2}{\sigma_\beta^2+\sigma_a^2}\right)\right)\mu_{b\beta}.
\end{aligned} \tag{3.14}$$

The expression multiplying $\mu_{b\beta}$ is strictly negative, and so $\dot{\mu}_{b\beta} = 0$ if and only if $\mu_{b\beta} = 0$. We have therefore shown that, at steady state, we must have $\mu_a = \mu_b = \mu_\beta = \mu_\alpha$.

The remaining dynamical variables are governed by the system

$$\begin{aligned}
\dot{\sigma}_b^2 &= 2D_b - 2\frac{\chi_a r b_0\sigma_b^2}{\delta\sqrt{\pi}(\sigma_b^2+\sigma_a^2)^{3/2}} - 2\frac{\chi_a r\beta_0\sigma_b^2}{\delta\sqrt{\pi}(\sigma_b^2+\sigma_\alpha^2)^{3/2}}\\
\dot{\sigma}_a^2 &= 2D_a + \delta(\sigma_b^2-\sigma_a^2)\\
\dot{\sigma}_\beta^2 &= 2D_b - 2\frac{\chi_a r b_0\sigma_\beta^2}{\delta\sqrt{\pi}(\sigma_\beta^2+\sigma_a^2)^{3/2}} - 2\frac{\chi_a r\beta_0\sigma_\beta^2}{\delta\sqrt{\pi}(\sigma_\beta^2+\sigma_\alpha^2)^{3/2}}\\
\dot{\sigma}_\alpha^2 &= 2D_a + \delta(\sigma_\beta^2-\sigma_\alpha^2).
\end{aligned} \tag{3.15}$$

If we make the additional simplifying assumptions that the two bacterial populations are of the same size (that is, $b_0 = \beta_0$) and have the same initial variance, and the two chemoattractant populations have the same initial variance, then the first two equations are identical to the second two equations in system (3.15), and consequently $\sigma_b^2 = \sigma_\beta^2$ for all time (these assumptions ease analysis but are not necessary to achieve the results presented below; see Discussion). Imposing these conditions, system (3.15) reduces to the two-dimensional system

$$\begin{aligned}
\dot{\sigma}_b^2 &= 2\left(D_b - 2\frac{\chi_a r b_0\sigma_b^2}{\delta\sqrt{\pi}(\sigma_b^2+\sigma_a^2)^{3/2}}\right)\\
\dot{\sigma}_a^2 &= 2D_a + \delta(\sigma_b^2-\sigma_a^2).
\end{aligned} \tag{3.16}$$

This system is nearly identical to system (3.9), the only difference being that the second term inside the parentheses in the first equation is doubled in (3.16) because there are now two bacterial populations producing chemoattractant. System (3.13) therefore produces the same saddle-node bifurcation structure as the one-population system (3.6). We note that the same bifurcation will occur if the two populations are not of equal size, though the mathematical details become tedious and no more informative than this simplified case.

As with model (3.2), we will only consider regimes under which the bacterial population maintains a size above the critical threshold b_0^* and can therefore maintain a pulse. Two example outcomes of simulations of system (3.13) demonstrating agreement with the experimentally observed outcomes are shown in Figures 3.7 and 3.8. The only difference between the two simulations was the initial condition for shared nutrient, ϕ_0. In Figure 3.7, $\phi_0(0) = 35$, and the two populations combine; in Figure 3.8, $\phi_0(0) = 25$, and the two populations turn around and separately accumulates into meta-stable pulses (see Section 3.6). The parameters chosen in both simulations are those in Table 3.2. The results shown in Figures 3.7 and 3.8 are consistent with the results from Section 3.3 of simulations of the Keller-Segel model (3.2): increasing the initial amount of external nutrient caused the bacteria to switch from a regime in which they turn around to one in which they combine (Figures 3.3 and 3.4).

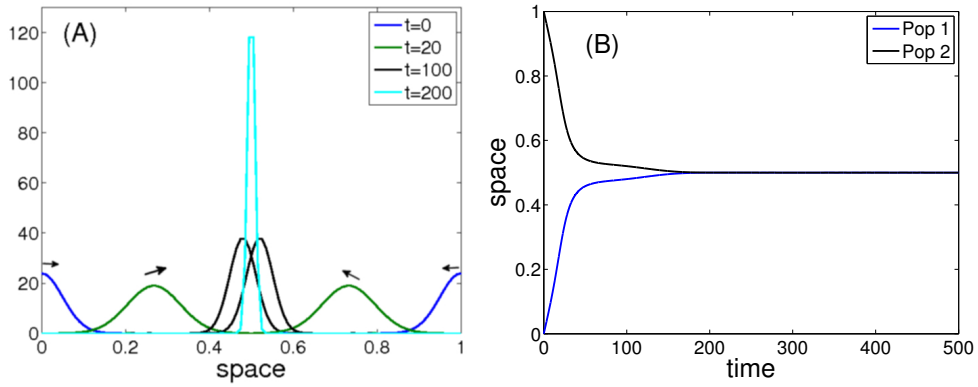

Figure 3.7: Bacterial pulses combine under the dynamics of system (3.13). The two populations move toward one another up the external nutrient gradient until they collide and combine to form a single pulse. The initial amount of nutrient is $\phi_0(0) = 35$. (A) Snapshots of the bacterial spatial profiles at different times, given by (3.7). The arrows indicate direction of motion. (B) The positions of the peaks of the bacterial pulses over time.

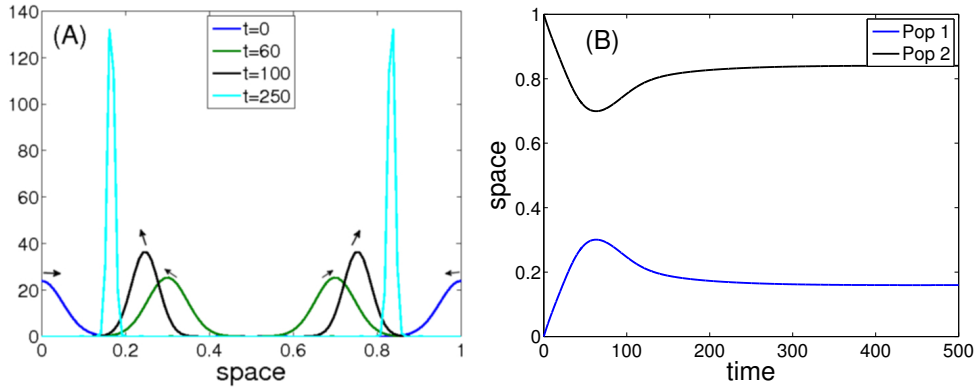

Figure 3.8: Bacterial pulses turn under the dynamics of system (3.13). The two populations initially move toward one another up the external nutrient gradient but later change direction and move back toward their own accumulated chemoattractant to form separate meta-stable pulses. The initial amount of nutrient is $\phi_0(0) = 25$. (A) Snapshots of the bacterial spatial profiles at different times, given by (3.7). The arrows indicate direction of motion. (B) The positions of the peaks of the bacterial pulses over time.

Our simulations confirm that a change to the initial amount of available nutrient can

cause a change in the outcome of the bacterial interaction. Variations in other parameters can have similar effects on the bacterial behavior. In the following section, we explore the effects of specific parameters and determine regions in various parameter spaces that correspond to each outcome.

3.6 PREDICTING TURNAROUND

We are particularly concerned with the behavior of the center of mass of the bacterial population, μ_b (and equivalently μ_β). One significant advantage of system (3.13) over the two-population Keller-Segel model (3.2) in this regard is that system (3.13) explicitly includes the time derivative of this center of mass and thus allows us to separately consider the effects that the chemotactic attraction to the chemoattractant and to the external nutrient have on its motion.

The differential equation for μ_b is

$$\begin{aligned}\dot{\mu}_b &= \frac{\chi_a\langle ba_x\rangle + \chi_a\langle b\alpha_x\rangle + \chi_\phi\langle b\phi_x\rangle}{b_0} \\ &= -\frac{2\chi_a a_0(\mu_b-\mu_a)}{\sqrt{\pi}(\sigma_b^2+\sigma_a^2)^{3/2}}\exp\left(\frac{-(\mu_b-\mu_a)^2}{\sigma_b^2+\sigma_a^2}\right) - \frac{2\chi_a\alpha_0(\mu_b-\mu_\alpha)}{\sqrt{\pi}(\sigma_b^2+\sigma_\alpha^2)^{3/2}}\exp\left(\frac{-(\mu_b-\mu_\alpha)^2}{\sigma_b^2+\sigma_\alpha^2}\right) \\ &\quad - \frac{2\chi_\phi\phi_0(\mu_b-\mu_\phi)}{\sqrt{\pi}(\sigma_b^2+\sigma_\phi^2)^{3/2}}\exp\left(\frac{-(\mu_b-\mu_\phi)^2}{\sigma_b^2+\sigma_\phi^2}\right),\end{aligned} \tag{3.17}$$

where each of the three terms in the sum in the right hand side of (3.17) can be interpreted, in order, as the rate of change in position of the center of mass of b due to its own chemoattractant, due to the other population's chemoattractant, and due to the external nutrient, respectively. Since we assume that $\mu_b(0) = \mu_a(0) = 0$, $\mu_\phi(0) = 0.5$, and $\mu_\beta(0) = \mu_\alpha(0) = 1$, we have that $\dot{\mu}_b(0) > 0$ and $\dot{\mu}_a(0) = 0$. The center of mass of the bacteria is therefore generically ahead (with respect to the direction of motion) of the center of mass of the chemoattractant for early time. We can now apprehend the mechanism that allows for the bacteria to turn around: the bacteria are attracted inward toward the nutrient and the second population's chemoattractant and outward by their own chemoattractant. If

the outward attraction is stronger than the inward attraction, then the bacteria will turn around.

Upon inspecting equation (3.17), it is clear that the chemotactic pull toward any given substance is related to the chemotactic sensitivity to the substance (χ_a and χ_ϕ), the distance between the center of mass of the bacterial population and that of the substance, the variance of the substance pulse, and the total amount of the substance present. Since the latter three quantities are dynamic variables, direct analysis of their effects on the transient behavior of μ_b is not viable. Instead, we consider the effects of parameters related to the dynamics of these variables.

Our goal in studying system (3.13) is to determine parameter conditions under which the two populations combine and those under which they turn around. Because equilibria require that $\mu_b = \mu_\beta$, the two populations will necessarily combine in asymptotic time, in contrast to the Keller-Segel model (3.2). We therefore must take care in deciding what qualifies as a turnaround in system (3.13). One possible condition is that $\dot{\mu}_b(t_1) = 0$ and $\dot{\mu}_\beta(t_2) = 0$ for some times t_1 and t_2 (indicating that the centers of mass of both populations have changed direction). However, this condition is not sufficient to determine when the populations turn around and move away from one another. Figure 3.9 shows an example where both populations quickly turn around, but shortly thereafter turn back around and combine. Though the center of mass of each population does change direction in this example, the overall outcome is not compatible with experimentally observed turnaround, in which the two populations accumulate along opposite ends of the domain. We therefore adopt the following more robust definition of turnaround.

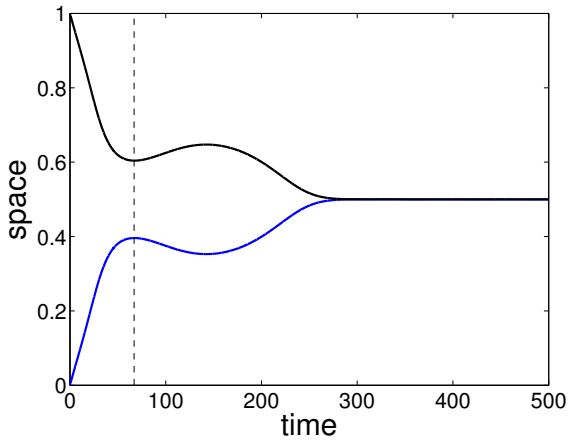

Figure 3.9: False turnaround. The vertical dashed line marks a turnaround in the center of mass of both populations, but the populations combine together a short time later.

The chemotactic attraction of a bacterial population decays exponentially with the distance between the center of mass of the bacteria and that of the chemoattractant (see equation (3.14)). Thus, if the two bacterial populations are sufficiently far apart, then the chemotactic pull from each pulse of chemoattractant to the more distant bacterial population is negligible, and the populations can separately approach a meta-stable state: each population asymptotes into it own pulse-like structure, subject to only an exponentially small effect from the other population's chemoattractant. This state is intuitively consistent with the experimental state in which two bacterial populations accumulate along the boundaries of the domain. In asymptotic time, the two populations will always combine, but the farther apart the two populations are, the longer it will take for the combination to occur. Once the populations do become sufficiently close, however, the relative effect that each population experiences from the other population's chemoattractant becomes nontrivial, and they combine together relatively quickly. We therefore reason that if the two populations have not combined after a large but finite amount of time, they must be in a meta-stable non-combined state. We therefore take as our condition for turnaround that the centers of mass of the two populations are distinct after a large amount of time; that is, that $|\mu_b(t_c) - \mu_\beta(t_c)| > \epsilon$ for some small, fixed distance ϵ at some large time $t = t_c$.

We must take care in choosing values for ϵ and t_c. For instance, in order to establish a

boundary between the turnaround outcome and the combination outcome, we must choose ϵ small enough so that the two populations will quickly combine if their center of masses are ϵ apart. We determine through numerical simulation that when the distance between the center of masses reaches $\epsilon = 0.1$, that distance decreases monotonically and quickly. Similarly, we must choose t_c large enough to guarantee that the system did in fact reach a meta-stable state and to avoid a false turnaround, as illustrated in Figure 3.9. Figure 3.10 shows the time $t = t_c$ at which the two populations will be $\epsilon = 0.1$ apart over varied parameter values. In each panel, the curve defines a boundary. For example, if $\phi_0(0)$ is to the right of the curve in the first panel, then the two populations will be ϵ apart sooner than t_c. In each case, the curve becomes very steep near a critical parameter value. Consequently, as long we choose t_c sufficiently large, our choice will not have much impact on the parameter value that defines our boundary. Guided by this reasoning, we choose to take as our condition for turnaround that the centers of the two populations are $\epsilon = 0.1$ units away from one another at $t_c = 500$.

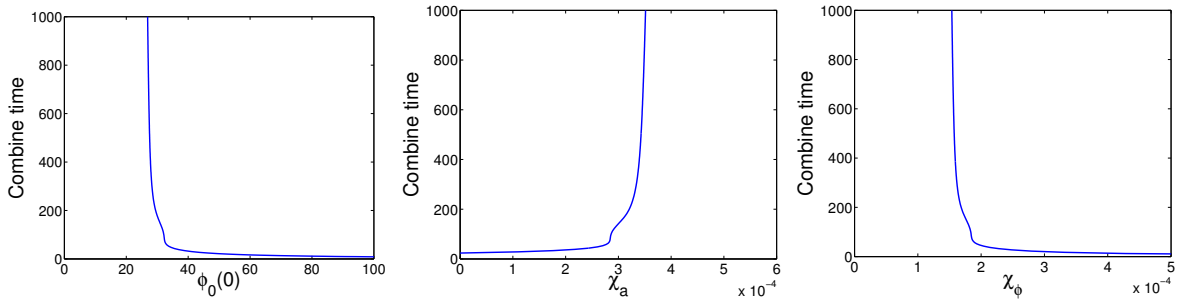

Figure 3.10: Dependence of time to combine on system parameters. In order to combine at time t, the parameter on the horizontal axis must be the value specified by the curve. Sensitivity of the time to combine t_c on each parameter considered decreases once t_c exceeds some quantitative threshold. Similar figures for parameters N_0 and D not shown.

To apply this condition, we solve a modification of system (3.13) as a boundary value problem with boundary condition $|\mu_b - \mu_\beta| = \epsilon = 0.1$ at time $t = 500$. To satisfy all boundary conditions, we must consider one of the pertinent parameters as a stationary variable. For example, to determine the effect of χ_a on the transient behavior, we include the differential

equation $\chi_a' = 0$ in the system. We then use the continuation software AUTO to solve this boundary value problem across a varied parameter. The solution curve in parameter space defines a boundary between regions in which our system predicts the bacteria turn around and in which it predicts they combine.

Figure 3.11 shows the results of solving this boundary value problem. In this figure, $N_0 = b_0 = \beta_0$, $D = D_b$, and $D_a = D_\phi = 20 \times D$. Each panel shows a given parameter space divided into two regions. Parameter pairs chosen from the grey region in each panel represent a regime in which the two *E. coli* populations turn around; parameters chosen from the white region correspond to a regime in which they combine. These figures provide a picture of the relative contributions of the parameters considered. For example, Figure 3.11A shows that if the bacterial population size is increased, more external nutrient is needed to result in the bacterial populations combining. This is easy to understand: if the bacterial populations are larger, then they produce more chemoattractant, and the outward attraction toward the bacteria's own chemoattractant will be stronger, requiring a stronger inward attraction toward the nutrient to result in combination. Our simulations presented in Figure 3.7 and 3.8 agree with this prediction. The parameters chosen in Figure 3.7 correspond to the black circle in Figure 3.11 and resulted in a combination of the two pulses; the parameters in Figure 3.8 correspond to the black square and results in the pulses turning around.

Figures 3.11B and C are more subtle. Increasing D can be interpreted as, for example, decreasing the viscosity of the medium in which the bacteria are suspended, thereby increasing the diffusivity of the bacterial and chemical populations. Figure 3.11B shows that the higher the diffusion rate, the less initial nutrient is necessary to cause the bacterial population to combine. For too fluid of a medium, the chemoattractant of both populations spreads quickly across the spatial domain to reach the other population. This results in a mutual attraction of both populations toward one another, and the external nutrient is no longer needed to pull both populations inward. Figure 3.11C similarly shows that in order for the two populations to turn around when diffusivity is high, they need a large initial population resulting in a large initial supply of chemoattractant.

Figure 3.11D shows the chemotactic sensitivity of the bacteria toward the chemoattractant, χ_a, versus the sensitivity toward the nutrient, χ_ϕ. While these parameters do not

change from trial to trial, this figure is easily interpreted and agrees with intuition: a strong attraction toward the nutrient will always result in the bacterial populations being pulled quickly inward and combining. If the attraction toward the chemoattractant is sufficiently high relative to the attraction toward the nutrient, then the bacteria will be pulled strongly outward toward their previously accumulated chemoattractant and hence will turn around.

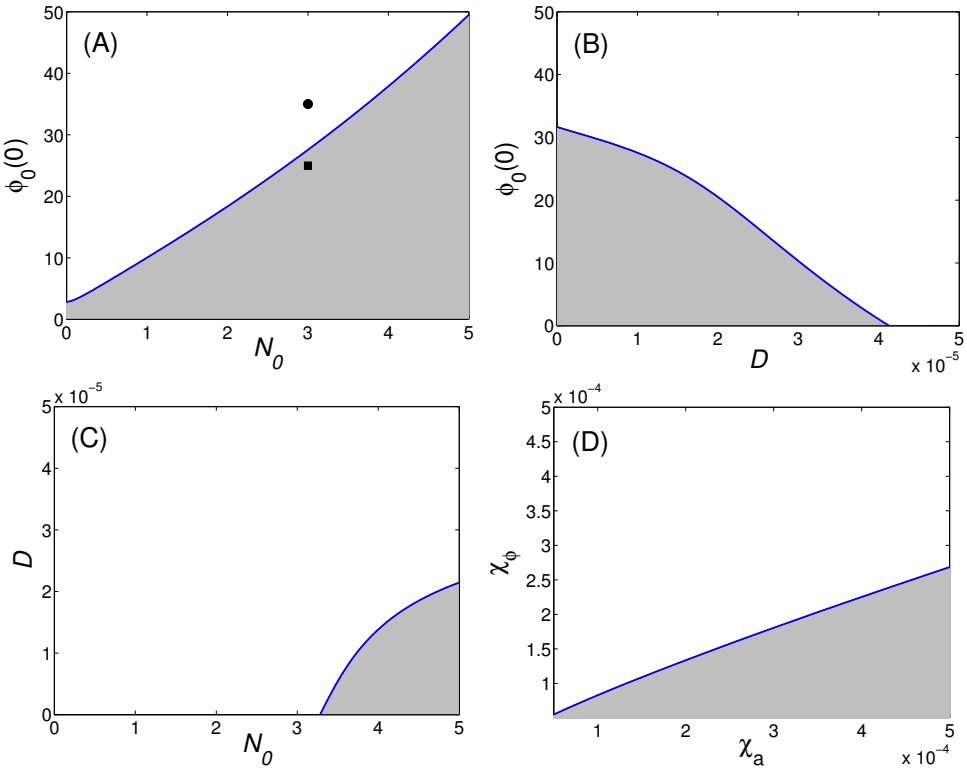

Figure 3.11: Boundaries in parameter space between combination (white) and turnaround (grey). The black circle and square in panel A correspond to the parameter values chosen in Figures 3.7 and 3.8, respectively. The criterion for combination is $\mu_b - \mu_\beta = 0$ before $t = 500$. Whenever a parameter is not varied, $N_0 = 3$, $D = 10^{-5}$, $\chi_a = 0.00025$, $\chi_\phi = 0.0002$, and $\phi_0(0) = 35$.

3.7 DISCUSSION

In this chapter, we study the interaction of bacterial pulses in a one-dimensional nutrient gradient. We present experimental results due to the Salman laboratory in which two identical populations of *E. coli* moving toward one another up a nutrient gradient change direction and move back in the direction they came from, rather than continuing toward each other to combine into one indistinguishable population. We capture this turn-around behavior analytically using the classic Keller-Segel model for bacterial chemotaxis. We then use a heuristic argument to develop a system of ordinary differential equations approximating the spatio-temporal dynamics of the Keller-Segel model. Our approximation facilitates the study of the global dynamics of the system and the exploration of effects of parameter variation on population dynamics. After verifying that the approximating system agrees qualitatively with both experiment and with the Keller-Segel model, we define a condition on system parameters that determines whether the bacterial populations will combine or turn around, then develop and numerically solve a boundary value problem to find the boundary in various parameter spaces separating these two outcomes.

Our results leave us with predictions about the mechanisms by which the *E. coli* populations manage to turn around and move away from each other and the nutrient gradient. System (3.6) shows that the center of mass of a bacterial population is generically between the center of mass of its chemoattractant and that of the external nutrient for early time. This allows the bacteria to turn around if the outward attraction toward the chemoattractant is stronger than the inward attraction toward the nutrient. Outward attraction can overcome inward attraction in a number of ways. For example, if the amount of chemoattractant accumulated on the edges of the spatial domain is large relative to the amount of nutrient between the bacterial populations, our approximating system predicts the bacteria will turn back toward the attractant. If the medium in which the bacteria are suspended is too fluid, our system predicts that the two bacterial populations will likely combine, because the chemoattractant will spread across the spatial domain, removing the driver of the direction reversal. Variations in the total amount of available nutrient or fluidity of the medium can therefore lead to qualitative changes in the behavior of the bacteria.

The predictions made by our approximate system agree qualitatively with the the Keller-Segel model. Figures 3.3 and 3.4 in Section 3.3 show that decreasing the initial amount of nutrient can cause the bacterial populations to switch from a combination outcome to a turnaround outcome. Similarly, increasing the diffusivity of all three populations results in the bacterial populations combining (results not shown). This agreement suggests that our Gaussian approximation system offers reasonable predictions to be tested experimentally.

Our analysis of the two population system assumed that both bacterial populations were of equal size. This assumption simplified our analysis by reducing the number of free parameters, but might be unrealistic, as population size could vary between the two populations during an experiment. Simulations of system (3.13) with unequal but similar population sizes agree qualitatively with those presented in this chapter, and the dynamics we observed are therefore not a result of perfect symmetry in the populations.

Previous works have derived approximate ODE systems to analyze the interaction of pulses in reaction-diffusion models [25, 45, 87]. These works use asymptotic matching methods to derive first-order approximation for an ODE describing the dynamics of the distance between slowly varying spike peaks. The stability of the origin of the resulting ODE determines whether the two pulses are predicted to combine or repel. However, this framework depends heavily on the dynamics of the pulses being slow, and does not allow for analysis of the transient behavior of pulses. Our approximating system and the method used to derive it provide an efficient and tractable framework for analyzing the transient dynamics of complex systems. A similar analysis was conducted in [2], in which the authors used singular perturbation techniques to derive a Lotka-Volterra-like ODE competition model between invasive bacteria and host leukocytes from a Keller-Segel system adapted to model the inflammation response due to bacterial infection. The resulting approximated system allowed the authors to conduct an analysis of the global behavior of the system as a function of model parameters, but removed all spatial aspects of the system. Our approximation preserves the spatial dimension by considering the temporal dynamics of the key quantities that characterize spatial features of our model populations.

There a several open directions related to this study. The first is to explore other, more quantitatively accurate approximations to the population distributions. While the bacteria

maintains a Gaussian pulse-like distribution in the Keller-Segel model, the chemoattractant and nutrient populations do not necessarily do the same, especially as two populations interact. One could impose a different assumption on the distribution of the chemical populations, the results of which could be important in understanding the transient behavior we studied in this chapter. An improvement could be made through better parameter fitting. Our study is primarily qualitative in flavor, and a more quantitatively accurate approximation could produce more precise experimental predictions. Our heuristic approximation could easily be applied as a method of moment closure for other spatio-temporal models whose nonlinearities make parameter exploration and transient analysis tedious or impossible. Finally, it would be interesting to apply our Gaussian approximation method to a two-dimensional Keller-Segel model and explore transient dynamics, asymptotic states, and pattern formation.

3.8 APPENDIX: ANALYSIS OF KELLER-SEGEL MODEL

3.8.1 Stability of uniform solution

Here we perform linear stability analysis of the uniform solution of system (3.2),

$$\begin{aligned} b_1 &= b_1^* \\ b_2 &= b_2^* \\ a &= \frac{r}{\delta}(b_1^* + b_2^*) \\ \phi &= 0. \end{aligned} \tag{3.18}$$

Since the only steady state solution of the external nutrient is $\phi = 0$, ϕ cannot affect the asymptotic stability of steady state solutions. Therefore, to study the stability of the uniform solution of system (3.2), we can instead study the uniform steady state of system

(3.1); that is, constant solutions of the system

$$\begin{aligned} 0 &= D_b \frac{\partial^2 b}{\partial x^2} - \chi_a \frac{\partial}{\partial x}\left[b \frac{\partial a}{\partial x}\right] \\ 0 &= D_a \frac{\partial^2 a}{\partial x^2} + rb - \delta a \\ \left.\frac{\partial b}{\partial x}\right|_{x=0,1} &= \left.\frac{\partial a}{\partial x}\right|_{x=0,1} = 0. \end{aligned} \tag{3.19}$$

System (3.19) admits the trivial solution

$$\begin{aligned} b &= b_0 \\ a &= \frac{r}{\delta} b_0, \end{aligned} \tag{3.20}$$

where b_0 is a positive constant.

Following the technique described in, for example, [26, 55], we linearize system (3.19) about the solution (3.20). We assume that to first order stationary solutions are of the form

$$\begin{aligned} b(x) &= b_0 + C_1 \cos k\pi x \\ a(x) &= \frac{r}{\delta} b_0 + C_2 \cos k\pi x, \end{aligned} \tag{3.21}$$

where the argument is $k\pi$ in order to satisfy the no-flux boundary conditions and $k > 0$ is the wavenumber. Plugging (3.21) into (3.19) yields the system

$$J\mathbf{b} = \mathbf{0},$$

where $\mathbf{b} = (b(x), a(x))^t$ and J is the Jacobian matrix

$$J = \begin{pmatrix} -(k\pi)^2 D_b & (k\pi)^2 \chi_a b_0 \\ r & -(k\pi)^2 D_a - \delta \end{pmatrix}.$$

The matrix J has two eigenvalues,

$$\lambda_{+,-}(k^2) = \frac{\tau(k^2) \pm \sqrt{\tau(k^2)^2 - 4\Delta(k^2)}}{2}, \tag{3.22}$$

where

$$\begin{aligned} \tau(k^2) &= -(k\pi)^2 (D_b + D_a) - \delta \\ \Delta(k^2) &= (k\pi)^2 D_b \left((k\pi)^2 D_a + \delta\right) - (k\pi)^2 r \chi_a b_0. \end{aligned}$$

The smaller (real part) of these two eigenvalues, $Re(\lambda_-(k^2))$, is always negative for any k, and consequently the uniform solution will only lose stability if $Re(\lambda_+(k^2)) > 0$ for any $k \in \mathbb{N}$. The real part of $\lambda_+(k^2)$ is plotted in Figure (3.12) for different values of b_0. The nodes on each curve denote the value of $\lambda_+(k^2)$ at values of k^2 for $k \in \mathbb{N}$. If any of these nodes are above the horizontal axis, small spatial perturbations to the uniform solution will grow.

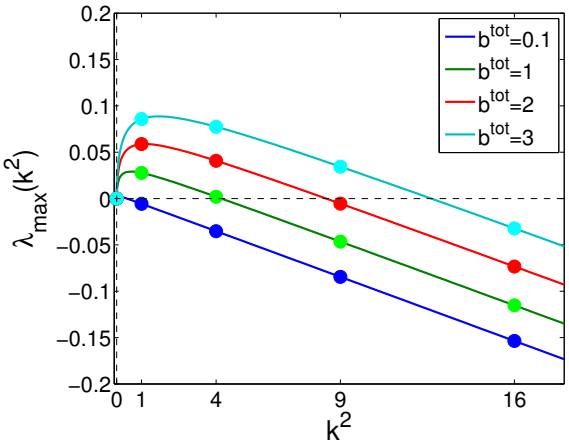

Figure 3.12: Dispersion relation.

3.8.2 Existence of bump solution

If the real part of $\lambda_+(k^2)$ is positive for $1 \leq k \leq n$, we expect a stationary waveform solution with wavenumber $1 \leq k \leq n$. Here we investigate the existence of such solutions. After integrating both sides of the first equation of system (3.19), the resulting equation is separable with solution

$$b = \sigma \exp\left(\frac{\chi_a a}{D_b}\right), \tag{3.23}$$

where σ is a constant of integration defined by the integral condition

$$b^{tot} = \int_0^1 b(x)dx = \int_0^1 \sigma \exp\left(\frac{\chi_a a(x)}{D_b}\right) dx. \tag{3.24}$$

Plugging equation (3.23) into the second equation of system (3.19) provides us with the second order nonlinear differential equation

$$0 = D_a \frac{\partial^2 a}{\partial x^2} + r\sigma \exp\left(\frac{\chi_a a}{D_b}\right) - \delta a. \tag{3.25}$$

Defining $v = a'$, where $'$ denotes differentiation with respect to x, and imposing no-flux boundary conditions allows us to write equation (3.25) as the system

$$\begin{aligned} a' &= v \\ v' &= \frac{1}{D_a}\left[\delta a - r\sigma \exp\left(\frac{\chi_a a}{D_b}\right)\right] \\ v(0) &= 0 \\ v(1) &= 0. \end{aligned} \tag{3.26}$$

Combining system (3.26) with integral condition (3.24), stationary solutions must therefore satisfy the boundary value problem

$$\begin{aligned} a' &= v \\ v' &= \frac{1}{D_a}\left[\delta a - r\sigma \exp\left(\frac{\chi_a a}{D_b}\right)\right] \\ b'_{sum} &= \sigma \exp\left(\frac{\chi_a a(x)}{D_b}\right) \\ \sigma' &= 0 \\ v(0) &= 0 \\ v(1) &= 0 \\ b_{sum}(0) &= 0 \\ b_{sum}(1) &= b^{tot}. \end{aligned} \tag{3.27}$$

We numerically solve system (3.27) using XPPAUT and continue the solution along the parameter b^{tot}. The continuation yields a branch of nonuniform stationary solutions bifurcating from the line of uniform solutions, shown in Figure 3.13.

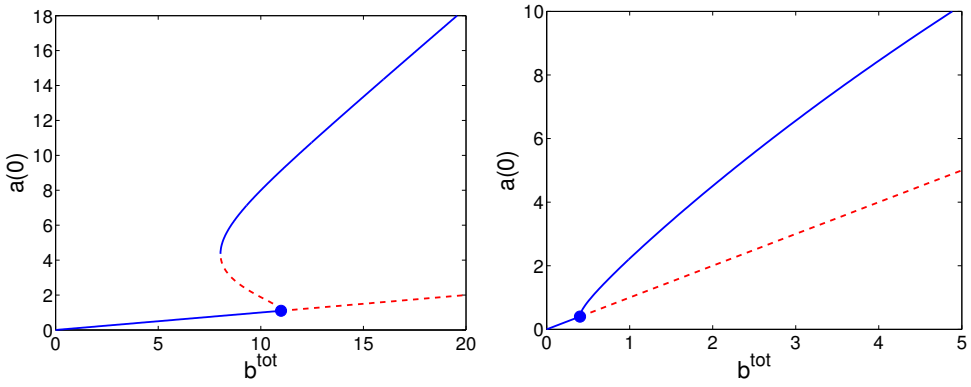

Figure 3.13: Stationary solution bifurcation. The solid blue curves correspond to stable solutions. The red curves correspond to unstable solutions.

3.8.3 Normal form analysis

The numerically generated bifurcation curves in Figure 3.13 suggest the possibility of a subcritical pitchfork bifurcation, and consequently bistability between the uniform solution and the nonuniform stationary bump solution. Our goal now is to characterize the criticality of the bifurcation. To this end, we use perturbation analysis to derive the normal form of the bifurcation.

As in the numerical analysis, we wish to use the parameter $b^{tot} = \int_0^1 b(x)dx$ as our bifurcation parameter. To introduce b^{tot} explicitly into our system, we define $B = b/b^{tot}$ and rewrite system (3.19) in terms of B, resulting in

$$\begin{aligned} 0 &= D_b \frac{\partial^2 B}{\partial x^2} - \chi_a \frac{\partial}{\partial x}\left[B\frac{\partial a}{\partial x}\right] \\ 0 &= D_a \frac{\partial^2 a}{\partial x^2} + r b^{tot} B - \delta a \\ \left.\frac{\partial B}{\partial x}\right|_{x=0,1} &= \left.\frac{\partial a}{\partial x}\right|_{x=0,1} = 0. \end{aligned} \tag{3.28}$$

We perturb the system off of the critical uniform solution defined by b^{tot} such that $\lambda_+(1) = 0$;

that is, we perturb the solution

$$B = 1$$
$$b^{tot} = b^{tot*}$$
$$a = \frac{r}{\delta} b^{tot*},$$

by

$$B = 1 + B_1\epsilon + B_2\epsilon^2 + B_3\epsilon^3 + \mathcal{O}(\epsilon^4)$$
$$b^{tot} = b^{tot*} + b_1^{tot}\epsilon + b_2^{tot}\epsilon^2 + b_3^{tot}\epsilon^3 + \mathcal{O}(\epsilon^4)$$
$$a = \frac{r}{\delta} b^{tot*} + a_1\epsilon + a_2\epsilon^2 + a_3\epsilon^3 + \mathcal{O}(\epsilon^4).$$

Plugging these ϵ-expansions into system (3.28) and collecting similar orders of ϵ produces a system of equations for each order ϵ^k, $k = 0, 1, 2, \ldots$, of the form

$$\mathcal{L}\mathbf{u}_k = \mathbf{f}_k,$$

where

$$\mathcal{L} = \begin{pmatrix} D_b \frac{\partial^2}{\partial x^2} & -\chi_a \frac{\partial}{\partial x} \\ r b_0^{tot} & D_a \frac{\partial^2}{\partial x^2} - \delta \end{pmatrix},$$

$$\mathbf{u}_k = \begin{pmatrix} B_k \\ a_k \end{pmatrix},$$

and $\mathbf{f}_k$ is a function of B_i, b_i^{tot}, and a_i for $i = 0, 1, \ldots, k-1$. Solving the systems through $\mathcal{O}(\epsilon^2)$ imposing no flux boundary conditions and the integral conditions $\int_0^1 B_i(x)dx = 0$ for $i \geq 1$ yields

$$B = 1 + \frac{\chi_a}{D_a} L\cos(\pi x)\epsilon + \mathcal{O}(\epsilon^2)$$
$$b^{tot} = b_0^{tot} + b_2^{tot}\epsilon^2 + \mathcal{O}(\epsilon^3)$$
$$a = r b_0^{tot}/\delta + L\cos(\pi x)\epsilon + \mathcal{O}(\epsilon^2),$$

where L is the nontrivial root of the pitchfork bifurcation equation

$$\gamma_1 b_2^{tot} + \gamma_3 L^3 = 0,$$

and $\gamma_1 > 0$, γ_3 are functions of model parameters.

The bifurcation is supercritical if $\gamma_3 < 0$ and subcritical if $\gamma_3 > 0$. Figure 3.14 shows the agreement between the above analysis and the numerically generated bifurcation diagrams near b^{tot*}.

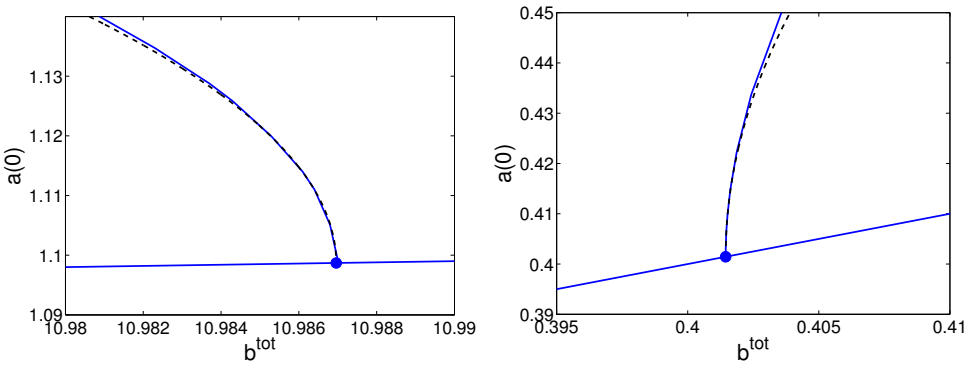

Figure 3.14: Perturbation analysis of the bifurcation. In both frames, the blue line corresponds to the family of uniform solutions for varied b^{tot}, and the blue curve corresponds to a family of nonuniform stationary solutions. The black-dashed curve is the analytically generated bifurcation curve. A. The bifurcation is supercritical ($\gamma_3 < 0$). B. The bifurcation is subcritical ($\gamma_3 > 0$).

4.0 QUALITATIVE EFFECTS OF MONOVALENT VACCINATION AGAINST ROTAVIRUS: A COMPARISON OF NORTH AMERICA AND SOUTH AMERICA

4.1 INTRODUCTION

Rotavirus is the leading cause of severe diarrhea in children under five years of age worldwide, resulting in about 453,000 deaths each year [89]. By the age of five, one in five children will visit a clinic, one in 50 will be hospitalized, and approximately one in 205 will die due to rotavirus infection [22].

Rotavirus strain distribution varies across continent and climate. G1P[8] is the most prevalent human rotavirus strain worldwide, and represents the majority of rotavirus infections in North America (Gentsch et al. 2009, Hull et al. 2011). Although a plurality of cases in South America, Africa, and Asia are due to G1P[8], the majority of cases are collectively caused by strains G3P[8], G4P[8], G9P[8], G2P[4], and a combination of less common strains [73]. The most prevalent strain in a region can change over time, however. Immunity gained after recovery from infection of the current dominant strain exerts selective pressure on that strain, allowing another strain to displace it as the most prevalent [66].

Vaccination programs are considered to be the most effective public health strategies for reducing the incidence rate of severe rotavirus infections. Rotarix is a monovalent vaccine manufactured by GlaxoSmithKline that contains the most common human rotavirus strain, G1P[8] [37]. Rotarix is administered in two doses: the first dose between 6 and 14 weeks of age, and the second by 8 months of age, with at least 4 weeks between doses. Studies have shown that after the second dose, Rotarix provides 90.8% protection against severe rotavirus gastroenteritis caused by G1P[8], 86.9% protection against severe rotavirus

gastroenteritis caused by G3P[8], G4P[8], or G9P[8], and 45.4% protection against severe rotavirus gastroenteritis caused by G2P[4] for up to twelve years after inoculation [70, 97].

Rotarix was introduced in countries throughout North and South America between 2006 and 2013 [60]. Since its introduction, many studies have sought to determine long term effects on disease prevalence and economic impact [7, 8, 79, 80, 78, 64, 65]. However, little has been done to compare the effect of the vaccination on regions with highly varied strain distribution. A multi-strain mathematical model of rotavirus transmission can clarify the effect that vaccination might have on populations with different strain distributions.

In this chapter, we first introduce a two-strain, pre-vaccination rotavirus transmission model. We use our model to investigate the transient and asymptotic behavior of rotavirus within a population, primarily as a function of transmission rate. Our model predicts that two strains of rotavirus can coexist either at fixed infected proportions of the population or oscillate over time, with periodic switching of the more prevalent strain over time. We mathematically explore the periodic behavior to determine what drives these oscillations in the Appendix. We then expand our model to include a class of individuals vaccinated with Rotarix, and we examine the effects of the vaccine on epidemic thresholds and transient behavior. Finally, we explore how vaccination affects the regions with widely differing strain distributions. In each case considered, infection due to rotavirus is substantially decreased for up to ten years after the introduction of the vaccination program. If the efficacy of the vaccination against heterotypic strains is sufficiently low, then our model predicts the potential for major strain replacement in countries where G1P[8] is the dominant serotype.

4.2 TWO STRAIN MODEL: DEVELOPMENT AND BASIC ANALYSIS

We developed a two-strain model of rotavirus transmission, Figure (4.1), in order to determine epidemic thresholds and behavior in an unvaccinated population.

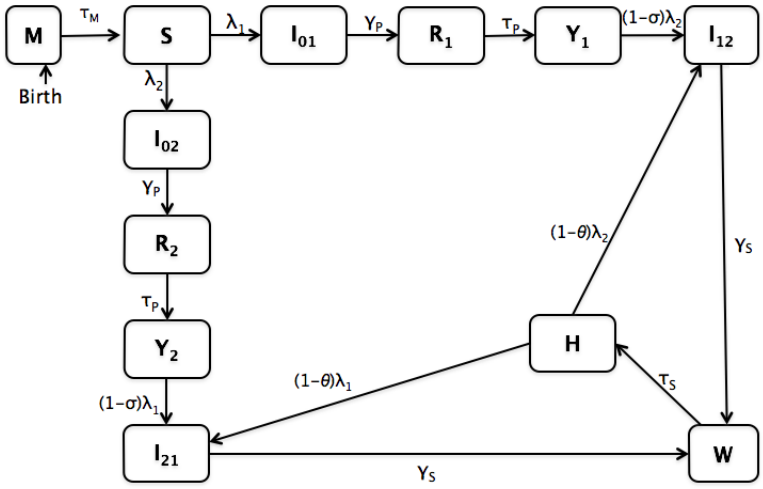

Figure 4.1: The model diagram. Natural mortality rate μ not shown.

Throughout this work, we assume the first strain is G1P[8], and the second strain is a weighted combination of all remaining strains within the population. Individuals are born into the maternally protected population, M. These individuals are immune to both strains of rotavirus for a period of $1/\tau_M$ weeks due to maternal antibodies. After maternal immunity wears off, they enter the susceptible population, S. Here they are at the risk of becoming infected with either strain of rotavirus. Susceptible individuals become infected with strain i at rate β_i upon contact with an infected individual in the class I_{0i}, and at rate $\rho\beta_i$ upon contact with individuals who have previously been infected with and recovered from strain j and are now infected with strain i, I_{ji}, $j \neq i$; $i, j = 1$ or 2. The total transmission rate is written concisely as the force of infection $\lambda_i = \beta_i(I_{0i} + \rho I_{ji})/N$. Upon primary infection with strain i, they enter the class I_{0i} and remain infectious for $1/\gamma_p$ weeks on average, then recover to the class R_i, where they are temporarily immune. The immunity wears off after $1/\tau_p$ weeks and the recovered individuals enter class Y_i, where they are susceptible to a secondary infection of strain j, $i \neq j$, but the risk of secondary infection is reduced by a factor of σ [93]. Thus, secondary infections occur at a rate $(1-\sigma)\lambda_j$, and infected individuals enter the I_{ij} class, remain there for $1/\gamma_s$ weeks on average, then recover to class W where they

are completely immune to both strains for $1/\tau_s$ weeks. Once an individual loses immunity, they then become susceptible again to both strains with added partial immunity θ in the H class, where upon infection at rate $(1-\theta)\lambda_j$, $j = 1, 2$, he or she enters class I_{ij} and stays infected for $1/\gamma_s$ weeks, and recovers into class W [93]. Consequently, no individual ever remains completely immune. Finally, we assume death due to infection is negligible and that the birth and death rates are equal so that the total population remains constant [78].

Our model assumes that individuals who have recovered from strain $i = 1, 2$ must become infected with $j \neq i$ before becoming infected with strain i again. This assumption is based on the findings that secondary infections were more likely to be caused by another strain due to homotypic protection (Velaquez et al. 1996) and that protection following natural infection was predominantly against homotypic strains (Clarke and Desselberger 2015). Other studies have found no evidence of homotypic protection, however (Gladstone et al. 2011). We therefore explore the possibility of reinfection with the same strain in Section 4.4.

The assumptions above and the diagram in Figure 4.1 lead us to the following system of differential equations:

$$
\begin{aligned}
\frac{dM}{dt} &= \mu N - (\tau_M + \mu)M \\
\frac{dS}{dt} &= \tau_M M - \lambda_1 S - \lambda_2 S - \mu S \\
\frac{dI_{01}}{dt} &= \lambda_1 S - (\gamma_p + \mu) I_{01} \\
\frac{dI_{21}}{dt} &= (1-\sigma)\lambda_1 Y_2 + (1-\theta)\lambda_1 H - (\gamma_s + \mu) I_{21} \\
\frac{dI_{02}}{dt} &= \lambda_2 S - (\gamma_p + \mu) I_{02} \\
\frac{dI_{12}}{dt} &= (1-\sigma)\lambda_2 Y_1 + (1-\theta)\lambda_2 H - (\gamma_s + \mu) I_{12} \\
\frac{dR_1}{dt} &= \gamma_p I_{01} - \tau_p R_1 - \mu R_1 \\
\frac{dR_2}{dt} &= \gamma_p I_{02} - \tau_p R_2 - \mu R_2 \\
\frac{dY_2}{dt} &= \tau_p R_2 - (1-\sigma)\lambda_1 Y_2 - \mu Y_2 \\
\frac{dY_1}{dt} &= \tau_p R_1 - (1-\sigma)\lambda_2 Y_1 - \mu Y_1 \\
\frac{dW}{dt} &= \gamma_s I_{21} + \gamma_s I_{12} - \tau_s W - \mu W \\
\frac{dH}{dt} &= \tau_s W - (1-\theta)(\lambda_1 + \lambda_2) H - \mu H,
\end{aligned}
\tag{4.1}
$$

where the force of infection is given by $\lambda_1 = \frac{\beta_1(I_{01}+\rho I_{21})}{N}$ and $\lambda_2 = \frac{\beta_2(I_{02}+\rho I_{12})}{N}$.

Variables	
M	Immune due to maternal antibodies
S	Susceptible
I_{01}	Infected with strain 1 without any prior infection
I_{02}	Infected with strain 2 without any prior infection
R_1	Recovered from strain 1
R_2	Recovered from strain 2
Y_1	Susceptible to strain 2, but immune to strain 1
Y_2	Susceptible to strain 1, but immune to strain 2
I_{21}	Infected with strain 1 after recovering from strain 2
I_{12}	Infected with strain 2 after recovering from strain 1
W	Recovered from both strains and immune to both
H	Partially susceptible to both strains

Table 4.1: System variables

	Parameters	Values	Source
μ	Birth and natural death rate	0.000275 wk^{-1}	
τ_M	Rate at which maternal protection wears off	$\frac{3}{52}$ wk^{-1}	[6],[64],[20]
β_1	Transmission coefficient of strain 1	8-17.5 wk^{-1}	
β_2	Transmission coefficient of strain 2	6.1-18.2 wk^{-1}	
ρ	Reduction of transmissibility of secondary infections	0.5	
γ_p	Rate of recovery from first infection	1 wk^{-1}	[98],[100]
γ_s	Rate of recovery from secondary infection	2 wk^{-1}	[95],[96]
τ_p	Rate at which partial protection wears off after one infection	$\frac{1}{52}$ wk^{-1}	[15],[52]
τ_s	Rate at which partial protection wears off after secondary infection	$\frac{1}{52}$ wk^{-1}	[15],[52]
σ	Reduction in susceptibility after first infection	0.38	[93]
θ	Reduction in susceptibility after secondary infection	0.63	[93]

Table 4.2: System parameters

In system (4.1), N is the total population and $\dot{N} = 0$, so the total population is constant. By rescaling the state variables $M \to M/N$, $S \to S/N$, and so on, we may assume that

$N = 1$, and so each epidemiological class represents a proportion of the total population.

Our analysis will focus largely on the behavior of the primary infected classes, I_{01} and I_{02}, because secondary infections are generally asymptomatic or mild compared to primary infections (Velázquez et al. 1996). We begin our analysis of system (4.1) by identifying steady states and their stability. System (4.1) supports four distinct equilibria in the positive orthant: one disease-free steady state, one with only strain 1 endemic, one with only strain 2 endemic, and one with both strains endemic. We will call these steady states E_0, E_1, E_2, and E_3, respectively.

4.2.1 The disease-free steady state and the basic reproductive numbers

The disease-free steady state is given by $E_0 = (M^0, S^0, 0, 0, 0, 0, 0, 0, 0, 0, 0, 0)$, where M^0 and S^0 must obey

$$\begin{aligned} 0 &= \mu - (\tau_M + \mu)M^0 \\ 0 &= \tau_M M^0 - \mu S^0, \end{aligned}$$

or equivalently,

$$\begin{aligned} M^0 &= \frac{\mu}{\tau_M + \mu} \\ S^0 &= \frac{\tau_M M^0}{\mu} = \frac{\tau_M}{(\tau_M + \mu)}. \end{aligned}$$

To determine epidemic thresholds, we construct the basic reproductive number of each strain, $\mathcal{R}_{0,1}$ and $\mathcal{R}_{0,2}$, by using the method described by [92]. Following their method, we define $x = (x_1, x_2) = (I_{01}, I_{21})$, $\mathcal{F}_{1,i}(x)$ to be the rate of new infections in compartment x_i, and $\mathcal{V}_{1,i}(x)$ to be the difference of the rate of transfer out of compartment x_i and the rate of transfer into compartment x_i by any means other than infection. We then know that $\mathcal{R}_{0,1} = \rho(F_1 V_1^{-1})$, the spectral radius of $F_1 V_1^{-1}$, where $F_1 = [\frac{\partial \mathcal{F}_{1,i}}{\partial x_j}]$, and $V_1 = [\frac{\partial \mathcal{V}_{1,i}}{\partial x_j}]$. Specifically, we have

$$F_1 = \begin{bmatrix} \beta_1 S^0 & \beta_1 \rho S^0 \\ 0 & 0 \end{bmatrix} \text{ and } V_1^{-1} = \begin{bmatrix} \frac{1}{\gamma_p + \mu} & 0 \\ 0 & \frac{1}{\gamma_s + \mu} \end{bmatrix},$$

which yields

$$\mathcal{R}_{0,1} = \frac{\beta_1 S^0}{\gamma_p + \mu} = \frac{\beta_1 \tau_M}{(\gamma_p + \mu)(\tau_M + \mu)} = \left(\frac{\tau_M}{\tau_M + \mu}\right) \beta_1 \left(\frac{1}{\gamma_p + \mu}\right). \tag{4.2}$$

By symmetry, we also have

$$\mathcal{R}_{0,2} = \frac{\beta_2 S^0}{\gamma_p + \mu} = \frac{\beta_2 \tau_M}{(\gamma_p + \mu)(\tau_M + \mu)} = \left(\frac{\tau_M}{\tau_M + \mu}\right) \beta_2 \left(\frac{1}{\gamma_p + \mu}\right). \tag{4.3}$$

These values are the product of the probability of transition into the S class from the M class, $\tau_M/(\tau_M + \mu)$, the transmission rate of the strain, β_i, and the average time period spent in the I_{0i} class, $1/(\gamma_p + \mu)$. We therefore define $\mathcal{R}_{0,i}$ as the number of secondary infections resulting from a single infection of strain i in a naive population. Theorem 2 from van den Driessche and Watmough provides us with the following theorem summarizing this result.

Theorem 1. *The disease free steady state E_0 is locally asymptotically stable (l.a.s.) if both $\mathcal{R}_{0,1} < 1$ and $\mathcal{R}_{0,2} < 1$ and unstable if either $\mathcal{R}_{0,1} > 1$ or $\mathcal{R}_{0,2} > 1$.*

More concisely, Theorem 1 states that if either basic reproductive number $\mathcal{R}_{0,i}$ exceeds the critical threshold of one, then rotavirus can become endemic in the population.

4.2.2 Singly Endemic Steady States

Now that we have established a necessary condition such that either strain can become endemic, we derive conditions under which one of the strains competitively excludes the other, and conditions under which the two strains can coexist.

In order for strain 1 to persist in the population at steady state E_1, we must have

$$\begin{aligned} 0 &= \mu - (\tau_M + \mu) M^1 \\ 0 &= \tau_M M^1 - \lambda_1 S^1 - \mu S^1 \\ 0 &= \lambda_1 S^1 - (\gamma_p + \mu) I_{01}^1 \\ 0 &= \gamma_p I_{01}^1 - \tau_p R_1^1 - \mu R_1^1 \\ 0 &= \tau_p R_1^1 - \mu Y_1^1. \end{aligned} \tag{4.4}$$

It is easy to show that $I_{21}^1 = 0$ at E_1, and so $\lambda_1 = \beta_1 I_{01}$ when strain 2 is extinct and strain 1 reaches steady state. Equivalently, Eqs. (4.4) are satisfied when

$$
\begin{aligned}
M^1 &= \frac{\mu}{\tau_M + \mu} = M^0 \\
S^1 &= \frac{\gamma_p + \mu}{\beta_1} \\
I_{01}^1 &= \frac{\tau_M M^1}{\gamma_p + \mu} - \frac{\mu}{\beta_1} \\
R_1^1 &= \frac{\gamma_p}{\tau_p + \mu}\left(\frac{\tau_M M^1}{\gamma_p + \mu} - \frac{\mu}{\beta_1}\right) \\
Y_1^1 &= \frac{\tau_p \gamma_p}{(\tau_p + \mu)\mu}\left(\frac{\tau_M M^1}{\gamma_p + \mu} - \frac{\mu}{\beta_1}\right),
\end{aligned}
$$

and it is clear that this steady state exists in the positive orthant if and only if $\frac{\tau_M M^1}{\gamma_p+\mu} - \frac{\mu}{\beta_1} > 0$, that is, when $\mathcal{R}_{0,1} > 1$.

Now that we've established existence of E_1, we characterize its stability in the following theorem.

Theorem 2. *Given $\mathcal{R}_{0,i} > 1$, the steady state E_i is locally asymptotically stable if $\hat{\mathcal{R}}_{0,j} := \frac{\beta_j S^i}{\gamma_p+\mu} + \frac{\beta_j \rho(1-\sigma) Y_i^i}{\gamma_s+\mu} < 1$ and unstable if $\hat{\mathcal{R}}_{0,j} > 1$, where $i, j \in \{1, 2\}, i \neq j$.*

Proof. The Jacobian of the of the system evaluated at E_1 has twelve eigenvalues. The first six of these eigenvalues are easy to find, and they are $-\mu, -\mu, -(\mu + \tau_p), -(\mu + \tau_p), -(\mu + \tau_M), -(\mu + \beta_1 I_{01}^1(1-\sigma))$. Since $\mathcal{R}_{0,1} > 1$ by assumption, $I_{01}^1 > 0$, so each of these eigenvalues are negative. The remaining six eigenvalues are comprised of the roots of three separate quadratic polynomials, the first two of which are

$$
\begin{aligned}
p_1(x) &= x^2 + \left(\beta_1 I_{01}^1 + \mu\right) x + \beta_1 I_{01}^1(\gamma_p + \mu) \\
p_2(x) &= x^2 + \left(\gamma_s + \tau_s + 2\mu + \beta_1 I_{01}^1(1-\theta)\right) x + (\mu + \gamma_s)(\mu + \tau_s) + \beta_1 I_{01}^1(1-\theta)(\mu + \tau_s + \gamma_s).
\end{aligned}
$$

Since the nonleading coefficients of these two polynomials are positive, their roots have negative real part.

The remaining two eigenvalues are roots of the quadratic polynomial

$$
p(x) = x^2 + bx + c, \tag{4.5}
$$

where

$$b = \gamma_b + \gamma_s + 2\mu - \beta_2 S^1 - \beta_2\rho(1-\sigma)Y_1^1$$

and

$$c = (\gamma_p + \mu)(\gamma_s + \mu) - \beta_2 S^1(\gamma_s + \mu) - \beta_2\rho(1-\sigma)Y_1^1(\gamma_p + \mu).$$

Thus, the eigenvalues have negative real part if and only if $b > 0$ and $c > 0$. It follows that

$$b > 0 \iff \gamma_p + \gamma_s + 2\mu > \beta_2 S^1 + \beta_2\rho(1-\sigma)Y_1^1 \tag{4.6}$$

and

$$c > 0 \iff (\gamma_p + \mu)(\gamma_s + \mu) > \beta_2 S^1(\gamma_s + \mu) + \beta_2\rho(1-\sigma)Y_1^1(\gamma_p + \mu). \tag{4.7}$$

The inequality (4.7) is equivalent to

$$1 > \frac{\beta_2 S^1}{\gamma_p + \mu} + \frac{\beta_2\rho(1-\sigma)Y_1^1}{\gamma_s + \mu}. \tag{4.8}$$

Note that since γ_p, γ_s, and μ are all strictly positive values,

$$\frac{\beta_2 S^1}{\gamma_p + \mu} + \frac{\beta_2\rho(1-\sigma)Y_1^1}{\gamma_s + \mu} > \frac{\beta_2 S^1}{\gamma_p + \gamma_s + 2\mu} + \frac{\beta_2\rho(1-\sigma)Y_1^1}{\gamma_p + \gamma_s + 2\mu}, \tag{4.9}$$

and so by (4.8) and (4.9), we have

$$1 > \frac{\beta_2 S^1}{\gamma_p + \gamma_s + 2\mu} + \frac{\beta_2\rho(1-\sigma)Y_1^1}{\gamma_p + \gamma_s + 2\mu} \tag{4.10}$$

and thus by multiplying both sides of (4.10) by $\gamma_p + \gamma_s + 2\mu$, we get (4.6). Thus, we have that (4.7) implies (4.6), and so the condition (4.8) is necessary and sufficient for all eigenvalues of the Jacobian matrix evaluated at E_1 to have negative real part. We define $\hat{\mathcal{R}}_{0,2} = \frac{\beta_2 S^1}{\gamma_p+\mu} + \frac{\beta_2\rho(1-\sigma)Y_1^1}{\gamma_s+\mu}$, and the claim is proven. □

The quantity $\hat{\mathcal{R}}_{0,j}$ is not a basic reproductive number in the sense of $\mathcal{R}_{0,j}$ above, but rather an invasion reproductive number for strain j when strain i is already present. It can be understood as the number of infections resulting from a single infection of strain j when only strain $i \neq j$ is endemic. For clarity, consider the case when $i = 1$ and $j = 2$. The quantity $\beta_2 S^1/(\gamma_p + \mu)$ is the number of primary infections resulting from a single case of strain 2 infection in a population where strain 1 is endemic; that is, the number of individuals

who transition from the S class into the $I_{0,2}$ class due to contact with an individual infected with strain 2 (I_{02} or I_{12}). Similarly, the quantity $\beta_2\rho(1-\sigma)Y_1^1/(\gamma_s+\mu)$ is the number of secondary infections resulting from the same single case of strain 2 infection; i.e., the number of individuals who transition from Y_1 into I_{12} due to contact with a strain 2-infected individual. If infections due to strain 2 result in more than one additional infection on average per case, then strain 2 will become endemic in the population.

Notice that for both $j = 1, 2$,

$$\begin{aligned}
\hat{\mathcal{R}}_{0,j} &= \frac{\beta_j S^i}{\gamma_p+\mu} + \frac{\beta_j\rho(1-\sigma)Y_i^i}{\gamma_s+\mu} \\
&= \frac{\beta_j}{\beta_i} + \beta_j\rho(1-\sigma)\frac{\tau_p}{\tau_p+\mu}\frac{\gamma_p}{\gamma_s+\mu}\left(\frac{\tau_M}{(\tau_M+\mu)(\gamma_p+\mu)} - \frac{1}{\beta_i}\right) \\
&< \frac{\beta_j}{\beta_i} + \beta_j\left(\frac{\tau_M}{(\tau_M+\mu)(\gamma_p+\mu)} - \frac{1}{\beta_i}\right) \\
&= \frac{\beta_j\tau_M}{(\tau_M+\mu)(\gamma_p+\mu)} \\
&= \frac{\beta_j\mathcal{R}_{0,j}}{\beta_j} \\
&= \mathcal{R}_{0,j}.
\end{aligned} \tag{4.11}$$

The inequality is due to the fact that $\tau_p/(\tau_p+\mu)$ and $\gamma_p/(\gamma_p+\mu)$ are both between 0 and 1 and the assumption that ρ and σ are both between 0 and 1. The second to last equality uses the identity $\mathcal{R}_{0,j}/\beta_j = \tau_M/(\gamma_p+\mu)(\tau_M+\mu)$. We therefore have that $\hat{\mathcal{R}}_{0,j} < \mathcal{R}_{0,j}$, and importantly, we have that $\hat{\mathcal{R}}_{0,j} > 1$ only if $\mathcal{R}_{0,j} > 1$.

Theorem 2 partially determines the asymptotic behavior of the system and provides us with four cases to be analyzed: (1) $\hat{\mathcal{R}}_{0,1} < 1$ and $\hat{\mathcal{R}}_{0,2} < 1$, (2) $\hat{\mathcal{R}}_{0,1} > 1$ and $\hat{\mathcal{R}}_{0,2} < 1$, (3) $\hat{\mathcal{R}}_{0,1} < 1$ and $\hat{\mathcal{R}}_{0,2} > 1$, and (4) $\hat{\mathcal{R}}_{0,1} > 1$ and $\hat{\mathcal{R}}_{0,2} > 1$. Case (1) is impossible, as

$$\begin{aligned}
\hat{\mathcal{R}}_{0,2} &< 1 \iff \\
\frac{\beta_2 S^1}{\gamma_p+\mu} + \frac{\beta_2\rho(1-\sigma)Y_1^1}{\gamma_s+\mu} &< 1 \iff \\
\frac{\beta_2}{\beta_1}\left(1 + \frac{\rho(1-\sigma)\tau_p\gamma_p(\mathcal{R}_{0,1}-1)}{(\gamma_s+\mu)(\tau_p+\mu)}\right) &< 1 \implies \text{(since } \mathcal{R}_{0,1} > 1\text{)} \\
\frac{\beta_2}{\beta_1} &< 1,
\end{aligned}$$

and so if $\hat{\mathcal{R}}_{0,2} < 1$ then $\beta_2 > \beta_1$. Similarly, if $\hat{\mathcal{R}}_{0,1} < 1$ then $\beta_1 > \beta_2$, and so $\hat{\mathcal{R}}_{0,2} < 1$ and $\hat{\mathcal{R}}_{0,1} < 1$ can never be simultaneously true.

In case (2), strain 1 is much better suited to persist in the population than strain 2 in the sense of epidemic thresholds $\hat{\mathcal{R}}_{0,1}$ and $\hat{\mathcal{R}}_{0,2}$. Consequently, E_1 is the only stable fixed point in the positive orthant. Strain 1 will therefore ultimately remain endemic while strain 2 will become extinct. Similarly, in case (3), since E_2 is the only stable fixed point, strain 2 will remain endemic and strain 1 will become extinct.

In case (4), both strains are above their respective epidemic thresholds, and so both can become and remain endemic in the population. The long term behavior of the system is not entirely determined by the stability of E_1 and E_2, shown in Figure 4.2 in Section 4.2.3.

4.2.3 Dually Endemic Steady States

It was shown in Section 4.2.2 that both strains of rotavirus can persist in the population long term only if $\hat{\mathcal{R}}_{0,1} > 1$ and $\hat{\mathcal{R}}_{0,2} > 1$. Given that multiple strains of rotavirus are found in almost all countries where rotavirus is endemic [73], we study the asymptotic behavior of the system where $\hat{\mathcal{R}}_{0,1} > 1$ and $\hat{\mathcal{R}}_{0,2} > 1$ using numerical simulations.

Specifically, we used XPPAUT [29]) in order to numerically track the stability of the dually endemic steady state E_3 as a function of the transmission rates β_1 and β_2 (Figure 4.2). Region I in Figure 4.2 corresponds to the case when neither strain can persist because $\mathcal{R}_{0,1} < 1$ and $\mathcal{R}_{0,2} < 1$ (E_0 stable). Regions II and III correspond to cases (2) and (3), respectively, from Section 4.2.2; points on the lower red line separating regions II and V satisfy $\hat{\mathcal{R}}_{0,1} = 1$, and points on the upper red line separating regions III and V satisfy $\hat{\mathcal{R}}_{0,2} = 1$. Regions IV and V together describe case (4). In region V, above the red lines and on the outside of the blue curve, E_3 is a stable steady state, and both strains will remain endemic and tend asymptotically toward a fixed resting state. Upon crossing the blue curve into region IV, however, the system undergoes a Hopf bifurcation, and both strains are attracted to a stable limit cycle. Both strains still persist in the population, but they alternate predominance. We study the mechanism that drives these oscillations in Section 4.6.

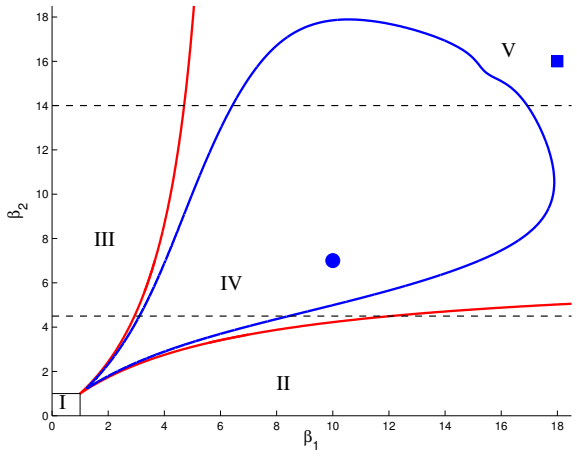

Figure 4.2: Rotavirus behavior as a function of transmission rates β_1 and β_2, without vaccination. In region I, neither strain can be endemic. In region II, the first strain is attracted to a stable non-trivial steady state, while the second strain becomes extinct. In region III, the second strain is attracted to a stable non-trivial steady state, while the first strain becomes extinct. In region IV, both strains exist and oscillate. The blue curve denotes the parameter values for which the steady state E_3 goes through a Hopf bifurcation. In region V, both stains are endemic and are attracted to the stable fixed point E_3. The horizontal black dashed lines denote fixed β_2 values along which we perform bifurcation analysis with respect to β_1 in Figure 4.3. The blue circle and square denote fixed (β_1, β_2) pairs that we consider in Sections 4.2.3 and 4.3.3.

Figure 4.2 shows that steady state E_1 can only be stable if β_2 is substantially less than β_1, and that E_2 can only be stable if β_1 is substantially less than β_2. This can be seen more clearly in Figure 4.3. When β_2 is fixed at 4.5 and β_1 varies as in Figure 4.3A and C, the system passes through regions II-V from Figure 4.2. However, when β_2 is fixed at 14 and β_1 varies as in Figure 4.3B and D, the system passes through region III, where strain 2 is the only endemic state, region IV, where both strains are endemic but oscillate, and region V, where both strains stably coexist.

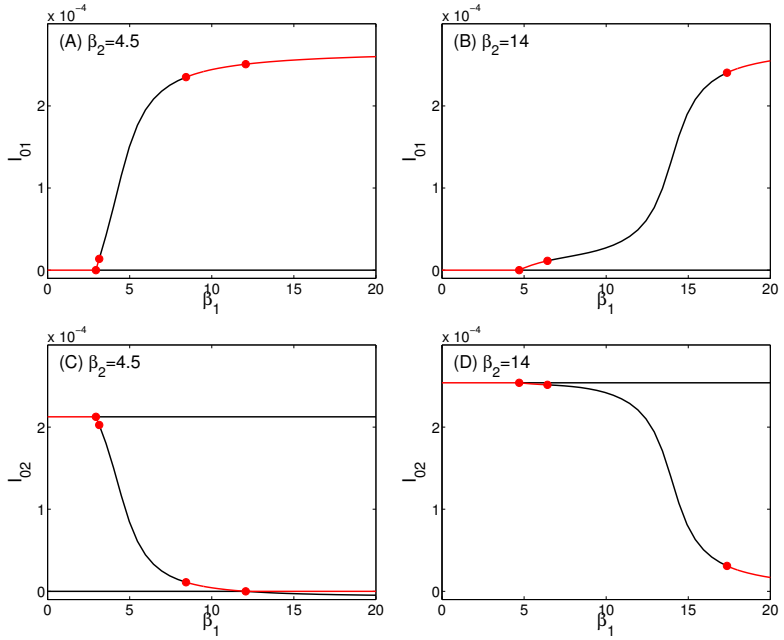

Figure 4.3: Bifurcation diagrams with respect to β_1 with β_2 fixed. (A) and (C): The rate β_2 is fixed at 4.5, corresponding to the lower horizontal dashed line in Figure 4.2. (A) shows the bifurcation in relation to variable I_{01} and (C) in relation to I_{02}. The system is in region III in Figure 4.2 when β_1 is between 0 and 2.932, and consequently the system is attracted to fixed point E_2. The system briefly crosses through region V as β_1 increases from 2.932 until 3.113, allowing both strains to stably coexist. The system then undergoes a Hopf bifurcation at $\beta_1 = 3.113$ and stays in the oscillatory region IV until $\beta_1 = 8.434$. From $\beta_1 = 8.434$ until $\beta_1 = 12.08$, the system returns to region V, where the dually endemic steady state E_3 is stable. Beyond $\beta_1 = 12.08$, the system stays in region II, where E_1 is stable, and strain 1 is therefore the only endemic strain. (B) and (D): Transmission rate β_2 is fixed at 14, corresponding to the upper horizontal dashed line in Figure 4.2. As β_1 increases from 0 to 4.703, the system is in region III from Figure 4.2 and E_2 is stable. When β_1 is between 4.703 and 6.428, the system is in region V, and therefore the dually endemic steady state E_3 is stable. A Hopf bifurcation occurs at $\beta_1 = 6.428$, and the system oscillates until $\beta_1 = 6.93$, where the system leaves region IV and reenters region V, where it stays for all β_1 values considered.

If the transmission rates are chosen from region IV in Figure 4.2, the two strains oscillate in anti-phase over time. Figure 4.4 (A) confirms this behavior of the primary infected states over the first one hundred years, with $\beta_1 = 10$ and $\beta_2 = 7$, denoted by the blue circle in Figure 4.2. Over one oscillation period of approximately twelve years, strain 1 represents the majority of rotavirus cases for roughly ten years at a time, then an abrupt switch occurs causing strain 2 to dominate for approximately two years, after which strain 1 takes over again and the cycle repeats. We explore this switching behavior in the Appendix. As both transmission rates increase and the system tends toward region V in Figure 4.2, the amplitude of the oscillations decreases to zero. The period also decreases as the transmission rates increase, but seems to remain bounded away from zero until the system enters region V: the smallest numerically observed period being around nine years. Once the system enters region V, the two strains coexist nontrivially and stably in the population. Figure 4.4 B shows the transient behavior of the system over the first one hundred years after rotavirus is introduced, with $\beta_1 = 18$ and $\beta_2 = 16$, chosen so that the system falls in region V, represented by the blue square in Figure 4.2. The two strains never alternate dominance; strain 1 constantly comprises a majority of all primary infections due to a higher transmission rate, but strain 2 consistently represents a substantial proportion of all rotavirus infections.

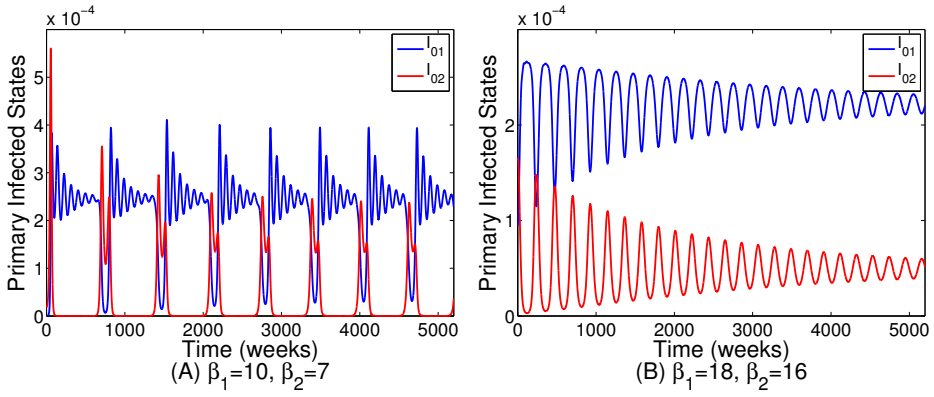

Figure 4.4: Long-term primary infection behavior changes with transmission rate. Panel A shows the primary infected states from system (4.1) when $\beta_1 = 10$ and $\beta_2 = 7$, denoted by the blue circle in region IV of Figure 4.2. The corresponding basic reproductive ratios are $\mathcal{R}_{0,1} = 9.950$ and $\mathcal{R}_{0,2} = 6.965$, respectively. The primary infection rates of strain 1 and strain 2 oscillate in anti-phase over time. While one strain infects a relatively large proportion of the population, the other is essentially dormant until the roles of the two switch, and the once dormant strain becomes the major strain. In this case, strain 1 stays dominant for approximately 600 weeks at a time, after which strain 2 takes over for approximately 200 weeks, and then strain 1 takes over again. Figure B shows the same system when $\beta_1 = 18$ and $\beta_2 = 16$, denoted by the blue square in region V of Figure 4.2, with corresponding basic reproductive ratios $\mathcal{R}_{0,1} = 17.910$ and $\mathcal{R}_{0,2} = 15.920$. In this setting, primary infections due to both strains settle asymptotically to fixed values. The prevalence of strain 1 is approximately 4.5 times larger than that of strain 2, due to the higher transmission rate of strain 1.

4.3 EXPANDED SYSTEM: EFFECTS OF VACCINATION

Now that we have categorized rotavirus behavior as a function of transmission rates in the pre-vaccine era, we expand our model (Figure 4.1) and include a vaccination program using the G1P[8] rotavirus vaccine, Rotarix (Figure 4.5). We include an additional epidemiological

class of vaccinated individuals, V, and assume that a proportion, ϕ, of children in the maternally protected class M will be vaccinated. Therefore, vaccinated individuals leave M and enter V at rate $\phi\tau_M$ and unvaccinated individuals leave M and enter S at rate $(1-\phi)\tau_M$. Those who receive the vaccination gain partial immunity ξ_i $(0 < \xi_i < 1)$ against strain i for $1/\tau_v$ weeks on average, after which they become fully susceptible to both strains. The population size in this expanded system remains constant, and so we assume that $N = 1$ and discuss infections as proportions of the total population. Using our assumptions and definitions, we generate the following system of equations modeling rotavirus transmission and vaccination:

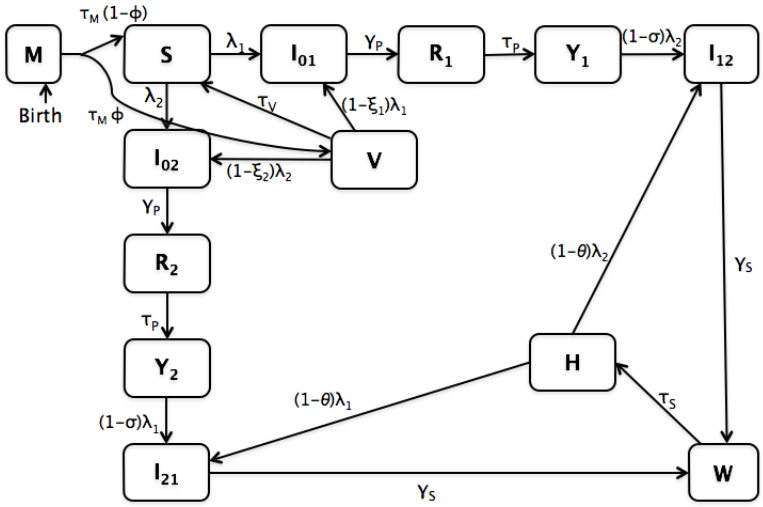

Figure 4.5: The model diagram with vaccination. Removal rate μ not shown.

$$
\begin{aligned}
\frac{dM}{dt} &= \mu N - (\tau_M + \mu)M \\
\frac{dS}{dt} &= \tau_M(1-\phi)M + \tau_v V - \lambda_1 S - \lambda_2 S - \mu S \\
\frac{dV}{dt} &= \tau_M \phi M - \tau_v V - (1-\xi_1)\lambda_1 V - (1-\xi_2)\lambda_2 V - \mu V \\
\frac{dI_{01}}{dt} &= \lambda_1 S + (1-\xi_1)\lambda_1 V - (\gamma_p + \mu)I_{01} \\
\frac{dI_{21}}{dt} &= (1-\sigma)\lambda_1 Y_2 + (1-\theta)\lambda_1 H - (\gamma_s + \mu)I_{21} \\
\frac{dI_{02}}{dt} &= \lambda_2 S + (1-\xi_2)\lambda_2 V - (\gamma_p + \mu)I_{02} \\
\frac{dI_{12}}{dt} &= (1-\sigma)\lambda_2 Y_1 + (1-\theta)\lambda_2 H - (\gamma_s + \mu)I_{12} \\
\frac{dR_1}{dt} &= \gamma_p I_{01} - \tau_p R_1 - \mu R_1 \\
\frac{dR_2}{dt} &= \gamma_p I_{02} - \tau_p R_2 - \mu R_2 \\
\frac{dY_2}{dt} &= \tau_p R_2 - (1-\sigma)\lambda_1 Y_2 - \mu Y_2 \\
\frac{dY_1}{dt} &= \tau_p R_1 - (1-\sigma)\lambda_2 Y_1 - \mu Y_1 \\
\frac{dW}{dt} &= \gamma_s I_{21} + \gamma_s I_{12} - \tau_s W - \mu W \\
\frac{dH}{dt} &= \tau_s W - (1-\theta)(\lambda_1 + \lambda_2)H - \mu H,
\end{aligned}
\tag{4.12}
$$

Here the force of infection is given by $\lambda_1 = \beta_1(I_{01} + \rho I_{21})$ and $\lambda_2 = \beta_2(I_{02} + \rho I_{12})$, and all variables are as in system 4.1.

New Variable and Parameters			
V	Vaccinated		
	Parameters	Values	Source
τ_v	Rate at which vaccination wears off	$\frac{1}{624}$ wk^{-1}	[97]
ϕ	Vaccination coverage	0.9	[99]
ξ_1	Efficacy of vaccination against strain 1	0.9	[70, 94]
ξ_2	Efficacy of vaccination against strain 2	0.85	[94]

Table 4.3: Additional Variables and Parameters

The partial immunity against strain 1 (G1P[8]) gained due to vaccination (ξ_1) is taken to be 0.9 [70, 94]. Early studies on Rotarix efficacy indicated that the vaccine is less effective against heterotypic strains, but recent meta-analysis by Velasquez et al. suggests that the vaccine efficacy against heterotypic strains is much closer to that against homotypic strains. For this reason, we take the immunity against strain 2 gained due to vaccination to be $\xi_2 = 0.85$. The behavior of the primary infected states over varied ξ_2 is briefly explored in Section 4.3.3.

4.3.1 The disease-free steady state and the basic reproductive numbers

The system maintains the four equilibria in the positive orthant, and we will refer to the disease-free steady state, the strain one-endemic steady state, the strain two-endemic steady state, and the dually endemic steady state as E_0^V, E_1^V, E_2^V, and E_3^V, respectively.

Just as in system (4.1), we can use the method described in [92] to determine a control reproductive ratio. System (4.12) is at steady state E_0^V when

$$\begin{aligned} 0 &= \mu - (\tau_M + \mu)M^0 \\ 0 &= \tau_M(1-\phi)M^0 + \tau_v V^0 - \mu S^0 \\ 0 &= \tau_M \phi M^0 - (\tau_v + \mu)V^0, \end{aligned}$$

which is equivalent to

$$\begin{aligned} M^0 &= \frac{\mu}{(\tau_M+\mu)} \\ S^0 &= \frac{(\tau_v+(1-\phi)\mu)\tau_M\mu}{(\tau_v+\mu)(\tau_M+\mu)\mu} \\ V^0 &= \frac{\tau_M\phi\mu}{(\tau_M+\mu)(\tau_v+\mu)}. \end{aligned}$$

Our $\mathcal{F}_{1,i}(x)$ and $\mathcal{V}_{1,i}(x)$ functions are defined in the same way as in Section 4.2.1, and thus we have

$$F_1 = \begin{bmatrix} \beta_1 S^0 + \beta_1(1-\xi_1)V^0 & \beta_1\rho S^0 \\ 0 & 0 \end{bmatrix} \text{ and } V_1^{-1} = \begin{bmatrix} \frac{1}{\gamma_p+\mu} & 0 \\ 0 & \frac{1}{\gamma_s+\mu} \end{bmatrix}.$$

Thus, the control reproductive number of strain 1 in a vaccinated population is

$$\begin{aligned} \mathcal{R}_{c,1} &= \beta_1 \frac{S^0 + V^0(1-\xi_1)}{\gamma_p+\mu} \\ &= \frac{\beta_1\tau_M\mu(\tau_v+(1-\phi)\mu)}{(\gamma_p+\mu)(\tau_v+\mu)(\tau_M+\mu)\mu} + \frac{\beta_1(1-\xi_1)\tau_M\phi\mu}{(\gamma_p+\mu)(\tau_v+\mu)(\tau_M+\mu)} \\ &= \mathcal{R}_{0,1}(1-\frac{\phi\xi_1\mu}{\tau_v+\mu}). \end{aligned}$$

Similarly, we can find the control reproductive number of strain 2, which is

$$\mathcal{R}_{c,2} = \beta_2 \frac{S^0 + V^0(1-\xi_2)}{\gamma_p+\mu} = \mathcal{R}_{0,2}(1-\frac{\phi\xi_2\mu}{\tau_v+\mu}).$$

The values of $\mathcal{R}_{c,i}$ $(i=1,2)$ tell us important information about the effect of vaccination on a naive population. First, $\mathcal{R}_{c,i} = \mathcal{R}_{0,i}(1-\frac{\phi\xi_i\mu}{\tau_v+\mu})$, and thus vaccination decreases the basic reproductive ratio by a factor of $1-\frac{\phi\xi_i\mu}{\tau_v+\mu}$. Second, since $\mathcal{R}_{0,i}$ is independent of ϕ, ξ_i, and τ_v, $\mathcal{R}_{c,i}$ is a decreasing function of ϕ and ξ_i, and an increasing function of τ_v (and therefore a decreasing function of $1/\tau_v$, the average length of immunity conferred by the vaccination). This is expected, as increasing the coverage and efficacy of the vaccine, as well as the duration of vaccine-induced immunity should only impede the strain's ability to establish itself in the population. Moreover, it is worth noting that if $\phi = \xi_i = 1$ and $\tau_v = 0$, then $\mathcal{R}_{c,i} = 0$; that is, if the entire population is vaccinated with a perfect vaccine that confers lifetime immunity, then rotavirus can never become endemic, which is certainly expected and therefore a necessary feature of our model.

4.3.2 Singly Endemic States

Analysis of the stability of steady states E_1^V and E_2^V of system (4.12) follows in a similar manner to the characterization of the corresponding steady states of system (4.1). Using standard linear stability analysis, it becomes clear that E_1^V is an asymptotically stable fixed point of the system if both eigenvalues of the matrix

$$J = \begin{bmatrix} \frac{\partial \dot{I}_{01}}{\partial I_{01}} & \frac{\partial \dot{I}_{01}}{\partial I_{02}} \\ \frac{\partial \dot{I}_{02}}{\partial I_{01}} & \frac{\partial \dot{I}_{02}}{\partial I_{02}} \end{bmatrix} = \begin{bmatrix} A\beta_2 - (\gamma_p + \mu) & A\beta_2\rho \\ B\beta_2 & B\beta_2\rho - (\gamma_s + \mu) \end{bmatrix}, \tag{4.13}$$

where A and B are parameter dependent constants, have negative real part. Therefore, strain 2 can invade the population only if one of these eigenvalues has positive real part, which happens exactly when

$$\hat{\mathcal{R}}_{c,2} > 1,$$

where

$$\hat{\mathcal{R}}_{c,2} = \frac{\beta_2 S}{\gamma_p + \mu} + \frac{\beta_2(1-\xi_2)V}{\gamma_p + \mu} + \frac{\beta_2\rho(1-\sigma)Y_1}{\gamma_s + \mu}\bigg|_{E_1^V}. \tag{4.14}$$

Thus, strain 2 can persist in the population only if $\hat{\mathcal{R}}_{c,2} > 1$. By symmetry, we have the endemic threshold for strain 1, $\hat{\mathcal{R}}_{c,1} = \frac{\beta_1 S}{\gamma_p+\mu} + \frac{\beta_1(1-\xi_1)V}{\gamma_p+\mu} + \frac{\beta_1\rho(1-\sigma)Y_2}{\gamma_s+\mu}\Big|_{E_2^V}$.

Replacing $\hat{\mathcal{R}}_{0,i}$ with $\hat{\mathcal{R}}_{c,i}$ in cases (1)-(4) from Section 4.2.2, these cases still categorize the asymptotic behavior of system (4.12). In particular, case (1) is impossible for the same reason as in section 4.2.2; cases (2) and (3) result in strain 1 and 2 outcompeting the other, respectively; case (4) is the setting in which the two strains can coexist for all time. Region I of Figure 4.6 corresponds to the trivial case in which both $\mathcal{R}_{c,1} < 1$ and $\mathcal{R}_{c,2} < 1$, and so neither strain can become endemic. Regions II and III of the same figure correspond to cases (2) and (3), respectively, and regions IV and V both correspond to case (4).

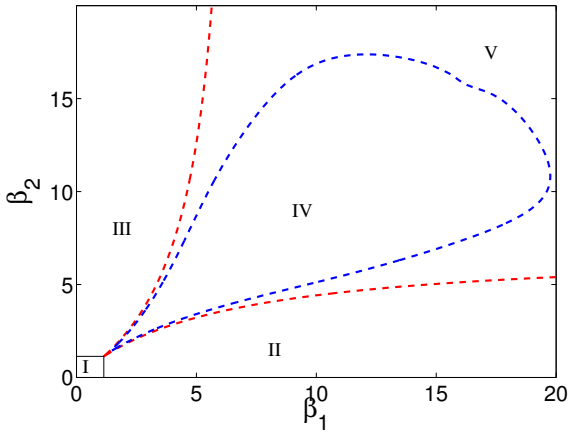

Figure 4.6: Rotavirus behavior as a function of transmission rates, with vaccination. In region I, neither strain can be endemic. In region II, the first strain is attracted to the stable non-trivial steady state E_1^V, while the second strain becomes extinct. In region III, the second strain is attracted to the stable non-trivial steady state E_2^V, while the first strain becomes extinct. In region IV, both strains exist and oscillate. The blue curve denotes the parameter values for which the steady state E_3^V goes through a Hopf bifurcation. In region V, both stains are endemic and are attracted to the stable fixed point E_3^V. The figure shown is made from system (4.12) with $\xi_1 = 0.908$ and $\xi_2 = 0.85$.

Under case (4), the system either approaches a stable, dually endemic steady state or settles into a stable periodic solution, as shown in Figure 4.6. Numerical analysis of the asymptotic behavior of the system in either case follows directly from the analysis in Section 4.2.3, and so we do not repeat it here.

4.3.3 Comparison of effects of vaccination: North America vs South America

In order to evaluate the differential impact of rotavirus vaccination in various regions, we parameterize system (4.12) with continent-specific data, and compare the effect of vaccination on populations in North and South Americas [73]. For the direct comparison of rotavirus dynamics in pre- and post-vaccination eras in North America, Figures 4.2 and 4.6 are shown together in Figure 4.7A. Similarly, rotavirus dynamics in pre- and post-vaccination eras in

South America is shown in Figure 4.7B. We chose transmission rates β_1 and β_2 such that the ratio of individuals infected with strain 1 ($I_{01} + I_{21}$) to individuals infected with strain 2 ($I_{02} + I_{12}$) at the fixed point E_3^V is equal to the ratio of the prevalence of G1P[8] to the prevalence of all other rotavirus strains in a given continent. Specifically, in North America, G1P[8] comprises 73% of all rotavirus strains. We therefore choose β_1 and β_2 so that $\frac{I_{01}+I_{21}}{I_{02}+I_{12}} = 73/27$ is maintained at E_3^V. Similarly, we choose β_1 and β_2 so that the ratio $\frac{I_{01}+I_{21}}{I_{02}+I_{12}} = 34/66$ is maintained in South America. The transmission rates of rotavirus that satisfy this constraint for North America and South America are shown in light blue in Figure 4.7. For both North and South America, the introduction of vaccination can lead to long term oscillations of the two strains for a range of transmission rates, β_1 and β_2 (Figure 4.7).

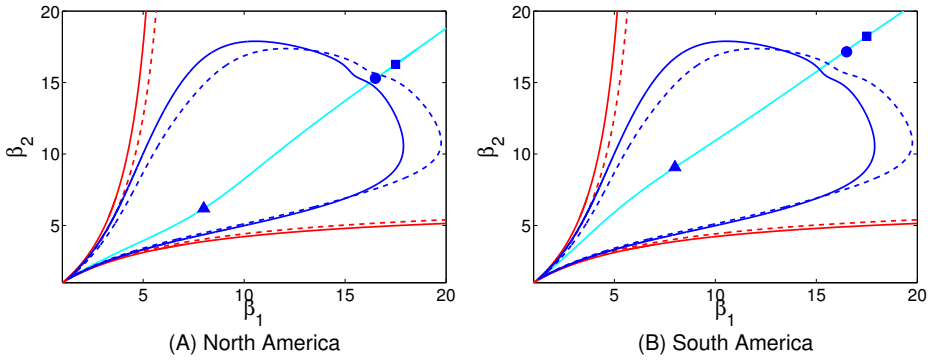

Figure 4.7: Continent specific parameterization for (A) North America and for (B) South America. For both continents, the efficacy of the vaccination against strains 1 and 2 are $\xi_1 = 0.9$ and $\xi_2 = 0.85$, respectively. The solid blue and red lines are the same as in Figure 4.2, the dashed blue and red lines correspond to the same threshold once vaccination is introduced ($\phi = 0.9$). The light blue line is the curve of (β_1, β_2) values that preserve the ratio of strain 1 and strain 2 infected individuals at steady state E_3^V: $\frac{I_{01}+I_{21}}{I_{02}+I_{12}} = \alpha$, where $\alpha = 73/27$ for North America and $\alpha = 34/66$ in South America. Region I is not shown, as it is not considered in the following analysis, but it should be noted that the height of the region is increased by a factor of $1/(1 - (\phi\xi_2\mu)/(\tau_v + \mu))$ and the width is increased by a factor of $(1/(1 - (\phi\xi_2\mu)/(\tau_v + \mu))$, as $\mathcal{R}_{c,i} = \mathcal{R}_{0,i}(1 - \frac{\phi\xi_i\mu}{\tau_v+\mu})$.

Although it is difficult to pin down exact transmission rates and basic reproductive

numbers, we choose transmission rates that give reasonable $\mathcal{R}_0$ values according to previous estimates [65]. The basic reproductive numbers for each transmission rate are shown in Table 4.4. For each fixed transmission rate β_1, the corresponding transmission rate β_2 is lower in North America and higher in South America. This is consistent with the relative incidence due to either strain in each continent.

Transmission rates and reproductive numbers			
β_1	17.5	8	12.8
$\mathcal{R}_{0,1}$	17.4122	7.9594	12.7358
$\mathcal{R}_{c,1}$	16.8269	7.6923	12.3076
North America			
β_2	16.2709	6.1883	11.3938
$\mathcal{R}_{0,2}$	16.1893	6.1573	11.3366
$\mathcal{R}_{c,2}$	15.8353	6.0226	11.0880
South America			
β_2	18.2446	9.0728	13.6028
$\mathcal{R}_{0,2}$	18.1531	9.0273	13.5346
$\mathcal{R}_{c,2}$	17.7313	8.8176	13.2201

Table 4.4: Transmission rates and corresponding basic reproductive numbers for each simulation. The three β_1 values are used in simulations for both the North and South American system, and the corresponding β_2 value is shown in the same column beneath the appropriate header.

Direct comparisons of primary infection dynamics after the introduction of a monovalent vaccination in North America and South America were carried out (Figures 4.8 and 4.9). We assume that vaccination is introduced into the population after the unvaccinated system reaches steady state or limit cycle. For our simulations results, we assume that $\beta_1 = 17.5$ for both continents, and $\beta_2 = 16.2709$ in North America and $\beta_2 = 18.2446$ in South America, as indicated by the blue squares in Figure 4.7 (Figure 4.8A and 4.8C). In this case, Figure 4.7 confirms that the qualitative behavior of system (4.12) before and after vaccination remains unchanged in both continents: the system is attracted to a stable steady state in both cases. In Figures 4.8B and 4.8D, both continents are chosen to have transmission rate $\beta_1 = 8$, and North America has corresponding rate $\beta_2 = 6.1883$ while South America has corresponding rate $\beta_2 = 9.0728$. As indicated by the blue triangles in Figure 4.7, these transmission rates put both continents in a regime under which the system is attracted to a stable limit cycle

both before and after vaccination.

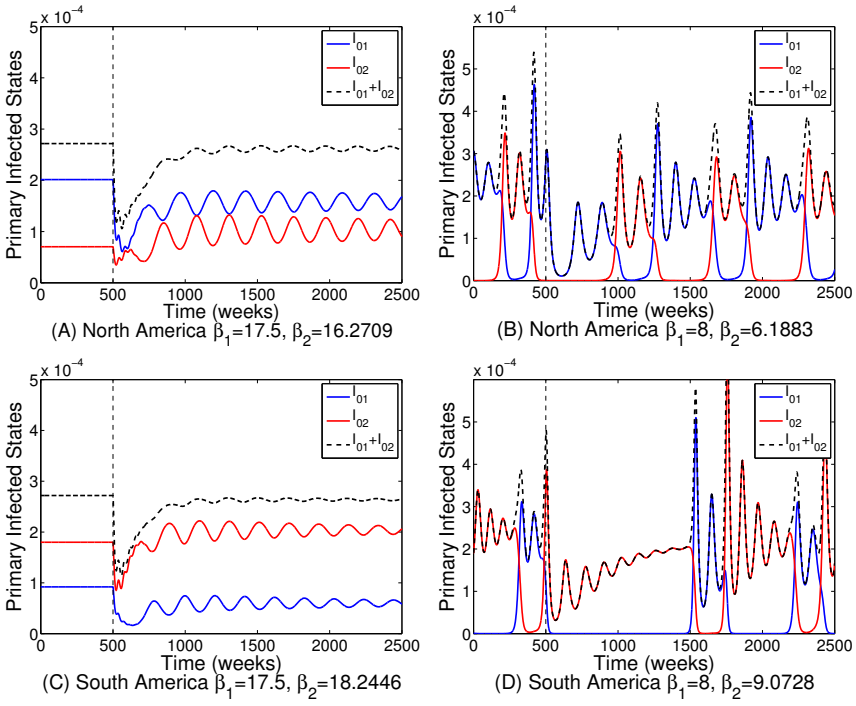

Figure 4.8: Primary infection behavior before and after vaccination is introduced to North and South America. Figures A and C. The system is parameterized with transmission rates corresponding to the blue squares in Figures 4.7 A and B, respectively. The system starts in its pre-vaccination steady steady and 90% of individuals receive the vaccination at time $t = 500$ weeks, denoted the the dashed vertical line. Figures B and D. The system is parameterized with transmission rates corresponding to the blue triangles from Figures 4.7 A and B, respectively. The system starts in its pre-vaccination limit cycle and 90% of individuals receive the vaccination at time $t = 500$ weeks, denoted the the dashed vertical line. In all four cases, the stability behavior of the system is not affected by the vaccination: the system in Figures A and C is attracted to a stable fixed point, and in Figures B and D is attracted to a stable limit cycle before and after vaccination is introduced.

In all cases shown in Figure 4.8, the total primary infected states initially decrease, then recover to levels close to pre-vaccination levels. In Figure 4.8A, the total primary infection in North America decreases for the first half of a year, then begins to recover, and reaches

levels similar to its pre-vaccination state after roughly five years, after which the total primary infection levels remain roughly constant. The growth in primary infected states is due to an increase of individuals infected with strain 2, despite a substantial drop off of strain 1 infections caused by the greater efficacy against strain 1. In Figure 4.8B, the introduction of vaccination leads to an immediate and significant reduction in the total incidence of primary infection, with only strain 1 persisting at a considerably reduced level for roughly ten years. After such time, the oscillations in the dominant strain continue.

The behavior of the system parameterized by South American strain data provides further insights into the effect of vaccination at different strain distributions and transmission rates (Figures 4.8C and 4.8D). The qualitative behavior of the primary infected states in South America is not drastically altered by vaccination (Figure 4.8C). The total incidence of primary infection is not substantially lowered, and recovers to pre-vaccination levels in about year. However, when transmission rates of both strains are relatively low, vaccination is shown to result in a dramatic decrease in both strains (Figure 4.8D). Before vaccination is introduced, the two strains oscillate dominance over time: strain 1 dominates for periods lasting roughly five years, followed by a switch after which strain 2 dominates for roughly eight years. For about twenty years after vaccination is introduced, however, strain 1 is nearly nonexistent in the population and strain 2 persists at a reduced level compared to the pre-vaccination era (Figure 4.8D).

Figure 4.9 shows the most striking difference in the effect of vaccination between system (4.1) parameterized by North and South American strain data. With transmission rate $\beta_1 = 16.5$ for both continents and $\beta_2 = 15.2$ in North America and $\beta_2 = 17.15$ in South America (see the blue circles in Figure 4.7), both systems are attracted to a stable steady state before vaccination is introduced. When vaccine is introduced into South America, the prevalence of both strains quickly decreases and approaches a new steady state (Figure 4.9B). On the other hand, in North America, the two strains begin to oscillate over time after the introduction of vaccination (Figure 4.9A).

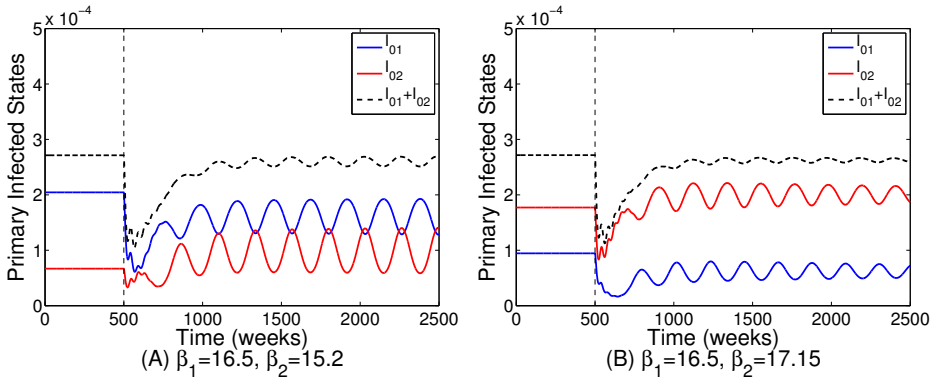

Figure 4.9: Primary infection behavior after vaccination is introduced to North and South America. Figure A shows the behavior of the primary infected states I_{01} and I_{02} in North America before and after the introduction of the vaccine, with transmission rates corresponding to the blue circle in Figure 4.7 A. Before the vaccine is introduced, the system is attracted to a stable steady state, but upon the introduction of vaccination at $t = 500$ weeks (vertical dashed line), the system is instead attracted to a stable limit cycle, resulting in oscillatory behavior in the primary infected states. Figure B shows the behavior of the primary infected states in South America before and after the introduction of the vaccine, with transmission rates corresponding to the blue circle in Figure 4.7 B. The system is attracted to a stable steady state before and after the introduction of vaccination at $t = 500$ weeks. The total incidence of primary rotavirus infection initially decreases, but recovers to pre-vaccination levels within approximately ten years.

In all cases studied (Figures 4.8 and 4.9), the average incidence of strain 1 is lower after vaccination is introduced relative to its prevalence before vaccination, while the incidence of strain 2 is increased on average after vaccination. This is due to the greater efficacy against strain 1 versus that of strain 2. Moreover, if we decrease the efficacy of vaccination against strain 2 from $\xi_2 = 0.85$, the incidence of strain 1 decreases and the incidence of strain 2 increases until the strain 2 overtakes strain 1 as the dominant strain (Figure 4.10).

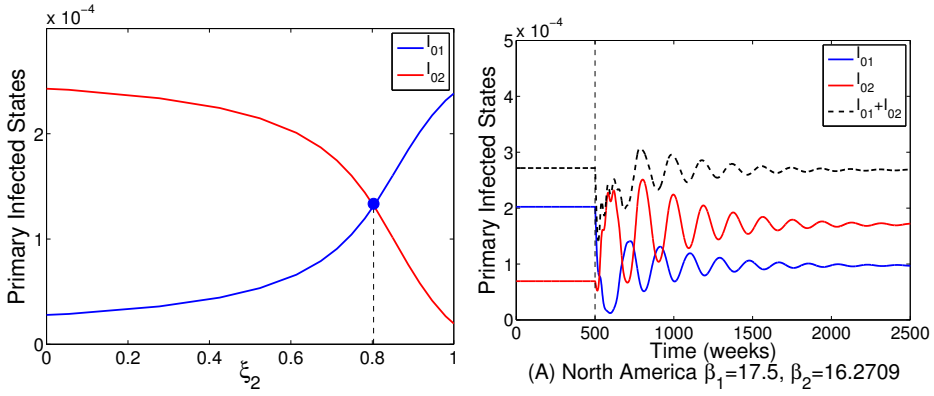

Figure 4.10: Effect of strain 2 efficacy on strain prevalence. (Left) As ξ_2 decreases from $\xi_2 = 0.85$, the steady state of the strain 1 primary infected class decreases, with the strain 2 primary infected class increases. The dominance of the two strains switches around $\xi_2 = 0.8$, below which the population is at risk for dominant strain replacement due to vaccination. The system is parameterized with North American data in this figure, with $\beta_1 = 17.5$, $\beta_2 = 16.2709$, $\phi = 0.9$, and $\xi_1 = 0.9$. (Right) An example of dominant strain replacement with $\xi_2 = 0.65$. After the introduction of the vaccine, strain 2 overtakes strain 1 as the most abundant rotavirus strain.

4.4 EXTENDED MODEL WITH REINFECTION

In the preceding analysis, we assumed individuals could not become reinfected with strain $i = 1, 2$ before becoming infected with strain $j \neq i$, based on the findings that secondary infections were more likely to be caused by another strain due to homotypic protection and that protection following natural infection was predominantly against homotypic strains (Velázquez et al. 1996, Clarke and Desselberger 2015). Because there is conflicting evidence that rotavirus infection provides no such homotypic protection (Gladstone et al. 2011), here we extend our model to allow individuals to become reinfected with the same strain without experiencing infection from the other.

We now assume that after individuals recover from primary infection due to strain $i = 1, 2$

and are now in class Y_i, they can become reinfected with strain i at rate $(1-\theta)\lambda_i$ and enter the new secondary infection class I_{ii}. From this class, individuals recover at rate γ_s and enter recovered class R_i. These interactions are shown in the model diagram Figure 4.11. Since we have added two new infected classes, the force of infection for strain i is now $\lambda_i = \beta_i(I_{0i} + \rho(I_{ii} + I_{ji}))$.

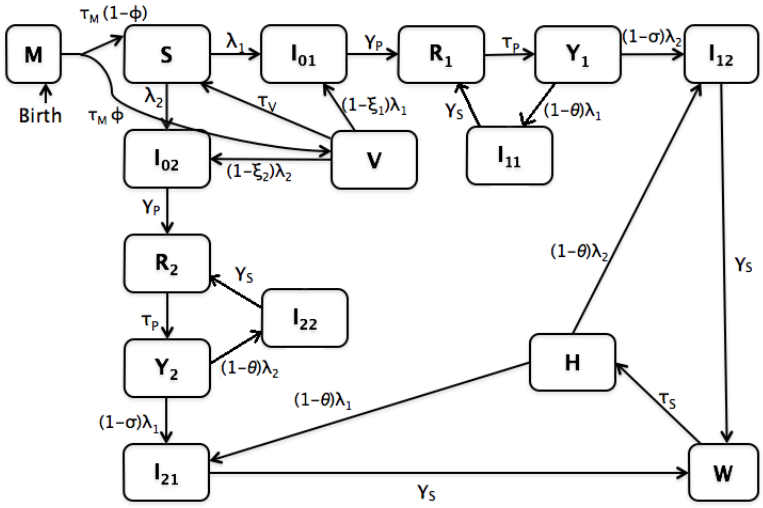

Figure 4.11: Model diagram with reinfection. Natural mortality rate μ not shown.

Under these new assumptions, we arrive at the following system of differential equations:

$$\begin{aligned}
\tfrac{dM}{dt} &= \mu N - (\tau_M + \mu)M \\
\tfrac{dS}{dt} &= \tau_M(1-\phi)M + \tau_v V - \lambda_1 S - \lambda_2 S - \mu S \\
\tfrac{dV}{dt} &= \tau_M \phi M - \tau_v V - (1-\xi_1)\lambda_1 V - (1-\xi_2)\lambda_2 V - \mu V \\
\tfrac{dI_{01}}{dt} &= \lambda_1 S + (1-\xi_1)\lambda_1 V - (\gamma_p + \mu)I_{01} \\
\tfrac{dI_{11}}{dt} &= (1-\theta)\lambda_1 Y_1 - (\gamma_s + \mu)I_{11} \\
\tfrac{dI_{21}}{dt} &= (1-\sigma)\lambda_1 Y_2 + (1-\theta)\lambda_1 H - (\gamma_s + \mu)I_{21} \\
\tfrac{dI_{02}}{dt} &= \lambda_2 S + (1-\xi_2)\lambda_2 V - (\gamma_p + \mu)I_{02} \\
\tfrac{dI_{22}}{dt} &= (1-\theta)\lambda_2 Y_2 - (\gamma_s + \mu)I_{22} \\
\tfrac{dI_{12}}{dt} &= (1-\sigma)\lambda_2 Y_1 + (1-\theta)\lambda_2 H - (\gamma_s + \mu)I_{12} \\
\tfrac{dR_1}{dt} &= \gamma_p I_{01} + \gamma_s I_{11} - \tau_p R_1 - \mu R_1 \\
\tfrac{dR_2}{dt} &= \gamma_p I_{02} + \gamma_s I_{11} - \tau_p R_2 - \mu R_2 \\
\tfrac{dY_2}{dt} &= \tau_p R_2 - (1-\theta)\lambda_2 Y_2 - (1-\sigma)\lambda_1 Y_2 - \mu Y_2 \\
\tfrac{dY_1}{dt} &= \tau_p R_1 - (1-\theta)\lambda_1 Y_1 - (1-\sigma)\lambda_2 Y_1 - \mu Y_1 \\
\tfrac{dW}{dt} &= \gamma_s I_{21} + \gamma_s I_{12} - \tau_s W - \mu W \\
\tfrac{dH}{dt} &= \tau_s W - (1-\theta)(\lambda_1 + \lambda_2)H - \mu H.
\end{aligned} \tag{4.15}$$

The qualitative behavior of system (4.15) is similar to that of system (4.12). Figure 4.12 shows the behavior of system (4.15) as a function of transmission rates before and after vaccination is introduced. The labeled regions in Figure 4.12 are analogous to those in Figures 4.2 and 4.6. In particular, in region II, only strain 1 can persist, and in region

III, only strain 2 can persist. The two strains can coexist in regions IV and V, though both strains oscillate over time in region IV, while the system is attracted to a stable steady state in region V. This behavior as a function of transmission rates is identical to that of system (4.12), though the shape and size of each region is now changed.

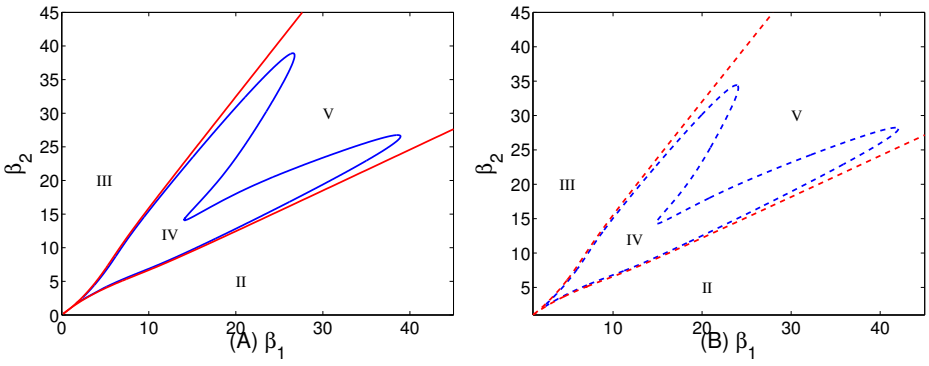

Figure 4.12: Rotavirus infection behavior as a function of transmission rates. Figure A shows the behavior without vaccination, and Figure B shows the behavior after vaccination is introduced, with $\phi = 0.9$, $\xi_1 = 0.9$, and $\xi_2 = 0.85$. In both figures, the red and blue curves are analogous to those from Figures 4.2 and 4.6.

Simulations confirm the similarity between the behavior of systems (4.12) and (4.15). Figure 4.13 shows the effect of vaccination on the primary infected states from system (4.15), parameterized with both North American and South American strain data. As with the analogous Figures 4.8 and 4.9, the introduction of vaccination leads to a substantial and immediate decrease in the overall prevalence of primary rotavirus infection, with the incidence levels recovering to nearly those of the pre-vaccination era after approximately ten years.

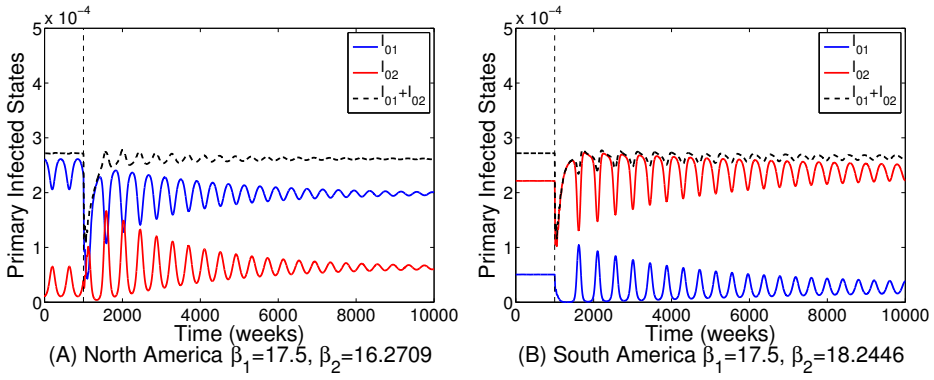

Figure 4.13: Primary infection class behavior before and after introduction of the vaccine. In both figures, the vaccine is introduced at $t = 1000$ weeks, indicated by the vertical dashed black line, with $\phi = 0.9$, $\xi_1 = 0.9$, and $\xi_2 = 0.85$. Figure A shows the primary infected classes when the system is parameterized with North American strain data. Figure B shows the system parameterized with South American data. In both cases, the total incidence of primary infection decreases greatly following the introduction of vaccination, but recovers to near pre-vaccination levels after approximately a decade.

4.5 DISCUSSION

The oral rotavirus vaccine Rotarix® manufactured by GlaxoSmithKline is currently in use worldwide, including the United States, Mexico, Brazil, eleven other countries throughout the Americas [60], greatly reducing the incidence rate of severe gastroenteritis caused by rotavirus. Rotarix has the potential to decrease the total incidence rate in any other nations as well; however, several factors should be considered before implementing a rotavirus vaccination program. In particular, since Rotarix is a monovalent vaccine and strain distributions can vary widely from country to country, it is worthwhile to study the possibility of the selection pressure exerted by the use of monovalent vaccine in countries with various distributions.

In this chapter, we first developed a two-strain system of equations modeling rotavirus

transmission with partial cross-immunity to determine epidemic thresholds for one or both strains. We then extended our system to include vaccination, determined the new epidemic thresholds, and compared these in North and South Americas. As expected, the basic reproductive ratio for both strains decreases with the introduction of vaccination. The decrease is small, however, because the duration of immunity conferred by the vaccine is relatively short. Nevertheless, the severity of rotavirus infection decreases with age, and thus the role of vaccination in shifting the average age of infection is critical. Using available strain distribution data, we then parameterized the system using data from two continents with widely different strain distributions and compared the effect of vaccination between the two. In North America, G1P[8] is responsible for 73% of all rotavirus infections, whereas in South America, G1P[8] results in 34% of all rotavirus infections.

Our results indicate that the effect of vaccination is dependent on both the strain distribution and the overall transmission rates, and consequently the basic reproductive ratios. In both North and South Americas, the use of Rotarix is likely to reduce total rotavirus incidence immediately after introduction. The regions with lower transmission rates are expected to observe the initial reduction in rotavirus cases for longer durations than the regions with higher transmission rates. However, regardless of transmission rates, the prevalence of rotavirus is expected to recover to nearly pre-vaccination levels after approximately a decade.

In all cases, the reduction in G1P[8] due to vaccination was greater than the reduction in the composite strain 2, due to greater efficacy of Rotarix against G1P[8] relative to all other strains. This is consistent with observations following the introduction of Rotarix in American populations [38]. Moreover, the initial decrease in infection incidence is in general larger than the long-term decrease in cases. Our model predicts that the greatest reduction in cases of rotavirus occurs immediately following vaccination introduction to about ten to twelve years after introduction, after which time the total prevalence of rotavirus infection returns to near pre-vaccination levels.

Importantly, our model predicts in regions such as North American where G1P[8] constitutes a majority of rotavirus cases, dominant strain replacement is possible after the introduction of vaccination. Rotarix is most effective against G1P[8] relative to any other strain, resulting in a larger relative decrease in the infection levels due to that strain. In

North America where G1P[8] is the most prevalent, the use of Rotarix might therefore exert selective pressure in favor of a previously less abundant rotavirus strain, which then will establish itself as a dominant strain [53]. In South America, however, G1P[8] comprises a much smaller proportion ($\sim 34\%$) of all rotavirus cases. Consequently, the other rotavirus strains continue to dominate G1P[8] after the introduction of Rotarix, and dominant strain replacement is not expected to be observed.

Our assumption that all non-G1P[8] strains are grouped together in strain 2 is done for mathematical simplification purposes, but the results shown here will likely extend naturally to a three or more strain model. In particular, if we include in our model a separate compartment for each of the five most common strains, we could use the methods described here to compute basic reproductive numbers for each strain, as well an invasive reproductive numbers that determine when a strain can invade and persist in the population given that one or more strains is already endemic. However, our two strain model is advantageous in that it is mathematically tractable, and provides valuable intuition on the overall effect of vaccination on rotavirus prevalence.

Similarly, our assumption that individuals are not susceptible to reinfection with strain $i = 1, 2$ before infection with strain $j \neq i$ was a mathematical simplification and was based on the findings that secondary infections were more likely to be caused by another strain and that protection following natural infection was predominantly against homotypic strains [16, 93]. When we relax this assumption and allow for reinfection, the model predicts small quantitive changes in the outcome of vaccination, increasing the size of the region in transmission rate parameter space over which the system oscillates, but we do not observe any new qualitative behaviors in the system.

Our analysis predicts a rebound in rotavirus incidence five to twenty years after the vaccine is introduced, although the United States has yet to see such a rebound in the six years since the introduction of Rotarix [61]. One reason that the model-predicted rebound might not be observed is that the pentavalent rotavirus vaccine RotaTeq is also in use in the United States, which we did not include in our model. Another, more probable reason why such a rebound might never be observed is that Rotarix provides partial immunity against rotavirus for up to twelve years, and the severity of the symptoms associated with rotavirus

decreases with age, with many cases being asymptomatic in adults [93, 97]. Since our model is not age structured, it does not differentiate between infected children and infected adults, and so many of the model-predicted infections are likely mild or asymptomatic, and would likely go unreported.

Our study shows that the impact of rotavirus vaccination can be significantly affected by region-specific parameters, including strain distribution as well as transmission rates. The model can be adapted to study other infectious diseases that persist in multiple strains.

4.6 APPENDIX: OSCILLATION ANALYSIS

Numerical observations about the behavior of the system drive the study of the oscillations. First, the dynamics of the state variables Y_1 and Y_2 seen in Figure 4.14A and B are slow relative to the dynamics of the infected states shown in Figure 4.4A. Second, Figure 4.14C shows that the variable H has relatively small changes in amplitude as it oscillates. Indeed, if the dynamics of H are frozen so that H is fixed at some intermediate value, the system still oscillates for a range of β_1 and β_2 values.

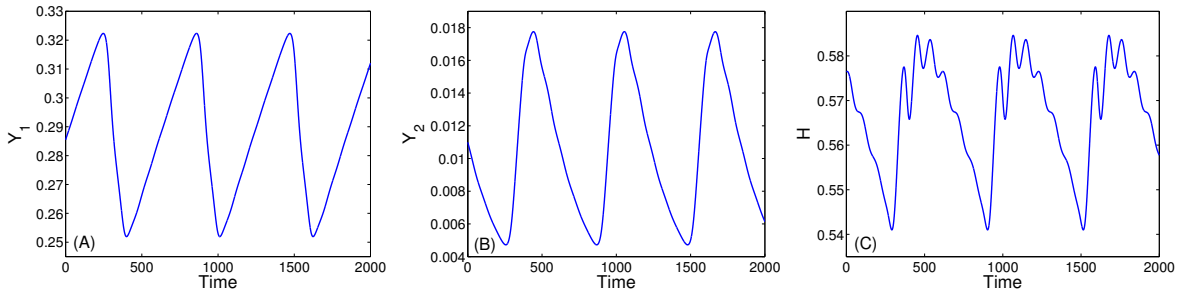

Figure 4.14: (A) and (B): Y_1 and Y_2 are slow variables. (C) H has relatively small oscillations.

We therefore fix the value of H at an intermediate value and introduce a time-scaling parameter τ_y to slow down the dynamics of Y_1 and Y_2 simultaneously. As τ_y is decreased from 1 to 0, the period of the oscillation increases, and the system stops oscillating when $\tau_y = 0$; that is, oscillations vanish when the dynamics of Y_1 and Y_2 are completely turned

off. When τ_y is small, however, Y_1 and Y_2 remain (approximately) on a line with respect to one another, as seen in Figure 4.15.

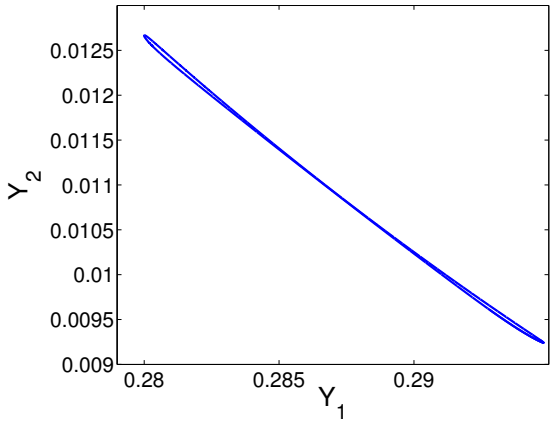

Figure 4.15: Y_2 grows approximately linearly with respect to Y_1 for small values of τ_y. Here, $H = 0.575$ is fixed, $\tau_y = 0.01$, $(\beta_1, \beta_2) = (10, 7)$, $\phi = 0$, and $Y_2 \approx -.02314Y_1 + 0.0774$.

We exploit this observation by treating Y_1 and Y_2 as parameters, with the constraint that they both stay on the line $Y_2 = b + aY_2$, where a and b are approximated from Figure 4.15.

Treating Y_1 and Y_2 as parameters in this way eliminates the oscillations in the system. Instead, the system is generically attracted to one of two steady states: one with strain 1 endemic and strain 2 extinct, the other with strain 2 endemic and strain 1 extinct, which we call E_1^* and E_2^*, respectively. Figure 4.16 shows the stability of the two fixed points as the parameter Y_1, and consequently Y_2, varies. When Y_1 is small, the E_1^* is stable and E_2^* is unstable. As Y_1 increases past some critical threshold, the two steady states immediately switch stability: E_1^* becomes unstable and E_2^* becomes stable.

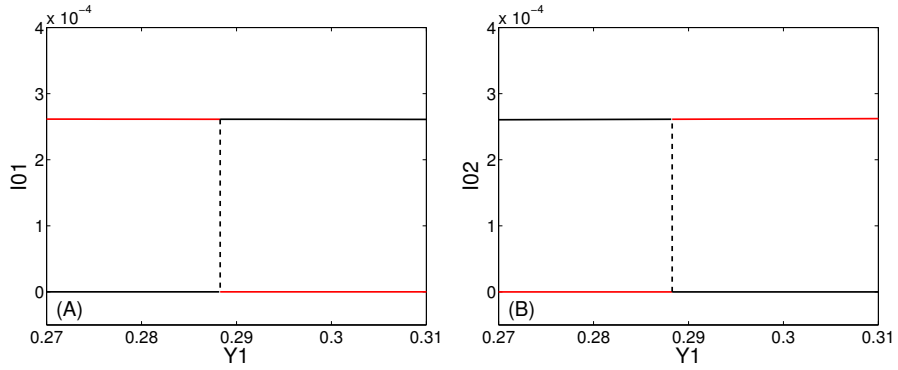

Figure 4.16: Stability switches from strain 1 being "on" and strain 2 being "off" to strain 1 being "off" and strain 2 being "on" past a critical value of Y_1. $(\beta_1, \beta_2) = (10, 7)$, $\phi = 0$. Bifurcation at $Y_1 = 0.28828$.

This instantaneous switch in the stability of the system is due to a degenerate hyperplane of fixed points at the critical value of Y_1. In particular, at E_i^*, we must have

$$\begin{aligned} \frac{dI_{0i}}{dt} &= 0 \\ \frac{dI_{ji}}{dt} &= 0 \end{aligned}$$

which occurs if and only if

$$\beta_i(I_{0i} + \rho I_{ji})S - (\gamma_p + \mu)I_{0i} = 0 \tag{4.16}$$

$$[(1-\sigma)Y_j + (1-\theta)H]\,\beta_i(I_{0i} + \rho I_{ji}) - (\gamma_s + mu)I_{ji} = 0. \tag{4.17}$$

Equation (4.16) is satisfied if and only if

$$I_{0i} = \frac{\beta_i \rho S}{(\gamma_p + \mu) - \beta_i S} I_{ji}, \tag{4.18}$$

and by plugging (4.18) into (4.17), we get

$$\left[\,[(1-\sigma)Y_j+(1-\theta)H]\,\beta_i\left(\frac{\beta_i\rho S}{(\gamma_p+\mu)-\beta_i S}+\rho\right)-(\gamma_s+\mu)\right]I_{ji} \;=\; 0.$$

If $I_{ji}\neq 0$, then $\frac{dI_{0i}}{dt}=0$ and $\frac{dI_{ji}}{dt}=0$ if and only if

$$[(1-\sigma)Y_j+(1-\theta)H]\,\beta_i\left(\frac{\beta_i\rho S^*}{(\gamma_p+\mu)-\beta_i S^*}+\rho\right)-(\gamma_s+\mu) \;=\; 0,$$

or equivalently,

$$S_i^* \;=\; \frac{\gamma_p+\mu}{\gamma_s+\mu}\left(\frac{1}{\beta_i}\left(\gamma_s+\mu-\beta_i\rho[(1-\sigma)Y_j+(1-\theta)H]\right)\right), \tag{4.19}$$

where S_i^* is the value of S at the fixed point E_i^*. Thus, E_1^* and E_2^* coincide if and only if

$$S_1^*=S_2^*. \tag{4.20}$$

In this case, I_{01}, I_{02}, I_{21} and I_{12} are all nonzero and from system (4.1) we have $\frac{dS}{dt}=0$ if and only if

$$\begin{aligned} S_i^* &= \frac{\tau_M M}{\beta_1(I_{01}+\rho I_{21})+\beta_2(I_{02}+\rho I_{12})-\mu} \\ &= \frac{\tau_M M}{\beta_1(\alpha_1+\rho)I_{21}+\beta_2(\alpha_2+\rho)I_{12}-\mu}, \end{aligned} \tag{4.21}$$

where $\alpha_i=(\beta_i\rho S_i^*)/(\gamma_p+\mu-\beta_i S_i^*)$.

Setting equations (4.19) and (4.21) equal defines a line in the I_{21}-I_{12} plane, along which the reduced system is at a steady state. Since $I_{0i}=\alpha_i I_{ji}$, the line of fixed points in the I_{21}-I_{12} plane defines a hyperplane of fixed points in I_{01}-I_{02}-I_{21}-I_{12} space.

This hyperplane exists only if equation (4.20) is satisfied. Given our requirement that $Y_2=b+aY_1$, equation (4.20) is equivalent to

$$Y_1 \;=\; \frac{(\beta_1-\beta_2)(\gamma_s+\mu)}{\beta_1\beta_2\rho(1-\sigma)(1-a)}+\frac{b}{1-a}, \tag{4.22}$$

which, when evaluated at parameter values specified in our simulation, is exactly the bifurcation value of Y_1 as in Figure 4.16.

To visualize this bifurcation in system (4.1), we now allow Y_1 and Y_2 to vary as dynamic variables, but slow down their dynamics by a factor of $\tau_y = 0.01$ and continue to treat H as a parameter fixed at $H = 0.575$. Figure 4.17 shows the infected state I_{02} versus the susceptible class Y_1. The vertical dashed line coincides with the critical value of Y_1 from Figure 4.16. Beginning in the lower left corner of the oscillation in Figure 4.17, as Y_1 increases through the critical value of Y_1, the stability switches from strain 1 endemic to strain 2 endemic, and I_{02} quickly grows to a steady state. After I_{02} increases, Y_1 begins to decrease again because all of the individuals who are susceptible to only strain 2 (i.e., individuals in class Y_1) quickly begin to become infected. Once Y_1 decreases past the critical Y_1 value, the incidence of strain 2 drops off sharply and Y_1 begins to increase again.

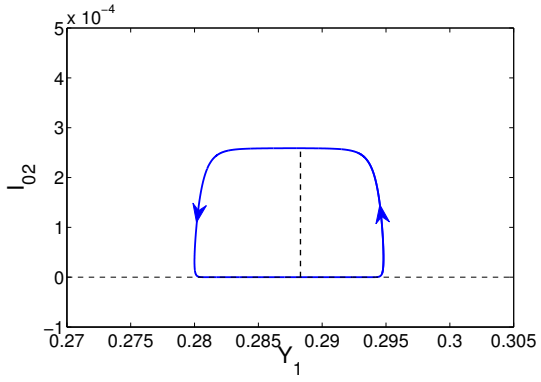

Figure 4.17: Y_1 plotted against I_{02} in the full system with Y_1 and Y_2 slowed down by a factor of $\tau_y = 0.01$, and H frozen at 0.575. In this case, the transmission rates are $(\beta_1, \beta_2) = (10, 7)$, and there is no vaccination ($\phi = 0$). After Y_1 passes a critical threshold from left to right along the bottom of the blue curve, there is a relative abundance of individuals who are susceptible to strain 2 but not strain 1, and strain 2 gets turned "on." I_{02} remains on until Y_1 falls below the critical value, after which strain 2 is turned "off" and strain 1 is turned "on."

In terms of a population, this means that while strain 1 is infecting a large proportion of the population, strain 2 is almost extinct. Consequently, much more individuals become

infected with strain 1 than strain 2, and upon recovery, they are only susceptible to strain 2. The switch between strain 1 being the more prevalent strain to strain 2 taking over occurs when the number of individuals susceptible to only strain 2 surpasses a critical threshold. Immediately after the switch, there are much more individuals only susceptible to strain 2, but as these individuals become infected and recover, more will be susceptible to only strain 1, prompting another switch in the dominant strain back to strain 1, and the cycle repeats. The class of individuals who have recovered from strain i and are susceptible only to strain j are therefore the driving force behind the oscillations: both strains require a sufficient number of susceptible individuals available only to that strain in order to infect a nontrivial proportion of the population. However, since the number of individuals who are susceptible to only strain 1 is inversely proportional to that of those susceptible to only strain 2, the two strains oscillate dominance over time.

5.0 CONCLUSION

The chapters of this thesis contain a variety of results, both mathematical and biological, arising from questions concerning pathogen dynamics. The primary focus is on the development and analysis of simple mathematical models to study complex dynamics, and we consider these on a variety of scales, from within host to without, and populations well-mixed to spatially homogeneous. Our results have produced testable predictions, interesting mathematical problems, and questions open to future study.

In Chapter 2, we studied the competition for space and resources between the host's native microbiota and invasive Salmonella Typhimurium within the inflamed mammalian intestinal tract. A key factor that facilitates S. Typhimurium invasion their ability to maintain two phenotypically distinct subpopulations: one fast growing avirulent population, and a slower growing virulent population. Importantly, the avirulent cells can activate a virulence factor and consequently switch into the virulent subpopulation. We developed an optimization method to determine the minimum population size with which the salmonella must invade so that they will outcompete the established microbiota population. We use this method to make experimentally testable predictions about the optimal initial proportion of avirulent cells in the invading population and about the virulence factor activation rate that maximize the chance of a successful invasion.

A simple within-host Lokta-Volterra-type competition model between virulent S. Typhimurium and native commensal microbiota was presented by Brown et al. in [13]. They encapsulate the net advantage S. Typhimurium gains over the microbiota in a scaling parameter on the mass action competition term. An extended model that considers the competition of both avirulent and virulent phenotypes with commensal microbiota was presented in [23]. Their model was the first to separately consider the two salmonella phenotypes to study co-

existence between them. Our model advances the field further by explicitly coupling a model for the inflammatory immune response with both the food and differential killing hypotheses proposed by Stecher and Hardt in [83], thereby creating a unified competition structure.

Cooperation among organisms is an anomaly when survival is viewed as a competition. The self-destructive cooperation of the virulent bacteria within S. Typhimurium populations has therefore been studied extensively [1, 23]. How such a self sacrificing relationship might have evolved remains an open question, however. Such questions related to evolutionary dynamics are frequently studied using stochastic methods, modeling phenotypic variation as a random variable [31, 57]. Applying existing methods to the question of the coevolution of the two distinct phenotypes in the context of maximizing their success against commensal microbiota presents an immediate and substantial issue: most stochastic processes used to study evolution (e.g., Moran processes, branching processes) consider a single stochastic variable, and the inclusion of a second stochastic variable makes the development of an analytically tractable model difficult or impossible. The construction of a framework in which two or more stochastically varying populations evolve would be both beneficial to the study of S. Typhimurium and also groundbreaking in the study of evolutionary dynamics.

In Chapter 3, we analyzed an anomalous behavior observed in interacting bacterial pulses in a one-dimensional nutrient gradient. When two populations of *E. coli* are placed on opposite ends of a long plate that contains a uniform supply of nutrient in the interior, both populations will initially form pulses and move up the nutrient gradient toward one another. The bacteria will often meet somewhere in the middle of the plate and form a single, larger pulse, but occasionally they will instead change direction and move back toward the end of the plate from which they came. Using the classic Keller-Segel partial differential equations model for bacterial chemotaxis, we captured this turn-around behavior analytically. In order to study the effects of model parameters on the transient behavior of the two interacting populations, we used Gaussian distributions to approximate the spatial profile of each model variable. This approximation allowed us to derive an ordinary differential equations model for the dynamics of the spatial moments of each variable, which agrees qualitatively with the Keller-Segel model in many important ways. Using our approximate model, we were able to determine parameter settings in which the bacterial populations are predicted to

turn around and those in which they will combine. For example, if the bacterial population size is increased, our model predicts that a higher proportion of trials will result in the two populations turning around. If the medium is made more fluid, more trials are expected to result in the populations combining.

The work in Chapter 3 is the first to consider transient direction switches in the collective behavior of bacteria. The system of ODEs we derived using a Gaussian approximation to the spatial profile of each population considered is similarly the first of its kind applied to collective behavior models. This type of approximation can naturally be applied to any spatio-temporal system in which each spatial profile is approximately symmetric and pulsatile. On the other hand, populations whose dynamics evolve according to the Keller-Segel equations do not necessarily maintain such a pulse-like shape. For instance, bacteria can move as an asymmetric front, or largely diffuse out and never aggregate in the interior of the domain before forming a pulse along a spatial boundary. Our approximation therefore only holds under conditions that induce symmetric, interior pulse formation.

A natural extension of the work conducted in Chapters 2 and 3 is to explicitly consider the spatial dimension of bacterial competition. A shortcoming of well-mixed Lokta-Volterra-type competition models is that they necessarily result in competitive exclusion: one population must drive the other to extinction. Spatial models can allow for coexistence of the competing species [3, 88]. In the case of bacterial invasion of the gut, this might correspond to the salmonella outcompeting the native microbiota in a patch of the intestinal lining. This more closely reflects the biology, as the salmonella do not uniformly eliminate all of the host's microbiota upon successful invasion. Our method described in Chapter 3 of approximating spatial moments of bacterial populations can be applied to analyze such a model, to efficiently consider the effect of varying model parameters.

In Chapter 4, we used an extended SIR-type, two-strain epidemiological model to study the transmission of rotavirus in a human population, before and after the introduction of the monovalent vaccination Rotarix. We considered the overall effect of the vaccination on the proportion of the infected individuals over time, and on the effect it has on epidemic thresholds (that is, the basic reproductive ratios). Our results indicate that the effect of vaccination is dependent on both the strain distribution and the transmission rates of both

strains. In all cases considered, the use of Rotarix reduced total rotavirus incidence immediately after introduction. Regions with lower transmission rates, however, are expected to observe a longer duration of decreased rotavirus incidence following the initial reduction after the vaccine is introduced than the regions with higher transmission rates. However, regardless of transmission rates, the prevalence of rotavirus is expected to recover to nearly pre-vaccination levels after approximately a decade. Importantly, our analysis predicted that in regions where strain G1P[8] constitutes a majority of rotavirus cases, dominant strain replacement is possible after the introduction of vaccination.

The issue of dominant strain replacement is important because it introduces a new pathogen into a naive population, which consequently weakens our ability to control its spread and effects [53]. Our model is general enough in structure that it can be readily adapted to model other viruses that maintain more than one strain, thereby helping to predict mechanisms by which strain replacement can occur. Another important study that could accompany our analysis is one that considers cost-effectiveness of vaccination implementation. Understanding the cost of a vaccination program versus the cost of healthcare and lost work time due to illness is crucial in determining whether it is economically viable to institute a mass vaccination program, and detailed models such as ours can help provide accurate estimates of these expenses [80].

BIBLIOGRAPHY

[1] Ackermann M, Stecher B, Freed NE, Songhet P, Hardt WD, and Doebeli M (2008) Self-destructive cooperation mediated by phenotypic noise. Nature, 454(7207), 987-990.

[2] Alt W and Lauffenburger DA (1987) Transient behavior of a chemotaxis system modelling certain types of tissue inflammation. Journal of mathematical biology, 24(6), 691-722.

[3] Amarasekare P (2003) Competitive coexistence in spatially structured environments: a synthesis. Ecology Letters, 6(12), 1109-1122.

[4] Antia R, Levin BR, and May RM (1994) Within-host population dynamics and the evolution and maintenance of microparasite virulence. American Naturalist, 457-472.

[5] Arciero JC, Ermentrout GB, Upperman JS, Vodovotz Y, and Rubin JE (2010) Using a mathematical model to analyze the role of probiotics and inflammation in necrotizing enterocolitis. PLoS One, 5(4), e10066.

[6] Atchison C, Lopman B, Edmunds WJ (2010) Modeling the seasonality of rotavirus disease and the impact of vaccination in England and Wales. Vaccine 28(18):3118-3126.

[7] Atkins KE, Shim E, Pitzer VE, Galvani AP (2012) Impact of rotavirus vaccination on epidemiological dynamics in England and Wales. Vaccine 30(3):552-564.

[8] Atkins KE, Shim E, Carroll S, Quilici S, Galvani AP (2012) The cost-effectiveness of pentavalent rotavirus vaccination in England and Wales. Vaccine 30(48):6766-6776.

[9] Ben-Shachar R and Koelle K (2015) Minimal within-host dengue models highlight the specific roles of the immune response in primary and secondary dengue inf

[10] Bernoulli D and Blower S (2004) An attempt at a new analysis of the mortality caused by smallpox and of the advantages of inoculation to prevent it. Reviews in medical virology, 14(5), 275-288.

[11] Brennan MA and Cookson BT (2000) Salmonella induces macrophage death by caspase-1-dependent necrosis. Molecular microbiology, 38(1), 31-40.

[12] Brenner MP, Levitov LS, and Budrene EO (1998) Physical mechanisms for chemotactic pattern formation by bacteria. Biophysical Journal, 74(4), 1677-1693.

[13] Brown SP, Le Chat L, and Taddei F (2008) Evolution of virulence: triggering host inflammation allows invading pathogens to exclude competitors. Ecology letters, 11(1), 44-51.

[14] The Centers for Disease Control and Prevention, *Salmonella*, http://www.cdc.gov/salmonella/general/. Accessed March 5, 2014.

[15] Chiba S, Yokoyama T, Nakata S, Morita Y, Urasawa T, Taniguchi K, et al (1986) Protective effect of naturally acquired homotypic and heterotypic rotavirus antibodies. Lancet 2(8504):417-421.

[16] Clarke E, Desselberger U (2015) Correlates of protection against human rotavirus disease and the factors influencing protection in low-income settings. Mucosal Immunol. 8(1):1-17.

[17] Coburn BJ, Wagner BG, and Blower S (2009) Modeling influenza epidemics and pandemics: insights into the future of swine flu (H1N1). BMC medicine, 7(1), 30.

[18] Costerton JW, Stewart PS, and Greenberg EP (1999) Bacterial biofilms: a common cause of persistent infections. Science, 284(5418), 1318-1322.

[19] Day J, Rubin J, Vodovotz Y, Chow CC, Reynolds A, and Clermont G (2006) A reduced mathematical model of the acute inflammatory response II. Capturing scenarios of repeated endotoxin administration. Journal of theoretical biology, 242(1), 237-256.

[20] de Blasio BF, Kasymbekova K, Flem E (2010) Dynamic model of rotavirus transmission and the impact of rotavirus vaccination in Kyrgyzstan. Vaccine 28(50):7923-7932.

[21] Demir M, Douarche C, Yoney A, Libchaber A, and Salman H (2011) Effects of population density and chemical environment on the behavior of Escherichia coli in shallow temperature gradients. Physical biology, 8(6), 063001.

[22] Dennehy PH (2008) Rotavirus vaccines: An overview. Clin Microbiol Rev 21(1):198208.

[23] Diard M, Garcia V, Maier L, Remus-Emsermann MN, Regoes RR, Ackermann M, and Hardt WD (2013) Stabilization of cooperative virulence by the expression of an avirulent phenotype. Nature, 494(7437), 353-356.

[24] Douarche C, Buguin A, Salman H, and Libchaber A (2009) E. Coli and oxygen: a motility transition. Physical review letters, 102(19), 198101.

[25] Doelman A and Kaper TJ (2003) Semistrong pulse interactions in a class of coupled reaction-diffusion equations. SIAM Journal on Applied Dynamical Systems, 2(1), 53-96.

[26] Edelstein-Keshet L (1988) Mathematical models in biology (Vol. 46). SIAM.

[27] Ei SI, Mimura M, and Nagayama M (2002) Pulse-pulse interaction in reaction-diffusion systems. Physica D: Nonlinear Phenomena, 165(3), 176-198.

[28] Eisenberg MC, Eisenberg JN, D'Silva JP, Wells EV, Cherng S, Kao YH, and Meza R (2015) Forecasting and Uncertainty in Modeling the 2014-2015 Ebola Epidemic in West Africa. arXiv preprint arXiv:1501.05555.

[29] Ermentrout B (2002) Simulating, analyzing, and animating dynamical systems: a guide to XPPAUT for researchers and students (Vol. 14). SIAM.

[30] Fields P, Swanson R, Haidaris C, Heffron F (1986) Mutants of Salmonella typhimurium that cannot survive within the macrophage are avirulent. Proceedings of the National Academy of Sciences, 83(14), 5189-5193.

[31] Foster D and Young P (1990) Stochastic evolutionary game dynamics?. Theoretical population biology, 38(2), 219-232.

[32] Gentsch JR, Hull JJ, Teel EN, Kerin TK, et al. (2009) G and P Types of Circulating Rotavirus Strains in the United States during 19962005: Nine Years of Prevaccine Data.The Journal of Infectious Diseases 200:S99105.

[33] Gladstone BP, Ramani S, Mukhopadhya I, Muliyil J, et al. (2011) Protective Effect of Natural Rotavirus Infection in an Indian Birth Cohort. The New England journal of medicine 365:337-46.

[34] Gog J, Murcia A, Osterman N, Restif O, McKinley T, Sheppard M, Achouri S, Wei B, Mastroeni P, Wood J, Maskell D, Cicuta P, Bryant C (2012) Dynamics of Salmonella infection of macrophages at the single cell level. Journal of The Royal Society Interface, 9(75), 2696-2707.

[35] Gog JR, Pellis L, Wood JL, McLean AR, Arinaminpathy N, and Lloyd-Smith JO (2015) Seven challenges in modeling pathogen dynamics within-host and across scales. Epidemics, 10, 45-48.

[36] Griffiths M (Ed.) (2005) Understanding Pathogen Behaviour Virulence, Stress Response and Resistance (Vol. 111). CRC Press.

[37] Grimwood K, Lambert SB, Milne RJ (2010) Rotavirus infections and vaccines: burden of illness and potential impact of vaccination. Paediatr Drugs 12(4):235256.

[38] Gurgel RQ, Alvarez ADJ, Rodrigues A, Ribeiro RR, Dolabella SS, et al. (2014) Incidence of Rotavirus and Circulating Genotypes in Northeast Brazil during 7 Years of National Rotavirus Vaccination. PLoS ONE 9(10): e110217. doi:10.1371/journal.pone.0110217.

[39] Hillen T and Painter KJ (2009) A users guide to PDE models for chemotaxis. Journal of mathematical biology, 58(1-2), 183-217.

[40] Höfer T, Sherratt JA, and Maini PK (1995) Cellular pattern formation during Dictyostelium aggregation. Physica D: Nonlinear Phenomena, 85(3), 425-444.

[41] Horstmann D (2003) From 1970 until present: the Keller-Segel model in chemotaxis and its consequences. I. Jahresberichte DMV 105(3), 103165.

[42] Horstmann D and Stevens A (2004) A constructive approach to traveling waves in chemotaxis. Journal of Nonlinear Science, 14(1), 1-25.

[43] Hoshen MB, Heinrich R, Stein WD, and Ginsburg H (2000) Mathematical modelling of the within-host dynamics of Plasmodium falciparum. Parasitology, 121(03), 227-235.

[44] Hull JJ, Teel EN, Kerin TK, Freeman MM, et al. (2011) United States Rotavirus Strain Surveillance From 2005 to 2008 Genotype Prevalence Before and After Vaccine Introduction. The Pediatric Infectious Disease Journal 30: S42S47.

[45] Kang K, Kolokolnikov T, and Ward MJ (2007) The stability and dynamics of a spike in the 1D Keller-Segel model. IMA journal of applied mathematics, 72(2), 140-162.

[46] Keller EF and Segel LA (1970) Initiation of slime mold aggregation viewed as an instability. Journal of Theoretical Biology, 26(3), 399-415.

[47] Keller EF and Segel LA (1971) Model for chemotaxis. Journal of theoretical biology, 30(2), 225-234.

[48] Keller EF and Segel LA (1971) Traveling bands of chemotactic bacteria: a theoretical analysis. Journal of Theoretical Biology, 30(2), 235-248.

[49] Klapper I and Dockery J (2010) Mathematical description of microbial biofilms. SIAM review, 52(2), 221-265.

[50] Lapidus IR, and Schiller R (1976) Model for the chemotactic response of a bacterial population. Biophysical journal, 16(7), 779.

[51] Lof ME, De Gee M, and Hemerik L (2009) Odor-mediated aggregation enhances the colonization ability of Drosophila melanogaster. Journal of theoretical biology, 258(3), 363-370.

[52] Makela M, Marttila J, Simell O, Ilonen J (2004) Rotavirus-specific T-cell responses in young prospectively followed-up children. Clin Exp Immunol 137(1):173-178.

[53] Martcheva M, Bolker BM, Holt RD (2008) Vaccine-induced pathogen strain replacement: what are the mechanisms? J. R. Soc. Interface 5:3-13.

[54] Maurer J and Lee M (2005) Salmonella: virulence, stress response and resistance. Understanding Pathogen Behaviour: Virulence, Stress Response and Resistance. Griffiths, M.(Ed.) Woodhead Publishing Limited, Cambridge, England, 215-239.

[55] Murray JD (2002) Mathematical Biology I: An Introduction, vol. 17 of Interdisciplinary Applied Mathematics.

[56] Nagai T and Ikeda T (1991) Traveling waves in a chemotactic model. Journal of mathematical biology, 30(2), 169-184.

[57] Nowak MA (2006) Evolutionary dynamics. Harvard University Press.

[58] Othmer HG and Hillen T (2002) The diffusion limit of transport equations II: Chemotaxis equations. SIAM Journal on Applied Mathematics, 62(4), 1222-1250.

[59] Park S, Wolanin PM, Yuzbashyan E a, Lin H, Darnton NC, Stock JB, Silberzan P, and Austin R (2003) Influence of topology on bacterial social interaction. Proceedings of the National Academy of Sciences, 100(24), 13910-13915.

[60] PATH (2013) Country introduction, maps and list. Available at: http://sites.path.org/rotavirusvaccine/country-introduction-maps-and-spreadsheet/.

[61] Payne DC, Wikswo M, Parashar UD (2012) Manual for the surveillance of vaccine-preventable diseases, Chapter 13: Rotavirus. Centers for Disease Control and Prevention, Atlanta, GA.

[62] Penner K, Ermentrout B, and Swigon D (2012) Pattern formation in a model of acute inflammation. SIAM Journal on Applied Dynamical Systems, 11(2), 629-660.

[63] Perkins A, Siraj A, Ruktanonchai CW, Kraemer M, and Tatem A (2016) Model-based projections of Zika virus infections in childbearing women in the Americas. bioRxiv, 039610.

[64] Pitzer VE, Viboud C, Simonsen L, Steiner C, Panozzo CA, Alonso WJ, et al. (2009) Demographic variability, vaccination, and the spatiotemporal dynamics of rotavirus epidemics. Science 325(5938):290-294.

[65] Pitzer VE, Atkins KE, de Blasio BF, Van Effelterre T, Atchison CJ, et al. (2012) Direct and Indirect Effects of Rotavirus Vaccination: Comparing Predictions from Transmission Dynamic Models. PLoS ONE 7(8): e42320. doi:10.1371/journal.pone.0042320

[66] Pitzer VE, Viboud C, Lopman BA, Patel MM, Parashar UD, Grenfell BT (2011) Modeling rotavirus strain dynamics in developed countries to understand the potential impact of vaccination on genotype distributions. PNAS 108(48) 19353-19358.

[67] Price I, Mochan-Keef ED, Swigon D, Ermentrout GB, Lukens S, Toapanta FR, Ross TM, and Clermont G (2015) The inflammatory response to influenza A virus (H1N1): An experimental and mathematical study. Journal of theoretical biology, 374, 83-93.

[68] Reynolds A, Rubin J, Clermont G, Day J, Vodovotz Y, and Ermentrout GB (2006) A reduced mathematical model of the acute inflammatory response: I. Derivation of model and analysis of anti-inflammation. Journal of theoretical biology, 242(1), 220-236.

[69] Rose J, Singer ME (2008) Projecting vaccine efficacy: accounting for geographic strain variations. Pharmacoeconomics 26(3):185-189.

[70] Ruiz-Palacios GM, Pérez-Schael I, Velázquez FR et al. (2006) Safety and Efficacy of an Attenuated Vaccine against Severe Rotavirus Gastroenteritis. The New England Journal of Medicine 354(1)11-22.

[71] Salman H and Libchaber A (2007) A concentration-dependent switch in the bacterial response to temperature. Nature cell biology, 9(9), 1098-1100.

[72] Salman H, Zilman A, Loverdo C, Jeffroy M, and Libchaber A. (2006). Solitary modes of bacterial culture in a temperature gradient. Physical review letters, 97(11), 118101.

[73] Santos N, Hoshino Y (2005) Global distribution of rotavirus serotypes/genotypes and its implication for the development and implementation of an effective rotavirus vaccine. Recv. Med. Virol. 15:29-56.

[74] Santos RL, Raffatellu M, Bevins CL, Adams LG, Tkel C, Tsolis RM, and Bäumler AJ (2009) Life in the inflamed intestine, Salmonella style. Trends in microbiology, 17(11), 498-506.

[75] Saragosti J, Calvez V, Bournaveas N, Buguin A, Silberzan P, and Perthame B (2010) Mathematical description of bacterial traveling pulses. PLoS Comput Biol, 6(8), e1000890.

[76] Schnell S, Grima R, and Maini P (2007) Multiscale Modeling in Biology New insights into cancer illustrate how mathematical tools are enhancing the understanding of life from the smallest scale to the grandest. Am Sci, 95(2), 134-142.

[77] Segel LA (1976) Incorporation of receptor kinetics into a model for bacterial chemotaxis. Journal of theoretical biology, 57(1), 23-42.

[78] Shim E, Banks HT, Castillo-Chavez C. (2006) Seasonal pattern of rotavirus infection with its vaccination. Modeling The Dynamics of Human Diseases: Emerging Paradigms and Challenges. AMS Contemporary Mathematics Series Vol. 410:327-348.

[79] Shim E, Feng Z, Martcheva M, Castillo-Chavez C. (2006) An Age-Structured Epidemic Model of Rotavirus with Vaccination. J. Math. Biol. 53 719-746.

[80] Shim E, Galvani AP (2009) Impact of transmission dynamics on the cost-effectiveness of rotavirus vaccination. Vaccine 27(30):4025-4030.

[81] Short MB, Bertozzi AL, and Brantingham PJ (2010) Nonlinear patterns in urban crime: Hotspots, bifurcations, and suppression. SIAM Journal on Applied Dynamical Systems, 9(2), 462-483.

[82] Stecher B, Robbiani R, Walker AW, Westendorf AM, Barthel M, Kremer M, Chaffron S, Macpherson AJ, Buer J, Parkhill J, Dougan G, von Mering C, Hardt WD (2007)

Salmonella enterica serovar typhimurium exploits inflammation to compete with the intestinal microbiota. PLoS Biol, 5(10), e244.

[83] Stecher B and Hardt WD (2008) The role of microbiota in infectious disease. Trends in microbiology, 16(3), 107-114.

[84] Stewart PS and Costerton JW (2001) Antibiotic resistance of bacteria in biofilms. The lancet, 358(9276), 135-138.

[85] Stevens A and Othmer HG (1997) Aggregation, blowup, and collapse: the ABC's of taxis in reinforced random walks. SIAM Journal on Applied Mathematics, 57(4), 1044-1081.

[86] Sturm A, Heinemann M, Arnoldini M, Benecke A, Ackermann M, Benz M, Dormann J, and Hardt WD (2011). The cost of virulence: retarded growth of Salmonella Typhimurium cells expressing type III secretion system 1. PLoS Pathog, 7(7), e1002143.

[87] Sun W, Ward MJ, and Russell R (2005) The Slow Dynamics of Two-Spike Solutions for the Gray–Scott and Gierer–Meinhardt Systems: Competition and Oscillatory Instabilities. SIAM Journal on Applied Dynamical Systems, 4(4), 904-953.

[88] Takenaka Y, Matsuda H, and Iwasa Y (1997) Competition and evolutionary stability of plants in a spatially structured habitat. Researches on population ecology, 39(1), 67-75.

[89] Tate JE, Burton AH, Boschi-Pinto C, Steele AD, Duque J, Parashar UD (2012) 2008 estimate of worldwide rotavirus-associated mortality in children younger than 5 years before the introduction of universal rotavirus vaccination programmes: a systematic review and meta-analysis. Lancet Infect Dis doi:10.1016/S1473- 3099(11)70253-5.

[90] Thiennimitr P, Winter SE, Winter MG, Xavier MN, Tolstikov V, Huseby DL, Sterzenbach T, Tsolis R, Roth J, and Bäumler AJ (2011).Intestinal inflammation allows Salmonella to use ethanolamine to compete with the microbiota. Proceedings of the National Academy of Sciences, 108(42), 17480-17485.

[91] Tyson R, Lubkin SR, and Murray JD (1999) A minimal mechanism for bacterial pattern formation. Proceedings of the Royal Society of London B: Biological Sciences, 266(1416), 299-304.

[92] van den Driessche P, Watmough J (2002) Reproduction numbers and sub-threshold endemic equilibria for compartmental models of disease transmission. Mathematical Biosciences 180:29-48.

[93] Velázquez FR, Matson DO, Calva JJ, Guerrero L, Morrow AL, Carter-Campbell S, et al (1996) Rotavirus infections in infants as protection against subsequent infections. The New England journal of medicine 335(14):1022-1028.

[94] Velazquez DE, Parashar UD, Jiang B (2014) Strain diversity plays no major role in the varying efficacy of rotavirus vaccines: An overview. Infection, Genetics and Evolution 28:561-571.

[95] Ward RL, Bernstein DI, Shukla R, McNeal MM, Sherwood JR, Young EC, et al. (1990) Protection of adults rechallenged with a human rotavirus. The Journal of infectious diseases 161(3):440-445.

[96] Ward RL, Bernstein DI, Young EC, Sherwood JR, Knowlton DR, Schiff GM (1986) Human rotavirus studies in volunteers: determination of infectious dose and serological response to infection. The Journal of infectious diseases 154(5):871-880.

[97] Weidemann F, Dehnert M, Koch J, Wichmann O, Hḧole M (2014) Modelling the epidemiological impact of rotavirus vaccination in Germany - A Bayesian approach. Vaccine 32:5250-5257.

[98] White LJ, Buttery J, Cooper B, Nokes DJ, Medley GF (2008) Rotavirus within day care centres in Oxfordshire, UK: characterization of partial immunity. Journal of the Royal Society, Interface / the Royal Society 5(29):1481-1490.

[99] WHO. WHO UNICEF coverage estimates 2011 [cited 2012 May 19]; Available from: http://apps.who.int/immunization_monitoring/globalsummary/timeseries/tswucoveragedtp1.html

[100] Wilde J, Yolken R, Willoughby R, Eiden J (1991) Improved detection of rotavirus shedding by polymerase chain reaction. Lancet 337(8737):323-6.

[101] Wonham MJ, de-Camino-Beck T, and Lewis MA (2004) An epidemiological model for West Nile virus: invasion analysis and control applications. Proceedings of the Royal Society of London B: Biological Sciences, 271(1538), 501-507.